UC Santa Barbara
UC Santa Barbara Electronic Theses and Dissertations

Title
Gallium Arsenide Lasers and Monolithic Integration on Silicon

Permalink
https://escholarship.org/uc/item/4h77s5tm

Author
Verrinder, Paul

Publication Date
2023

Peer reviewed|Thesis/dissertation

eScholarship.org Powered by the California Digital Library
University of California

University of California
Santa Barbara

Gallium Arsenide Lasers and Monolithic Integration on Silicon

A dissertation submitted in partial satisfaction
of the requirements for the degree

Doctor of Philosophy
in
Electrical and Computer Engineering

by

Paul Austin Verrinder

Committee in charge:

Professor Jonathan Klamkin, Chair
Professor Larry Coldren
Professor John Bowers
Professor Jon Schuller

December 2023

The Dissertation of Paul Austin Verrinder is approved.

Professor Larry Coldren

Professor John Bowers

Professor Jon Schuller

Professor Jonathan Klamkin, Committee Chair

August 2023

Gallium Arsenide Lasers and Monolithic Integration on Silicon

Copyright © 2023

by

Paul Austin Verrinder

This thesis is dedicated to my wife, Elsi and our son, Melvin.

Acknowledgements

I consider myself very fortunate to have had the opportunity to pursue a PhD at UCSB. This work would not have been possible without the guidance, support and many contributions from my colleagues, the UCSB staff, and of course, my family.

I would like to first acknowledge my advisor, Professor Jonathan Klamkin. He has been an invaluable source of guidance and support for me over the past five years, both in my research and professional development, and in my personal life. I am grateful for the opportunity I had to join his lab at the beginning of my PhD (despite knowing almost nothing about photonics); I truly would not be where I am now without his mentoring and support.

I would also like to thank the members of my PhD committee, Professor Larry Coldren, Professor John Bowers, and Professor Jon Shuller, for their constructive feedback and advice on this dissertation and throughout my PhD journey.

I am grateful to all the members in the Klamkin group for their help and support over the years. Lei Wang and Bei Shi performed the many MOCVD growths and regrowths that made this work possible. Lei Wang, Thomas Meissner, and Fengqiao Sang provided much guidance and help in the cleanroom as I was learning my way around early on. I enjoyed many good discussions with Michael Nickerson relating to design, fab, simulation and testing of GaAs devices. Michael also helped multiple times with laser bar cleaving, and was an excellent study partner for the screening exam during our first year. I would also like to thank all the remaining group members, past and present, who have supported me along the way: Tyler Zhang, Diya Hu, Yuan Liu, Si Zhu, Victoria Rosborough, Joe Fridlander, Sergio Pinna, Fabrizio Gambini, Bowen Song.

The cleanroom at UCSB is a state-of-the-art facility and I would like to thank all the staff for their help and advice over the years, and their hard work in maintaining all the

tools. Special thanks to Brian Thibeault, Demis John, Tony Bosch, Aidan Hopkins, Don Freeborn, Biljana Stamenic, Lee Sawyer, Bill Mitchell, Bill Millerski, Luis Zuzunaga, Mike Day, Mike Silva, and many others. I would also like to thank Jes Sherman at Freedom Photonics for the many useful discussions on SGDBR lasers and wavelength tuning.

Last, but not least, I would like to thank my family. My wife, Elsi, has been a constant source of love, support, and encouragement over the years. She has contributed in every way, from helping me with formatting slides and figures, to taking care of our son, Melvin, while I spent long hours in the cleanroom. I could not have done this without her. I would also like to acknowledge my parents-in-law, who helped us with caring for Melvin while I was writing this dissertation and Elsi was at work. And of course my parents and many siblings, who are always supportive, even when they don't know what it is that I actually do.

I would be remiss if I did not also acknowledge my Christian faith. It is entirely by God's sovereign grace and guidance in my life that I have accomplished what I have.

"Trust in the Lord with all your heart,
and do not lean on your own understanding.
In all your ways acknowledge him,
and he will make straight your paths."
Proverbs 3:5-6

Curriculum Vitæ

Paul Austin Verrinder

Education

2023	Ph.D. in Electrical Engineering (Expected), University of California, Santa Barbara.
2020	M.S. in Electrical Engineering, University of California, Santa Barbara.
2015	B.S. in Electrical Engineering, California State University, Fresno

Publications

1. **P. Verrinder**, L. Wang, B. Shi, S. Zhu, and J. Klamkin, "InAs/GaAs Quantum Dot Lasers on CMOS-Compatible (001) Silicon by MOCVD Direct Heteroepitaxy," in CLEO 2023, Technical Digest Series (Optica Publishing Group, 2023), paper SM2J.2.

2. M. Nickerson, **P. Verrinder**, L. Wang, B. Song, and J. Klamkin, "Broadband Optical Phase Modulator with Low Residual Amplitude Modulation," in Optica Advanced Photonics Congress 2022, Technical Digest Series (Optica Publishing Group, 2022), paper IW4B.4.

3. M. Nickerson, B. Song, L. Wang, **P. Verrinder**, J. Brookhyser, G. Erwin, J. Kleinert, and J. Klamkin, "Broadband and Low Residual Amplitude Modulation Phase Modulator Arrays for Optical Beamsteering Applications," in Conference on Lasers and Electro-Optics, Technical Digest Series (Optica Publishing Group, 2022), paper SS1D.4.

4. L. A. Coldren, **P. A. Verrinder** and J. Klamkin, "A Review of Photonic Systems-on-Chip Enabled by Widely Tunable Lasers," in IEEE Journal of Quantum Electronics, vol. 58, no. 4, pp. 1-10, Aug. 2022, Art no. 6300110, doi: 10.1109/JQE.2022.3168041.

5. **P. Verrinder** et al., "Widely Tunable 1030 nm Gallium Arsenide Sampled Grating Distributed Bragg Reflector Lasers and Photonic Integrated Circuits," 2022 Optical Fiber Communications Conference and Exhibition (OFC), San Diego, CA, USA, 2022, pp. 1-3.

6. **P. Verrinder** et al., "SGDBR tunable laser on gallium arsenide for 1030 nm lidar applications," 2021 27th International Semiconductor Laser Conference (ISLC), Potsdam, Germany, 2021, pp. 1-2, doi: 10.1109/ISLC51662.2021.9615662

7. **Verrinder, P**., Wang, L., Fridlander, J., Sang, F., Rosborough, V., Nickerson, M., ... and Klamkin, J. (2021, July). Gallium Arsenide Photonic Integrated Circuit Platform for 1030 nm Applications. In Integrated Photonics Research, Silicon and Nanophotonics (pp. ITu4A-5). Optica Publishing Group.

8. **P. A. Verrinder** et al., "Gallium Arsenide Photonic Integrated Circuit Platform for Tunable Laser Applications," in IEEE Journal of Selected Topics in Quantum Electronics, vol. 28, no. 1: Semiconductor Lasers, pp. 1-9, Jan.-Feb. 2022, Art no. 6100109, doi: 10.1109/JSTQE.2021.3086074.

9. J. Fridlander, V. Rosborough, F. Sang, M. Nickerson, J. Chen, K. Numata, **P. Verrinder**, F. Gambini, S. Pinna, S. Kawa, M. Stephen, L. Coldren, and J. Klamkin, "Photonic Integrated Circuits for Precision Spectroscopy," in Conference on Lasers and Electro-Optics, OSA Technical Digest (Optica Publishing Group, 2020), paper SF3O.3.

Abstract

Gallium Arsenide Lasers and Monolithic Integration on Silicon

by

Paul Austin Verrinder

The integration of active and passive optical components on-chip is critical for reducing size, weight and power, and realizing useful photonic integrated circuits (PICs). III-V substrates allow for monolithic integration of actives and passives, since both can be realized with the same material system. Indium phosphide (InP) PICs in particular have reached the highest level of maturity, owing to their utility in fiber-connected communication systems. However the lower wavelength limit is around 1.2 µm and InP substrates are costly. Silicon photonics (SiPh) has emerged in recent decades as the preferred PIC platform for high volume applications. Thanks to its compatibility with standard complimentary metal oxide semiconductor (CMOS) processing, SiPh can be manufactured at very low cost, compared to InP. PICs on silicon (Si) have demonstrated extremely low loss waveguides, and high performance passive devices. However, the lack of optical gain on Si limits its utility. Heterogeneous integration approaches, such as wafer bonding or die bonding, have sought to bridge this gap by incorporating InP gain blocks on SiPh to take advantage of the best of both. Direct heteroepitaxial growth of III-V materials on Si is the long-term goal and has the potential to create the most robust and cost effective active-passive integration solution. This technology is, however, still relatively immature compared to heterogeneous integration.

In the first part of this thesis, a monolithic active-passive integration platform on gallium arsenide (GaAs) is proposed and demonstrated. This PIC platform extends the wavelength of monolithic PICs down to 1030 nm. Fabry-Perot (FP) and widely tunable

lasers were both demonstrated on this platform. FP laser performance is consistent with state-of-the-art, demonstrating injection efficiency of 98%, and output power in excess of 240 mW for broad area lasers, with low threshold current density of 94 A/cm^2. Tunable lasers demonstrated greater than 20 nm of continuous wavelength tuning, with over 30 mW of output power. In the second part of this thesis, GaAs quantum dot (QD) lasers are demonstrated on Si by direct metalorganic chemical vapor deposition (MOCVD) heteroepitaxy. MOCVD growth is advantageous for high volume applications, and this is the first demonstration of electrically pumped QD lasers grown entirely by MOCVD on Si. Notable progress is also demonstrated towards realizing electrically pumped lasers on patterned Si by MOCVD selective area heteroepitaxy (SAH). SAH lasers would enable efficient coupling from III-V to Si and provide the clearest long-term path towards process integration with SiPh.

Contents

Curriculum Vitae **vii**

Abstract **ix**

List of Figures **xiii**

List of Tables **xx**

1 Introduction **1**

1.1 Background and Motivation 2
1.2 Brief Review of Photonic Integrated Circuits 4
1.3 Gallium Arsenide Lasers and Photonic Integrated Circuits 10
1.4 Thesis Overview 16

2 Review of Photonic Integration Technology **17**

2.1 Monolithic Active-Passive Integration on III-V Substrates 17
2.2 III-V Integration on Silicon 20
2.3 Summary 30

3 Active-Passive Integration on Gallium Arsenide **32**

3.1 Active-Passive Epitaxy Design 32
3.2 Device Fabrication 35
3.3 Device Testing and Characterization 37

4 Widely Tunable GaAs Lasers **49**

4.1 Sampled Grating Distributed Bragg Reflector Mirrors 51
4.2 Tunable Laser Design 53
4.3 Tunable Laser Fabrication 59
4.4 Laser Measurements 65
4.5 Laser Packaging and Collaboration with Freedom Photonics 70

5 Wavelength Tuning Mechanisms in GaAs **73**
5.1 Refractive Index Tuning 74
5.2 Analysis of Tuning in GaAs SGDBR Lasers 84
5.3 Time Resolved Photoluminescence on GaAs/AlGaAs Regrowth Samples . 87
5.4 Summary 92

6 III-V Lasers on Planar Silicon by MOCVD Heteroepitaxy **94**
6.1 Properties of Quantum Dot Active Regions 94
6.2 MOCVD Grown InAs/GaAs Quantum Dots 98
6.3 Gallium Arsenide Growth on Planar Silicon 100
6.4 Laser Fabrication 103
6.5 Laser Testing and Characterization 108

7 III-V on Silicon by MOCVD Selective Area Heteroepitaxy **113**
7.1 MOCVD Selective Area Heteroepitaxy 114
7.2 Fabrication Process Development 121
7.3 Selective Area Heteroepitaxy Device Fabrication 124
7.4 Next Steps for Lasers in Recess 135
7.5 Coupling to SiN Waveguides: Simulation 138

8 Summary and Future Work **142**
8.1 Summary of Accomplishments 143
8.2 Future Work 144

Bibliography **147**

List of Figures

1.1 Total sales of optical transceivers on different material platforms from LightCounting Silicon Photonics Report [43]. 4
1.2 Energy bandgap vs. lattice constant for common compound semiconductors. 6
1.3 Common building blocks for open-access InP based PIC platforms. Figure adapted from [4]. 7
1.4 APSUNY 300 mm SOI PDK under AIM Photonics [57]. 8
1.5 335 W fiber coupled diode pump laser module from Lumentum [70]. . . . 12
1.6 Schematic cross-section of a typical VCSEL and SEM image of oxide aperture in the upper mirror. Figure from [72]. 13
1.7 Side view diagram of a four section sampled grating distributed Bragg reflector (SGDBR) laser with active and passive waveguide sections. . . . 14

2.1 Common III-V active-passive integration techniques including (a) offset quantum well (OQW), (b) quantum well intermixing (QWI) and (c) butt-joint regrowth. 18
2.2 Co-packaged micro-optical system with an InP tunable laser coupled to a SiPh chip. Figure adapted from [19]. 21
2.3 Hybrid assembly for co-packaging InP laser array and silicon photonic transmitter using photonic wirebonds. Figure adapted from [21]. 22
2.4 GaSb RSOA gain chip edge coupled to SiN PIC to create a hybrid laser. Figure adapted from [83]. 23
2.5 Micro-transfer printing of III-V laser coupons on silicon photonics wafer. Figure adapted from [16]. 24
2.6 Evanescently coupled InP laser on silicon. Figure adapted from [14]. . . . 24
2.7 V-Groove patterned (001) Si to expose the (111) face in preparation for III-V heteroepitaxial growth. 27
2.8 Example of cracking on GaAs surface due to thermal expansion mismatch between GaAs and the underlying Si substrate. 28
2.9 Examples of lasers monolithically grown on silicon. (a) MOCVD grown 1550 nm QW laser [84] and (b) MBE grown QD laser on MOCVD grown buffer [58]. 29

3.1 Photoluminescence spectrum of epitaxial material prior to fabrication and regrowth . . . 34
3.2 Fundamental TE mode in (a) active and (b) passive sections for a 3 µm wide rib waveguide. . . . 35
3.3 Summary of primary fabrication steps including (a) initial epitaxial layers, (b) active-passive etch, (c) upper cladding and p-contact layer regrowth, (d) ridge waveguide etch, (e) surface passivation and p-contact via opening, (f) p-metal and n-metal contact formation. . . . 36
3.4 SEM image of (a) etched active-passive transition prior to regrowth, (b) active side cleaved facet of 3 µm wide fabricated laser, and (c) top view microscope image of completed devices, showing an all-active FP laser and an active-passive FP laser. The notches in the metal are spaced 200 µm apart and were placed as a visual aid for cleaving. . . . 37
3.5 Light-current characteristics for (a) 20 µm wide by 800 µm long broad area laser and (b) 600 µm long lasers between 2 µm and 5 µm wide under CW current injection. . . . 39
3.6 (a) LI characteristics for active-passive lasers with 400 µm long active section and 400 µm long passive section. (b) Side-view schematic diagram of a generic active-passive laser cavity. . . . 40
3.7 Inverse differential efficiency as a function of cavity length for 20 µm wide broad area lasers under pulsed current operation and linear fit to extract loss and efficiency. . . . 41
3.8 (a) Simulated η_d as a function of passive section length for varying passive loss from 0 cm^{-1} to 10 cm^{-1} in 3 µm wide active-passive FP lasers with 400 µm long gain sections. (b) Measured η_d points with curve fit to extract $\alpha_{ip} = 4.05$ cm^{-1}. . . . 43
3.9 Material gain as a function of current density for three 5 nm $In_xGa_{1-x}As$ (x=0.271) QWs with 8 nm $Ga_{1-x}AsP_x$ (x=0.1) barriers, obtained from 20 µm wide lasers measured under pulsed current operation. . . . 44
3.10 Threshold current and single-sided differential efficiency as a function of temperature for a 20 µm wide, 400 µm long broad area laser. Measurements were performed with pulsed current to mitigate self-heating, while the stage temperature was varied from 20 °C to 70 °C. . . . 46
3.11 Lasing spectra for 3 µm wide active-passive laser with 400 µm long gain section and 400 µm long passive section under various levels of CW current injection. . . . 47
3.12 Lasing spectra with varying temperature for 3 µm wide devices at 40 mA CW current injection. . . . 48

4.1 Schematic diagram of NASA's ICESat over the Arctic. Figure adapted from [39]. . . . 50

4.2 (a) Four section SGDBR laser with close-up view of SGDBR mirror and (b) example of simulated reflectivity spectrum for a single SGDBR mirror. 52
4.3 Side view diagram of a four section SGDBR laser. 54
4.4 Diagram of grating period and corresponding **T**-matrices. 56
4.5 (a) Fundamental mode effective index vs. wavelength for a 35 nm deep grating etch and (b) coupling constant κ vs. etch depth. 57
4.6 (a) Simulated reflectivity spectra of front and back SGDBR mirrors for design 6, (b) total reflectivity sepctrum for laser design 6, and (c) microscope image of fabricated laser with section lengths indicated. 59
4.7 Cavity mode spacing overlaid on total mirror reflectivity spectrum of design 6 showing effective mode filtering capability. 60
4.8 (a) Mask layout and (b) microscope image of fabricated die with close up of four section SGDBR laser in inset. 61
4.9 (a) Top-view SEM of etched gratings, (b) cross-section SEM image of gratings, and (c) AFM image showing 37 nm etch depth. 62
4.10 FIB cut and STEM image of the gratings after regrowth. 63
4.11 (a) Microscope image of cleaved four section SGDBR laser bar mounted and wirebonded to AlN carrier and (b) side view SEM of a similar device also mounted and wirebonded. 64
4.12 LIV characteristic from SGDBR laser design number 6 after antireflection coating and mounting to AlN carrier. Optical power shown here is only out of the front mirror facet and exhibits more than 35 mW output at 100 mA CW current injection. 65
4.13 Total power output while varying mirror current from 0 to 150 mA in (a) front mirror, (b) back mirror and (c) both mirrors simultaneously. 66
4.14 (a) Overlaid spectra of 8 channels accessible with coarse tuning and (b) demonstration of continuous tuning between the first and second channels with current injection into both mirrors. 68
4.15 (a) Map of wavelength vs. front and back mirror current and (b) SMSR vs front and back mirror current. 69
4.16 (a) Peak wavelength vs. phase section current and (b) overlaid spectra with varying phase section current and no mirror tuning. 69
4.17 (Left) Butterfly package with fiber coupled output from Freedom Photonics and (right) InstaTune module for wavelength tuning measurements. . 70
4.18 Tuning map showing wavelength versus front and back mirror current for one of the packaged SGDBR lasers. 71
4.19 Screenshot of oscilloscope waveform during wavelength switching experiment using 200 µs pulses. Fast rise time and slow decay indicate two different time constants affecting the wavelength tuning speed. 72

5.1 n-k data for GaAs 74

5.2 Carrier induced refractive index change in GaAs due to (a) bandgap shrinkage, (b) band filling, and (c) free carrier absorption. The vertical line in all three plots is at 1.204 eV which corresponds to a wavelength of 1030 nm. 79
5.3 (a) Calculation of change in refractive index versus carrier density for GaAs and (b) similar data calculated in [109] for n-type GaAs. 80
5.4 Calculated Δn versus carrier density in InP at two different wavelengths from [109]. 80
5.5 Δn versus reverse bias in the AlGaAs/GaAs/AlGaAs heterostructure described in [110]. 82
5.6 Refractive index vs. temperature of GaAs and AlAs at a photon energy of 1.2 eV. Figure adapted from [116]. 84
5.7 Contour map of wavelength versus front and back mirror current in 1030 nm SGDBR laser. 85
5.8 Wavelength change versus passive section current: experimental results for two different structures (left), and theory for the SQW structure (right) with varying SRH lifetimes and taking into account self-heating. Figure adapted from [102]. 86
5.9 (left) Simulated and measured IV curves and optical mode profile in mirror section and (right) simulated heat map at 130 mA for two different SRH lifetimes. 87
5.10 Index change versus mirror section current: (a) without self-heating and (b) with self-heating. 88
5.11 Epitaxy for regrowth tests. 90
5.12 870 nm emission vs time for (a) A samples, (b) B samples and (c) C samples. 980 nm emission vs time for (d) A samples, (e) B samples and (f) C samples. 91
5.13 1/e lifetime extracted from TRPL measurements for (a) 980 nm emission for QWs and (b) 870 nm emission from GaAs. 92

6.1 Effect that increasing electron confinement has on the density of states. Figure adapted from [74] 95
6.2 (a) MOCVD grown QD lasers on native GaAs with varying ridge widths and (b) broad area laser LI characteristics with varying temperature. Figures adapted from [87]. 100
6.3 InAs/GaAs QD growth development on GoVS template showing (left) layer schematic and AFM scan of QD surface with extracted dot density of $\sim 5 \times 10^{10}$ cm^2 and (right) PL emission comparing QDs on GoVS and native GaAs with emission peak near 1.3 µm. Figure adapted from [85]. . 101
6.4 GoVS template and growth results showing annihilation of APBs and threading dislocations in the buffer layer. Figure adapted from [85]. . . . 102
6.5 (a) QD laser epitaxial layers grown by MOCVD on GoVS template, and (b) measured QD PL spectrum. 103

6.6 (a-e) InGaP dry etch recipe waveguide etching results from recipes 1-5 showing that recipe 5 (e) has the lowest roughness and most vertical sidewalls. 105
6.7 Summary of fabrication steps for Fabry-Perot ridge lasers using GoVS template on planar silicon. 106
6.8 (a) Tilted SEM image of waveguide etch, (b) cross-section SEM of cleaved facet laser after fabrication and (c) top-view microscope after p-contact deposition showing relative alignment to thermal cracks, and (d) microscope image of fabricated lasers. 107
6.9 LIV characterstic for (a) 4 µm wide, 1850 µm long ridge laser under both CW and pulsed current operation and (b) LI characteristic under pulsed current for a 20 µm wide, 1600 µm long broad area laser. 108
6.10 (a) Inverse differential efficiency versus cavity length to extract internal loss and injection efficiency for 4 µm wide lasers and (b) pulsed current LI curves associated with the data points in (a). 109
6.11 (a) CW current LI characteristic and (b) pulsed LI characteristic with varying temperature. 111
6.12 Lasing spectra at (a) just above threshold current and (b) at 5 times threshold for a 4 µm wide QD laser on Si. 112

7.1 Selective area heteroepitaxy III-V laser stack showing vertical alignment to SiN waveguide layers. In this approach light is first coupled to SiN and can then be transitioned to the lower Si waveguide. 115
7.2 Examples of QD microdisk lasers grown by MOCVD SAH and presented at the International Semiconductor Lasers Conference (ISLC) 2022 [140]. Both flat-bottom Si and nano V-groove Si templates were used, with noticeable performance benefits for the V-groove Si devices. Figure adapted from [140]. 117
7.3 (a) n-GaAs contact layer grown on GoVS by SAH with metal contact pad, (b) layout for TLM measurements, (c) IV curves for different pad spacings on one TLM device and (d) resistance versus metal pad spacing for all 4 TLM devices. 119
7.4 (a) Electron mobility in GaAs vs doping concentration adapted from [149], and (b) GaAs resistivity vs doping from [150] 120
7.5 Epitaxial layers for a typical laser structure grown by MOCVD SAH, using a GaP-on-Si template. The SiN (SN, and FN) and Si (SE) waveguides shown here only indicate the vertical position of these layers in the AIM Photonics process; their horizontal position relative to the III-V layer stack depends on device design. 121
7.6 Wet etch process to remove parasitic III-V particles that form on SiO_2 during growth without damaging the epitaxial layers in the recess. 122

7.7 (a) Microscope image of III-V particles on sample surface with PR protecting the III-V material in the recesses; (b) SEM image of a single particle; (c) III-V particles before etching and (d) the same area on the sample after wet etching in HCl:H_3PO_4:H_2O_2 solution 123
7.8 (a) Mask layout showing III-V recesses and close-up of III-V laser-in-recess layout in the inset. (b) Photograph of diced sample after MOCVD III-V growth using GaP-on-Si template, but before device fabrication. 125
7.9 Overview of fabrication process for selective area heteroepitaxy devices grown in a recess, after removal of parasitic III-V growths. 126
7.10 SEM images of (a) waveguide ridge after etching, (b) top-view after probe metal deposition, (c) cleaved facet after fabrication. Microscope images of (d-e) III-V material in recesses after p-contact but before ridge etch, and (f) fully fabricated devices before cleaving. III-V material grown on the GaP-on-Si template. 127
7.11 PL emission measured for SAH QWs with peak around 980 nm, and strongest PL from 20 µm wide recesses. QW epitaxy grown on a GaP-on-Si template. 128
7.12 Electrical measurements on SAH QW diodes. (a) N- and P-contact measurements showing ohmic contacts with reasonably low resistance, and (b) diode IV curve demonstrating very high series resistance due to phase separation in InGaP cladding layers. 129
7.13 III-V layer structure and corresponding diode IV curves for (a) GaAs PiN junction, (b) full laser stack excluding p-InGaP cladding and (c) full laser stack excluding n-InGaP cladding. All three structures utilized the GaP-on-Si growth template. 131
7.14 Measured PL emission from SAH QDs with peak wavelength around 1230 nm, and strongest emission from 30 µm wide recess. QD epitaxy grown on GaP-on-Si template. 132
7.15 (a) N- and P-contact measurements on TLM patterns and (b) diode IV curve demonstrating reasonable series resistance in linear region but slow turn-on. Slight improvement with contact burn-in shown in inset. (c) IV curve from fab 1 QW devices for comparison. 132
7.16 (a) Picture of cleaved device under test and (b) QD emission observed on camera. (c) LIV curve for cleaved facet device under CW operation demonstrating LED behavior but no lasing. 133
7.17 (a) FIB cut and cross section TEM in center of recess after full device fabrication. (b) Close-up showing clear phase separation in InGaP, and EDX mapping of (c) Ga and (d) In elements. 135
7.18 (a) TEM analysis of defective InAs clusters and cascading dislocations in the upper InGaP cladding. (b) Evidence of stacking faults (SF) and antiphase boundaries (APBs) in the n-GaAs layer contributing to phase separation of lower InGaP. 136

7.19 (a) Potential new epitaxy design with AlGaAs upper and lower cladding, (b) cross section of the grown structure showing some polycrystalline AlGaAs deposition on the oxide, and (c) TEM image of the structure showing very flat layers, with no phase separation and minimal dislocations. . . . 137
7.20 Zero-gap interface between III-V and SiO_2 for III-V laser stack grown by MOCVD SAH. 139
7.21 (a) Top-view schematic of III-V ridge in a recess coupling to SiN waveguides, with corresponding cross-sectional mode profiles shown below. (b) Simulated coupling loss due to mode mismatch versus SiN waveguide width. Simulation assumes zero gap between III-V and SiN. 140
7.22 (a) 3D FDTD simulation to mimic faceting effects in the true geometry. (b) Sweep of coupling efficiency versus gap distance compared to results from (a). 141

List of Tables

2.1 Comparison of PIC Material Platforms 31

3.1 Epitaxial Layers for Active-Passive Integration 33

4.1 Laser Specifications 50
4.2 Front Mirror Parameters. 57
4.3 Back Mirror Parameters 57
4.4 Total Mirror Parameters. 58
4.5 Regrowth Layers for SGDBR Laser 62

5.1 GaAs/AlGaAs Regrowth Sample Information 89

6.1 InGaP Dry Etch Recipes 104

7.1 Fabrication Runs 124

Chapter 1

Introduction

Photonic integrated circuits (PICs) have become increasingly commonplace for a wide variety of applications across multiple fields. The original concept for PICs was envisioned in 1969 [1] (then known as integrated optics), shortly before the first demonstration of room temperature continuous wave (CW) lasing in a double heterostructure (DH) laser in 1970 [2, 3]. In the following decades, advances in semiconductor growth and manufacturing techniques led to steady improvements in semiconductor lasers, and enabled other optical components such as amplifiers, detectors, passive waveguides, and modulators to be integrated on-chip. The steady increase in integration density led to increasingly complex PICs while still reducing cost and size, mirroring Moore's law in microelectronics [4–10]. Indeed Miller's original prediction that by integrating multiple optical components in a small form-factor "economy should ultimately result" has proven accurate [1].

In this work, the focus is specifically on gallium arsenide (GaAs) based lasers and PICs and their integration with silicon photonics. The first section in this chapter provides background and motivation for the work, highlighting various applications for PIC technology. Following this, a brief review of PICs in general is presented in section 1.2. Section 1.3 provides an overview of GaAs based lasers and PICs, relevant to the work that is carried out in this thesis and the final section contains an overview of the entire

thesis.

1.1 Background and Motivation

One of the primary applications for PIC technology is high bandwidth optical communications [11, 12]. As a result, indium phosphide (InP) quickly became the most mature monolithic, active-passive PIC platform since the bandgap wavelengths of InP-related materials encompass the low loss window of optical fiber between 1.3 µm and 1.55 µm, and its direct bandgap enables efficient light emission making InP suitable for lasers. Significant efforts have been undertaken, with considerable success, to integrate InP lasers with silicon photonics (SiPh) via hybrid and heterogeneous techniques to leverage the advantages of high volume, low cost silicon (Si) manufacturing enabled by the complimentary metal oxide semiconductor (CMOS) electronics industry [13–21]. Intel, for example, is now mass producing heterogeneously integrated InP on silicon transceivers and shipping millions of units per year [17, 22]. In addition to InP, GaAs based lasers are also widely used for optical communications. Vertical cavity surface emitting lasers (VCSELs) on GaAs are commonly used for high speed optical interconnects near 850 nm [23], and GaAs based quantum dot lasers are employed for O-band communications around 1.3 µm [24].

While optical communication remains one of the largest markets, the inherent advantages of integration, namely the reduction in cost, size, weight and power (CSWaP), make PICs an ideal candidate for a wide variety of other applications. These include biosensing [25], high-performance computing and deep learning [26–29], optical phased arrays for beam steering [30, 31], light detection and ranging (lidar) [32, 33] and 3D sensing. In addition to the more consumer oriented applications for lidar, such as automotive or even the 3D sensors that are now used in Apple's iPhone, there is growing inter-

est in deploying PIC-based lidar systems on satellites for gas sensing and topographical mapping [32–35]. For space-based applications in particular, reduction of CSWaP is critical and enables previously bulky optical systems [36–39] to be integrated on-chip for potential deployment on small satellites.

While many of the aforementioned applications can leverage the spectral range offered by InP lasers, such as CO_2 gas sensing lidar which utilizes 1572 nm [32], others require wavelengths outside this range. GaAs is an alternative to InP for developing a monolithic PIC platform that has access to wavelengths near 1 µm by making use of indium gallium arsenide (InGaAs) quantum wells (QWs) for the active region [35,40]. The development of a tunable active-passive PIC platform on GaAs, specifically for lidar applications near 1030 nm, represents a significant portion of the work presented in this thesis.

In addition to monolithic PICs, GaAs is also a candidate for integration on silicon thanks to the development of QD active regions which extend the wavelength of GaAs into silicon's transparency window and out to 1.3 µm. Although it is also worth mentioning that with the use of silicon nitride (SiN) waveguides, the transparency window of silicon photonics platforms in general can be greatly expanded. SiN is transparent all the way down into the visible and near ultra-violet (UV) range whereas silicon is absorbing at wavelengths shorter than ∼1.1 µm [41]. Heterogeneous integration of GaAs lasers on SiN platforms has been demonstrated with operation around 990 nm, which is below the Si bandgap [42]. Many of the heterogeneous integration approaches that are commonly used for InP lasers on Si could also be employed for GaAs lasers on Si. And indeed, there are some potential advantages owing to the lower cost and larger size of GaAs wafers compared to InP. However, the focus of the work presented later in this thesis is on integration via direct growth, or heteroepitaxy. For this application, GaAs is generally preferred over InP, as will be discussed in later sections.

1.2 Brief Review of Photonic Integrated Circuits

In terms of photonic integration and total sales, InP and silicon are currently the two dominant material platforms in the industry. Fig. 1.1 shows the total sales of optical transceivers, projected out to 2028 and split up by material platform, from the recent silicon photonics report released by LightCounting [43]. InP and Si clearly dominate. Lithium niobate ($LiNbO_3$, LN) represents a small fraction and bulk $LiNbO_3$ is predicted to be replaced by thin film $LiNbO_3$ (TFLN), which is often deposited on Si substrates [44]. GaAs represents the remaining, relatively small fraction. A brief overview of these platforms is presented in this section and further details regarding integration techniques will be covered in chapter 2.

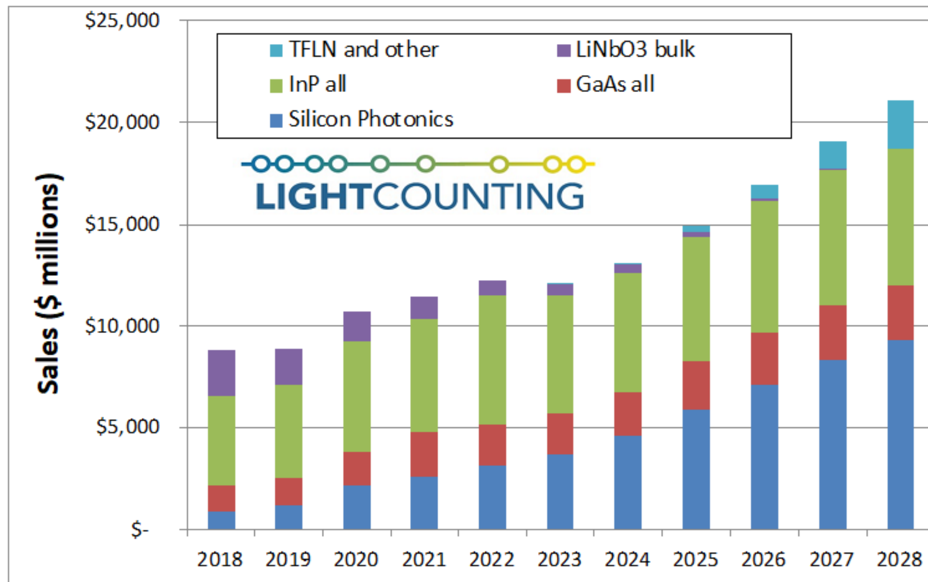

Figure 1.1: Total sales of optical transceivers on different material platforms from LightCounting Silicon Photonics Report [43].

1.2.1 Indium Phosphide

Direct bandgap group III-V compound semiconductors, such as InP and GaAs, provide a suitable platform for monolithic PICs. Various quaternary alloys such as indium gallium arsenide phosphide (InGaAsP) and indium aluminum gallium arsenide (InAlGaAs) have bandgap wavelengths in the 1.1-1.6 µm range and can be grown lattice matched to InP [45, 46]. Fig. 1.2 shows a plot of energy bandgap (wavelength) versus lattice constant for various compound semiconductors. The ability to tune both bandgap (and thus emission wavelength) and refractive index with quaternay alloy composition while still maintaining the lattice-matching condition, has led to a wide variety of both active and passive components being monolithically integrated on InP substrates. These include lasers, amplifiers, modulators, photodetectors, splitters, couplers, passive waveguides, and others. The flexibility in component design, and the fact that the wavelength range is compatible with the loss and dispersion minima of optical fiber, led to InP becoming the material of choice for monolithic active-passive PICs. Indeed high performance system-on-chip InP PICs have been demonstrated for a wide variety of applications from high speed transmitters and receivers, to gas sensing lidar [5, 32, 47].

With the maturation of PIC technology, foundries began to develop generic processes for InP fabrication and release process design kits (PDKs) [4, 9]. Making the foundry process accessible via PDKs and multi-project wafer (MPW) runs significantly reduces the barrier to entry for small companies and academics trying to prototype custom PIC designs. This relative accessibility led to a much wider variety of application specific PICs. Fig. 1.3 shows some of the common building blocks available in a generic open-access InP platform (figure adapted from [4]).

In spite of the advances made over the past decades, there are still some drawbacks to InP. One downside is cost: the wafers are significantly more expensive than Si and tend

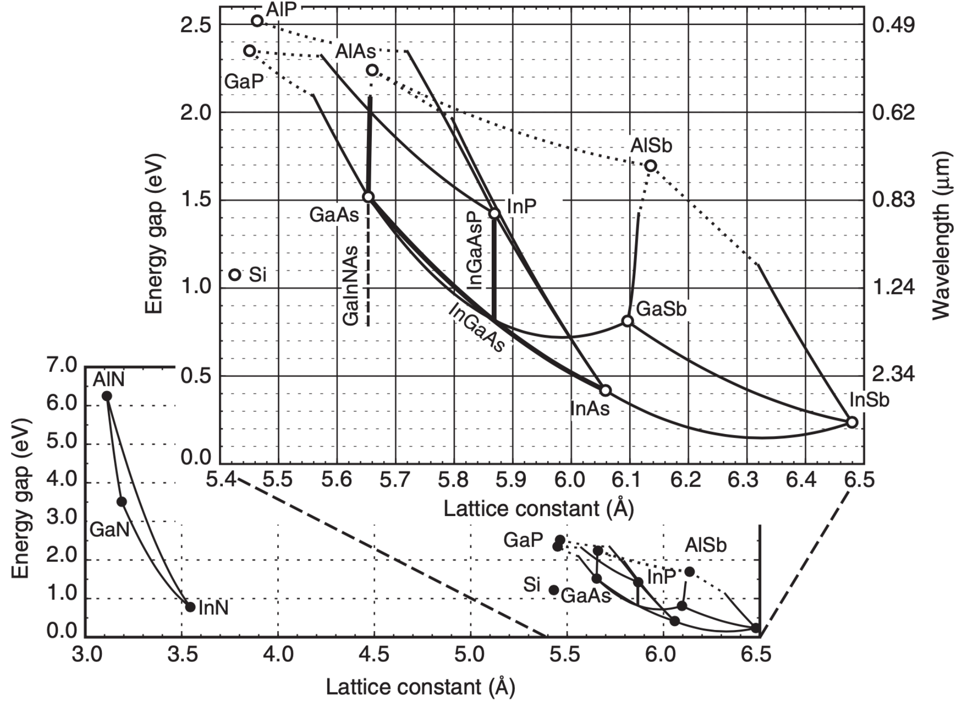

Figure 1.2: Energy bandgap vs. lattice constant for common compound semiconductors.

to be more costly than GaAs as well [48]. The small wafer size, which is limited to 4” for InP, also leads to higher overall manufacturing cost since fewer die can be placed on an individual wafer. 300 mm is the industry standard for Si and GaAs can be grown on 6” and even 8” wafers making both of these platforms more cost-effective when scaling to high-volume. Additionally, the passive losses in InP based waveguides are higher than in Si or SiN waveguides, and the relatively lower index contrast between core and cladding limits the bending radius. InP waveguides are limited to a minimum bending radius of greater than 10 µm for deeply etched ridges, while on SiPh platforms this can be as low as 2.5 µm [49,50]. Tighter waveguide bends lead to smaller overall device footprint which makes Si preferable in terms of integration density, as well as cost.

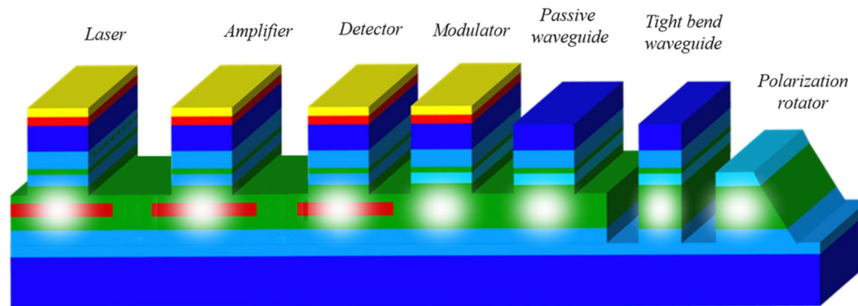

Figure 1.3: Common building blocks for open-access InP based PIC platforms. Figure adapted from [4].

1.2.2 Silicon Photonics

Silicon photonics (SiPh) leverages the mature, high volume manufacturing processes used for CMOS electronics. This enables mass production of SiPh chips on 300 mm silicon on insulator (SOI) substrates at very low cost. SiN can also be used as a passive waveguide material, is easily deposited on Si substrates, and is compatible with CMOS processing. Both Si and SiN waveguides exhibit lower loss than either InP or GaAs waveguides. Typical propagation loss in Si is around 0.1 dB/cm to 1 dB/cm [51] and for SiN waveguides this can be as low as 0.1 dB/m (0.001 dB/cm) [52, 53]. Additionally, the high index contrast between Si or SiN and the surrounding oxide cladding leads to tightly confined waveguide modes enabling very tight bend radii (as low as 2.5 µm), which in turn leads to higher overall integration density. These low-loss and high confinement waveguides enable a variety of robust and compact passive components such as multi-mode interference (MMI) couplers, grating couplers, ring resonators, loop mirrors, and others. In addition to passive devices, some active components, such as doped Si modulators and germanium (Ge) photodetectors are also supported on SiPh platforms.

There are multiple commercial foundries that offer PDKs and MPW runs, just as with InP, making SiPh design and fabrication accessible to both academia and industry for

research and other small-scale projects. AIM Photonics, for example, offers both active and passive SiPh PIC platforms on 300 mm SOI [54]. Other companies with PDKs and SiPh MPW runs include VTT which offers a thick SOI waveguide platform [55], and GlobalFoundries [56]. Fig. 1.4 highlights some of the capabilities of AIM Photonics' 300 mm SOI platform using the Analog Photonics APSUNY PDK [57].

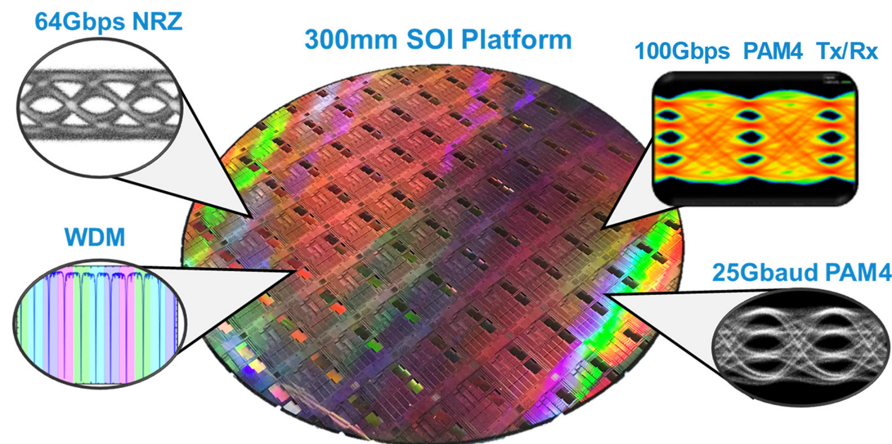

Figure 1.4: APSUNY 300 mm SOI PDK under AIM Photonics [57].

The major downside to SiPh of course, is that Si is an indirect bandgap semiconductor making it unsuitable for light emission. As a result, significant efforts have been undertaken to combine InP lasers and active devices with SiPh to take advantage of the best of both.

1.2.3 III-V Integration on Silicon

Various techniques have been proposed for integrating III-V gain material with Si to take advantage of both the efficient light emitting properties of direct bandgap III-Vs

and the low cost, high volume production of silicon. A brief overview of these techniques is provided here and will be discussed in greater detail in chapter 2.

One approach is co-packaging, where the III-V laser and SiPh chips are fabricated separately and then assembled in the same package. This technique avoids co-fabrication of III-V and SiPh and so doesn't sacrifice individual device performance. However, the precise alignment requirements and high assembly and packaging costs severely limit scalability. An alternative approach is to bond fully fabricated III-V devices to silicon at the wafer level before dicing. This approach eliminates some of the packaging costs associated with co-packaged optics since it is accomplished at wafer scale, but still requires precise alignment of individual chips. Yet another approach is to bond entire III-V wafers epi-side down to the SOI, remove the III-V substrate and then fabricate devices directly on the SOI. This technique allows for lasers to be lithographically aligned to existing devices on the SOI and fabricated at 300 mm wafer scale. Wafer bonding is the most scalable of the aforementioned techniques, however, it results in significant material waste as most of the III-V substrate is simply removed after bonding.

The final approach, and the one utilized in the latter portion of this thesis, is monolithic integration via direct growth, or heteroepitaxy, of III-V gain material on Si. Heteroepitaxy has been the ultimate goal of III-V on Si integration for many years as it would allow III-V growth at 300 mm scale, eliminates all excess packaging and assembly costs associated with co-packaging and chiplet bonding, and eliminates the bonding step and material waste associated with wafer bonding. However, achieving monolithically grown III-V material on Si with sufficiently low defect density has been, and remains, a major hurdle to overcome. Quantum dot (QD) active regions are particularly attractive for heteroepitaxy, as QDs are less sensitive to defects such as threading dislocations, compared to their QW counterparts. InAs/GaAs QD lasers on silicon have been demonstrated with low threshold current and good thermal performance [58, 59]. However,

growing high quality laser material on Si typically requires growth of a thick buffer layer which serves to trap defects. This presents a challenge in terms of integration because the laser epi layers are separated from the SiPh by a thick layer of highly defective material making coupling difficult or impossible. One solution is to grow the III-V in a deep trench, or recess, etched through the oxide layer and down to the Si substrate, which places the buffer layer well below the SiPh device layers and allows for alignment of the active waveguide with SiPh waveguides. Currently, many heteroepitaxially grown laser results have been achieved using molecular beam epitaxy (MBE) grown device layers on a metalorganic chemical vapor deposition (MOCVD) grown template. However, MOCVD is generally preferred in the industry for high-volume production and it would be advantageous to realize both the template and laser epitaxy with a single growth technique. Additionally, selective area heteroepitaxy (SAH) can be realized by MOCVD for growing in trenches [60, 61].

1.3 Gallium Arsenide Lasers and Photonic Integrated Circuits

GaAs based lasers have a long history that extends back to the very first demonstration of CW, room temperature lasing with a GaAs/AlGaAs double heterostructure laser [2, 3]. Now diode lasers on GaAs represent some of the most efficient light sources in existence, and are capable of demonstrating very high output powers. GaAs based lasers usually come in the form of discrete devices, and some of the most common are high power diode pump lasers, vertical cavity surface emitting lasers (VCSELs), and directly modulated QD lasers.

1.3.1 High Power Laser Diodes

High power laser diodes are useful for many optical systems. With high optical power and beam quality, these devices can be used for various industrial manufacturing, machining, and material processing applications [62], as well as space-based systems, and lidar [63]. GaAs based lasers are particulary attractive for high power as they have demonstrated some of the highest efficiencies of any light source [64, 65]. External efficiency greater than 70% with output powers in excess of 10 W from individual GaAs lasers are fairly accessible [64, 66]. By combining multiple devices in laser bars and stacks of bars, GaAs-based diode sources can yield output power in the kilowatt range. Laser diodes also provide the pump source for various laser systems that require optical pumping. Again, GaAs lasers are attractive for this as the common pump wavelengths are easily accessible. For example, Nd:YAG lasers, which are used in various industrial, medical and military applications, require an optical pump source at 808 nm or 885 nm [67], and laser-induced fusion research employs solid state lasers pumped with high power diode laser bars in the 87x nm range [68, 69]. Fiber lasers and erbium doped fiber amplifiers (EDFAs), also rely on diode lasers for pumping, typically in the 9xx nm wavelength range. This spectral region is also easily accessible with strained InGaAs QWs on GaAs, making such lasers an indispensible component in telecommunications. Fig. 1.5 shows an example of a typical fiber coupled diode pump laser package from Lumentum [70], which can provide 335 W of fiber coupled output power at a wavelength of 915 nm.

1.3.2 Vertical Cavity Surface Emitting Lasers

VCSELs are comprised of a gain section sandwiched above and below by Distributed Bragg Reflector (DBR) mirrors. The DBR mirrors are epitaxially grown with alter-

Figure 1.5: 335 W fiber coupled diode pump laser module from Lumentum [70].

nating layers of different semiconductor alloys; in the case of GaAs VCSELs, typically $Al_xGa_{(1-x)}As/Al_xGa_{(1-x)}As$ layers of different composition [71]. The laser's optical cavity is then oriented in the vertical direction with the DBR mirrors providing feedback, and emission is normal to the surface (emission can be either from the top or bottom, depending on the design of the gratings). A typical VCSEL structure is shown in Fig. 1.6 (figure adapted from [72]). VCSELs have very high beam quality as the small cavity often supports only one mode, and the shape of the output beam is easily controlled with the design of the oxide aperture, which leads to narrow beam divergence. The narrow divergence and circular beam shape allow for easy coupling to optical fibers. The small cavity also results in very low threshold currents (and thus low power consumption), and high modulation bandwidth. VCSELs are easy to scale to large volumes as the entire structure is monolithically grown, and devices can be tested at the wafer level. Their low power consumption, high bandwidth and manufacturability have made GaAs based VCSELs common for high speed, short reach, optical interconnects at 850 nm. VCSELs can also easily be integrated into 2D arrays, which are used for various sensing applications, including consumer applications such as facial recognition in smartphones [23, 71, 73]

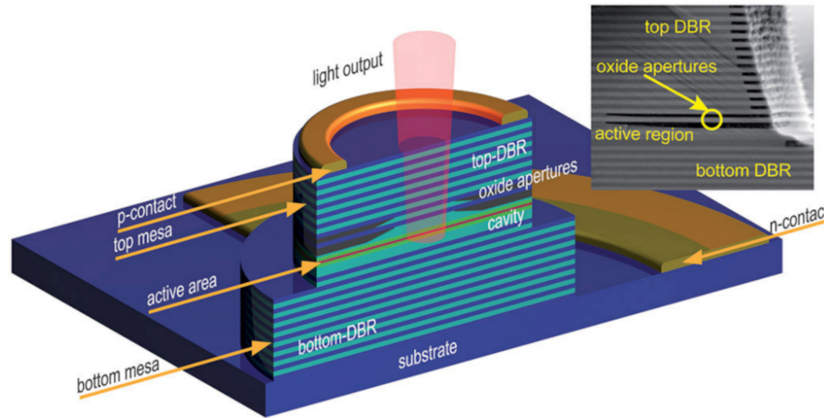

Figure 1.6: Schematic cross-section of a typical VCSEL and SEM image of oxide aperture in the upper mirror. Figure from [72].

1.3.3 Quantum Dot Lasers

With the invention of self-assembled InAs/GaAs QDs, the wavelength of GaAs lasers was extended to 1.3 µm [24, 48, 74], where it was previously limited to shorter than 1.1 µm with strained InGaAs QWs. This positioned GaAs lasers as a useful light source for O-band communications with several advantages over their InP QW based counterparts. The discrete density of states in QDs, which arises from their 3D electron confinement, results in a reduction in threshold current [24]. Lower threshold current leads to lower overall power consumption. QD lasers are also less sensitive to variations in temperature and operate over a wider temperature range than QW lasers, again due to the reduced density of states. Greater thermal stability is beneficial for operation in environments with elevated temperature, and reduces the cost associated with active cooling. QDs also have a broader gain spectrum than QWs, which is particularly relevant for wavelength division multiplexing (WDM) applications. Due to these performance advantages, InAs/GaAs QD lasers emitting at 1.31 µm have become a common light sources for O-band communications. QD lasers have also demonstrated high reliability with MOCVD lasers on GaAs demonstrating extrapolated lifetime of up to five million hours [75].

1.3.4 Prospects for GaAs Photonic Integrated Circuits

High power laser diodes, VCSELs, and QD lasers represent the majority of GaAs based lasers and for the most part these are manufactured as discrete components (or laser bars and VCSEL arrays). The realm of active-passive integration for system-on-chip (SoC) functionality is still largely dominated by InP and SiPh. However, there is growing interest in using PICs for a wider variety of applications that require shorter wavelengths than what InP has to offer, such as topographical lidar and sensing [39, 76]. Some early work on passive devices, specifically phase modulators around 1 µm, demonstrated the utility of GaAs for photonic devices other than lasers and amplifiers [77, 78]. By combining highly efficient GaAs lasers with GaAs passives, robust monolithic PICs could be demonstrated for wavelengths that are inaccessible with InP. A significant portion of this thesis is devoted to the development of just such a platform. Fig. 1.7 shows a schematic of a 1030 nm widely tunable laser demonstrated on GaAs with both active and passive waveguide sections. Parallel efforts at UCSB have already demonstrated optical phased arrays (OPA) for 1030 nm beam steering applications [31]. Ongoing work is being pursued to combine passive OPA PICs with QW gain regions.

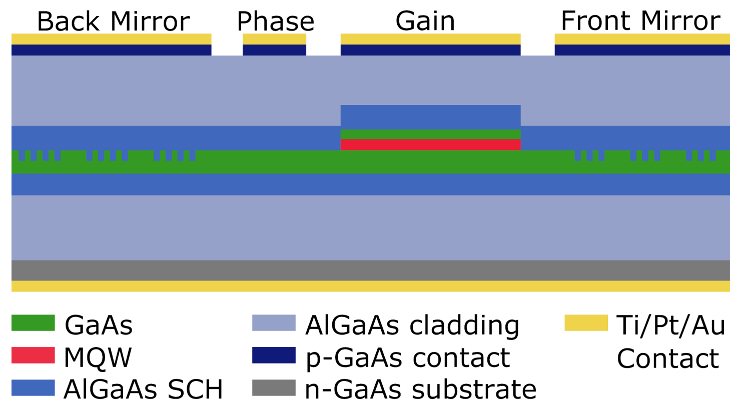

Figure 1.7: Side view diagram of a four section sampled grating distributed Bragg reflector (SGDBR) laser with active and passive waveguide sections.

QWs on GaAs enable wavelengths below 1.1 µm, but by utilizing QDs the wavelength

can be extended to 1.3 μm and beyond. These QD lasers on GaAs already demonstrate high performance and are commonly used as light sources for datacenter communications. In addition to discrete devices, these could potentially be integrated into a monolithic active-passive platform on GaAs to demonstrate SoC PICs for O-band applications. GaAs has an advantage over InP in terms of both wafer size and cost, which further motivates development of GaAs PICs. GaAs can be grown on 6 inch substrates, whereas InP is typically limited to 4 inch; this represents a 2.25x increase in wafer surface area. Additionally, the cost per cm^2 is lower for GaAs substrates [48]. So, strictly based on cost, GaAs-based PICs have an advantage over InP, at least for O-band wavelengths and shorter where optical gain is achievable. GaAs-based RF electronics, such as high electron mobility transistors (HEMTs) are commonplace for many applications, especially in the mobile device market, and represent the largest volume of GaAs-based devices on the market. These are fabricated on 6 inch substrates, so the infrastructure for high-volume production on GaAs is already well established.

In addition to purely monolithic PICs, GaAs based devices can also be integrated with SiPh. The previously described heterogeneous integration techniques regularly used for InP on Si can also be used for GaAs on Si. For example, Tower Semiconductor now offers GaAs QD lasers with its PH18 SiPh foundry platform [79], and heterogeneous integration of GaAs lasers for SiN photonics has been demonstrated [42]. Direct growth of III-Vs on Si is another active area of research as mentioned above and GaAs is generally preferred over InP for several reasons. Lattice mismatch between Si and III-V is a major problem; the mismatch is high in both cases, but significantly more for InP. For this reason the thick buffer and defect trapping layers are almost always GaAs-based. QD active regions are more tolerant to defects than QWs making them preferrable for growth on Si, and InAs/GaAs QDs are the most mature. This positions GaAs based QD lasers as the most promising candidate for monolithic integration on Si in addition to their proven utility

in heterogeneous integration.

1.4 Thesis Overview

The focus of this dissertation is on GaAs based lasers for monolithic active-passive integration enabled by MOCVD growth. The work is split into two main efforts. Firstly, the development of a fully monolithic active-passive PIC platform with widely tunable lasers on native GaAs. And secondly, all-MOCVD grown QD lasers on CMOS compatible Si are demonstrated. Continuing work towards demonstration of electrically pumped lasers grown on silicon by MOCVD selective area heteroepitaxy is also presented. In this chapter a brief background was given to motivate this work, and a high-level review of PIC technology was presented. In Chapter 2, the technical aspects of photonic integration will be discussed in more detail, covering monolithic integration on III-V substrates as well as III-V/Si integration. Chapter 3 provides a detailed summary of the GaAs PIC platform development and device characterization. The widely tunable lasers that were fabricated on this platform are then discussed in chapter 4. Chapter 5 is an anlaysis of the various wavelength tuning mechanisms in GaAs for tunable lasers. In chapter 6 the growth, fabrication and testing of QD lasers on planar silicon is presented. Chapter 7 covers MOCVD growth by SAH, and presents fabrication details and device results. Chapter 8 provides a summary of the accomplishments and a discussion of future work.

Chapter 2

Review of Photonic Integration Technology

The utility of PICs is greatly increased with an increase in the variety and integration density of components that can be included on-chip. The most fundamental requirement towards realizing complex, system-on-chip functionalities, is the development of a platform that includes both active and passive devices [5]. This chapter provides an overview of the various active-passive integration techniques in use today. The first section focuses on monolithic integration of active and passive devices on native III-V substrates, primarily on InP. The second section reviews the various techniques that are employed to integrate III-V lasers with silicon photonics.

2.1 Monolithic Active-Passive Integration on III-V Substrates

The double heterostructure (DH) forms the backbone of all monolithic III-V PICs [80]. In the epitaxial growth dimension, the only real difference between active and passive devices is the presence of a gain layer in the center of the DH for active devices. Accomplishing active-passive integration is, therefore, primarily a question of how to isolate

gain sections and passive sections while maintaining efficient optical coupling between the two. There are a number of approaches that are commonly used to accomplish this. These are highlighted in Fig. 2.1 and include offset quantum wells (OQW), quantum well intermixing (QWI), and butt-joint regrowth. For the most part these have been demonstrated on InP, however there is no reason that the basic concept cannot be extended to other III-V substrates, such as GaAs.

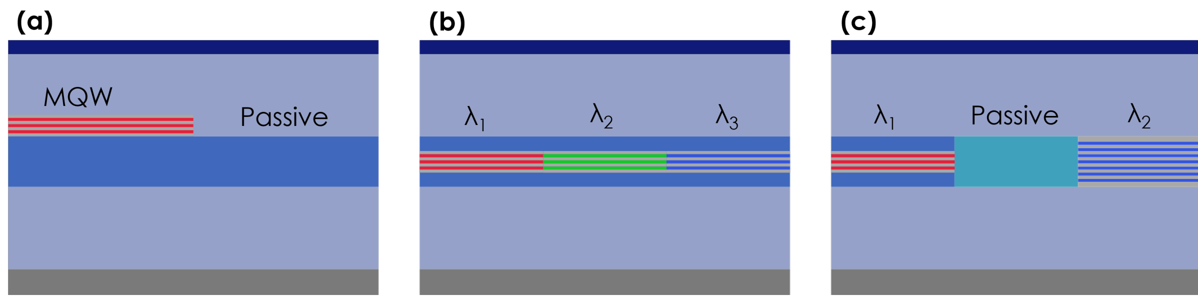

Figure 2.1: Common III-V active-passive integration techniques including (a) offset quantum well (OQW), (b) quantum well intermixing (QWI) and (c) butt-joint regrowth.

The approaches listed in Fig. 2.1 all use at least one, and sometimes multiple, regrowth steps. Other regrowth free methods have been proposed, such as vertical twin waveguide structures [81]. However, these have not been widely adopted by industry, and advances in growth techniques have made the regrowth methods preferable for their performance advantages.

Offset Quantum Wells

The OQW approach, shown in Fig. 2.1(a) places the QW active layers on top of a passive waveguide layer to form the base epi. The QWs are then selectively removed from the passive regions to form "islands" of gain material, which will eventually become lasers or other active components. After selective removal of the QWs, the upper half of the structure, typically p-type cladding and p-contact layer, is regrown across the entire

wafer. By placing the QW in the upper half of the active waveguide (hence the term "offset"), the step height difference between the active and passive regions is minimized, which enables efficient coupling and also makes regrowth simpler. However, offsetting the QWs also moves them away from the peak of the optical mode which reduces QW confinement factor, and therefore modal gain.

Quantum Well Intermixing

In the QWI approach shown in Fig. 2.1(b), ion implantation is used to induce interdiffusion between the QW layers after growth. This process leads to local variation in the composition and thus bandgap of the QWs. By shifting the band edge, the QWs can become transparent to wavelengths that would have previously been absorbed. This enables passive, non-absorbing, waveguide regions to be created without any etching. QWI has several advantages. For example, in the active regions the QWs can be placed in the center of the waveguide, rather than vertically offset, to maximize overlap with the optical mode. Optical coupling between the active and passive waveguides is also improved since there is no step at the interface. By tailoring the implantation process and performing multiple times, multiple bandgaps can be created in different regions which allows for greater wavelength agility and flexibility in component design [47, 82]. QWI still usually involves a regrowth step because the intermixing process is more easily achieved when the QWs are closer to the surface. The starting wafer is typically grown part way into the p-cladding and includes a sacrificial layer which is removed after the intermixing process to prepare the surface for regrowth. The remaining p-cladding and contact layers are then regrown across the whole wafer.

Butt-Joint Regrowth

Butt-joint regrowth, shown in Fig. 2.1(c), is the most commonly used technique in

the industry because it offers the ultimate flexibility in component design and coupling efficiency between sections [49]. This approach employs multiple growth steps. In the first growth, the entire active region epi stack is grown including the upper cladding. Active sections are then masked and selectively removed. In the second growth, the transparent passive waveguide layers are selectively regrown up to the same height as the first growth. The upper cladding in the passive section is not doped, which is an advantage of this approach as it reduces free-carrier absorption loss in the passive waveguides. In the final growth the remainder of the upper cladding and the p-type contact layer are regrown over the entire wafer. In theory there is almost no limit to the number of growths/regrowths that could be performed, which increases the complexity and variety of devices that can be included on a sinlge PIC. Although it is more complex in terms of growth, the advanced growth capabilities available to commercial foundries make butt-joint regrowth the preferred approach due to the flexibility in component design.

2.2 III-V Integration on Silicon

Silicon-based PICs offer numerous advantages, including low-loss and high-performance passive devices, as well as cost-effective, high-volume manufacturing enabled by 300 mm CMOS foundries [54–56]. However, it is well-known that the primary drawback of silicon is its lack of native optical gain. To this end, considerable research has been carried out to combine III-V lasers and gain blocks with silicon photonics [17,20]. This section covers the various techniques that are employed for III-V on Si integration.

2.2.1 Co-Packaging and Hybrid Integration

One approach is to fully fabricate discrete III-V chips and SiPh chips separately and then package them together to couple light from one to the other. This approach is

typically referred to as co-packaging, or hybrid integration (though terminology varies in the literature). This approach allows for flexibility in component design since the chips are fabricated separately, and the coupling is typically accomplished with micro-optics or photonic wirebonding. Fabricating the III-V chips in a dedicated facility also means that device performance is not limited by co-fabrication processes. Additionally, devices can be tested prior to co-packaging to ensure that only fully functional chips are sent for assembly. Co-packaging offers another advantage in terms of thermal isolation. Mounting the gain chip on an aluminum nitride (AlN) submount for example, allows heat to be efficiently removed from the laser during operation.

There are a number of approaches that have been proposed to couple light between lasers and the SiPh waveguides. One technique is to use micro optics such as ball lenses and turning mirrors to direct the laser output to a grating coupler on the surface of the SiPh chip [19]. A schematic of this concept is shown in Fig. 2.2.

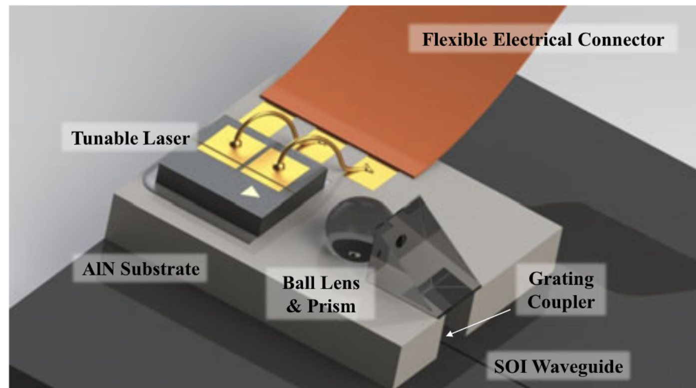

Figure 2.2: Co-packaged micro-optical system with an InP tunable laser coupled to a SiPh chip. Figure adapted from [19].

Another approach is to use 3D photonic wirebonding for coupling [21]. The III-V lasers and SiPh chips are both placed on the same submount and a 3D nanolithography technique is used to create free-form waveguides (known as photonic wirebonds) that connect the laser waveguide directly to the SiPh. The photonic wirebonding process

typically involves depositing a thick photoresist that fully encapsulates the space between facets. 3D wirebonds are then defined in the resist using two-photon lithography, and the unexposed resist is developed away. After developing, the photonic wirebonds are encapsulated in a low index cladding material. Fig. 2.3 shows this type of hybrid assembly as demonstrated in [21], with photonic wirebonds demonstrating insertion loss of around 0.7 dB.

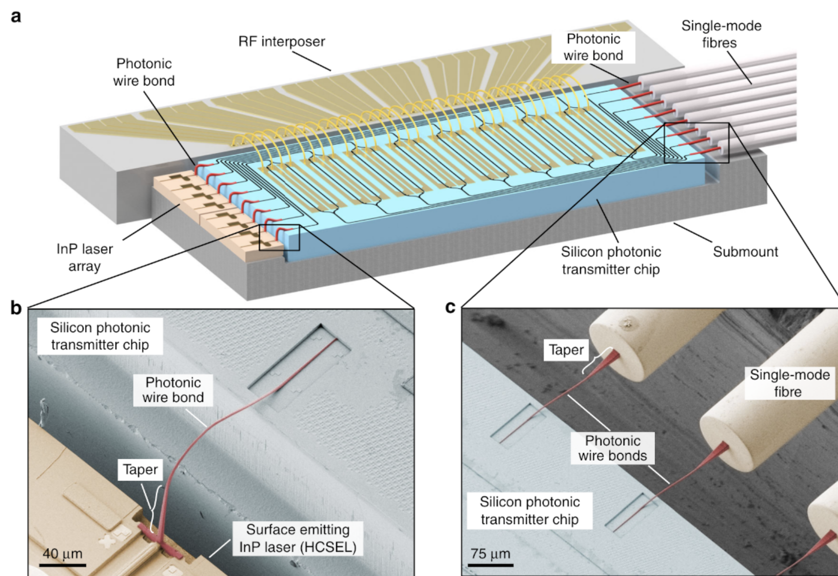

Figure 2.3: Hybrid assembly for co-packaging InP laser array and silicon photonic transmitter using photonic wirebonds. Figure adapted from [21].

Yet another approach is butt coupling. In this approach, an edge emitting III-V reflective SOA (RSOA) chip is placed adjacent to, and as close as possible, to the SiPh chip and the light is coupled directly from one to the other to create a hybrid laser. Fig. 2.4 shows an example of a hybrid laser with a GaSb RSOA edge-coupled to a SiN Vernier mirror chip [83]. While these hybrid and co-packaged devices have demonstrated high performance, the precise alignment requirements and the costs associated with complex packaging make them impractical for scaling to large volume.

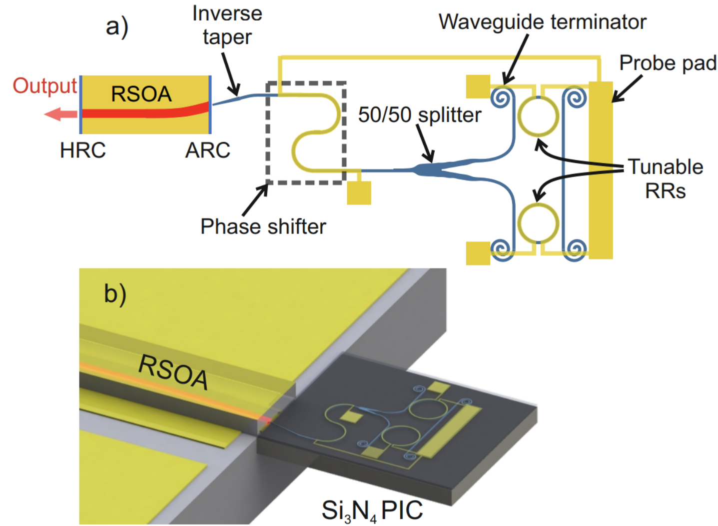

Figure 2.4: GaSb RSOA gain chip edge coupled to SiN PIC to create a hybrid laser. Figure adapted from [83].

2.2.2 Heterogeneous Integration

The heterogeneous integration approach involves bonding of III-V die or whole III-V wafers to silicon at the wafer level. With the micro-transfer printing approach, III-V devices (e.g. lasers or SOAs) are fabricated on their native substrate, encapsulated with a material (typically photoresist) that acts as a tether, and then released from the substrate by etching away a sacrificial layer below the device layer. This leaves the devices attached to the substrate only by the tethers and an elastomer stamp is then used to transfer coupons to a silicon photonics wafer [16]. This process is conceptually similar to flip-chip bonding, but is preferable since the stamp can transfer multiple III-V coupons simultaneously rather than one at a time. This is shown conceptually in Fig. 2.5 [16].

Wafer bonding and co-fabrication is another approach to integrating gain on silicon and is commonly used in the industry [22]. In this approach, entire III-V wafers (usually InP) are bonded epi-side down to an SOI substrate, typically via molecular bonding. The III-V substrate is then removed leaving only the device epi layers on the SOI wafer, and III-V devices are fabricated on the SOI wafer. The III-V laser epi sits on top of the SOI

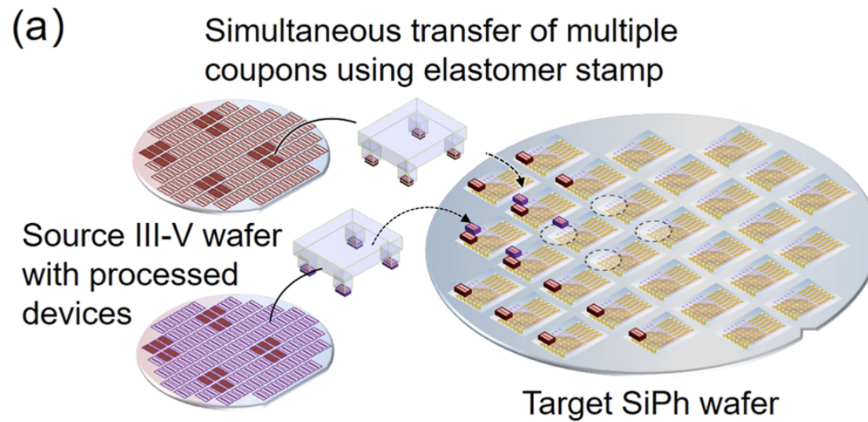

Figure 2.5: Micro-transfer printing of III-V laser coupons on silicon photonics wafer. Figure adapted from [16].

layers, and evanescent coupling is used to couple light from the laser to the underlying silicon waveguide [14, 18]. Fig. 2.6 shows a schematic of this approach, as demonstrated in [14]. Wafer bonding has some distinct advantages compared to micro-transfer printing

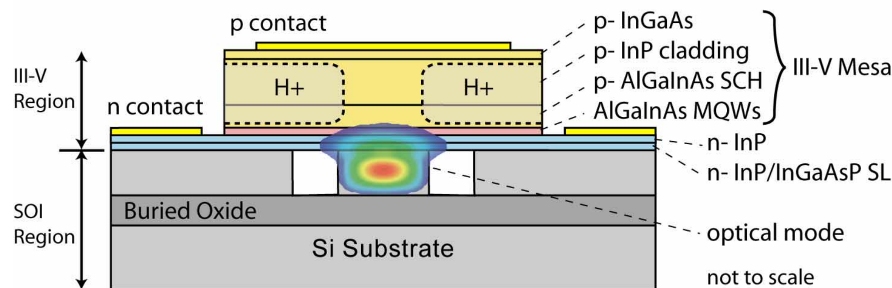

Figure 2.6: Evanescently coupled InP laser on silicon. Figure adapted from [14].

and chiplet bonding. One advantage is that III-V fabrication takes place on a full 300 mm wafer, which makes scaling to large volumes easier and more cost-effective. Another advantage is alignment with the underlying silicon devices. Since the III-V is fabricated directly on the SOI wafer, alignment accuracy is limited only by the tolerances of the lithography tools, which are typically better than the accuracy of micro-transfer printing tools.

2.2.3 Monolithic Integration

Growing III-V gain material directly on silicon is an active area of research, and has the potential to offer many advantages compared to heterogeneous integration, if the quality of the III-V crystal is sufficiently high. In this approach, III-V epitaxy is grown directly on a silicon substrate, thus eliminating many of the extra costs associated with packaging and bonding used in other integration methods. However, the inherent dissimilarities between the two materials present several challenges to achieving high quality epitaxial layers. As a result, semiconductor lasers grown on silicon generally underperform in comparison to those grown on native substrates. One major issue is the difference in lattice constant between silicon and most III-V. Another issue arises from the fact that silicon is a non-polar material, whereas III-Vs are polar. The mismatch in polarity leads to the formation of antiphase boundaries (APBs). Finally, there is a significant difference in the coefficient of thermal expansion for silicon and III-V materials. The different expansion rate leads to the formation of cracks in the III-V epitaxy as the wafer cools down after growth. There are various approaches that are used to deal with these issues and achieve low defect density material.

Lattice Mismatch and Threading Dislocations

For silicon, the lattice constant is approximately 5.431 Å, whereas for GaAs it is 5.653 Å and for InP 5.869 Å. This corresponds to a mismatch of 4.09% for GaAs and 8.06% for InP [48]. During growth, a significant amount of strain builds up and the III-V material will begin to relax when it reaches a certain critical thickness. This relaxation creates misfit dislocations where there are missing, or dangling, bonds in the crystal structure. Misfit dislocations generally lead to threading dislocations (TDs) which tend to propagate vertically through the epitaxial layers before terminating on the surface.

When a threading dislocation ends up in the active region it leads to a trap states, which dramatically reduces the chances for radiative recombination, leading to degraded device performance.

One technique for reducing TDs is thermal cycle annealing (TCA). This involves heating and cooling the wafer multiple times during growth. When the sample is heated, atoms become more mobile and the dislocations tend to coalesce, and promote the annihilation of TDs. Strained layer superlattices (SLS) can also be used as dislocation filters to reduce the total dislocation density. These filters typically consistent of alternating layers of strained InGaAs on GaAs, which promote propagation of TDs in the lateral direction, rather than vertically, effectively reducing the defect density in the epitaxial layers above. Typically multiple SLS layers are embedded in a thick GaAs buffer and combined with TCA to achieve the lowest density of TDs [84–86].

Anti-Phase Boundaries

APBs occur as result of the polarity mismatch between III-V materials and silicon. The surface of on-axis silicon is comprised of single atomic steps. For III-Vs these would be double atomic steps to accomodate the group III and group V species. When growing on silicon, the group V species preferentially nucleate on the surface and the presence of single-atomic steps can result in V-V bonds at the step edges leading to APBs. The oldest approach to deal with this problem was to grow on miscut silicon which creates double-atomic steps on the surface. However, this is undesirable as miscut silicon is incompatible with the CMOS process, thus eliminating one of the main advantages of growing on silicon. A better approach is to pattern nano V-grooves on the silicon surface, as shown in Fig. 2.7 [85, 87]. This creates the necessary double atomic steps in the V-groove trench, while still using a CMOS-compatible substrate. Gallium phosphide (GaP) on silicon can also be used to eliminate APBs [88–91]. In this approach, GaP

is grown directly on the unpatterned silicon surface and the double atomic step is then formed on the GaP surface through a high-temperature surface passivation step. Devices demonstrated later in this thesis are grown on both V-groove Si templates, and GaP on Si templates.

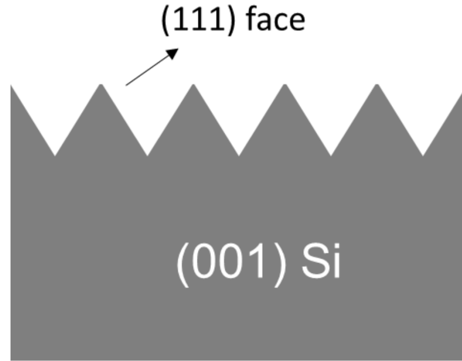

Figure 2.7: V-Groove patterned (001) Si to expose the (111) face in preparation for III-V heteroepitaxial growth.

Coefficient of Thermal Expansion Mismatch

The primary problem caused by the difference in the coefficient of thermal expansion (CTE) is cracking on the surface of the III-V epitaxy. CTE for GaAs is approximately 5.73E-6 K^{-1} and for Si is about 2.6E-6 K^{-1}. This represents a mismatch of over 100 %, or in other words, GaAs expands at more than twice the rate of Si. The temperature is quite high during GaAs growth (greater than 500 °C) and when the sample is cooled to room temperature after growth, the GaAs contracts significantly more than the Si leading to cracking [92]. Fig. 2.8 shows an example of thermal cracks on a GaAs surface after growth on silicon.

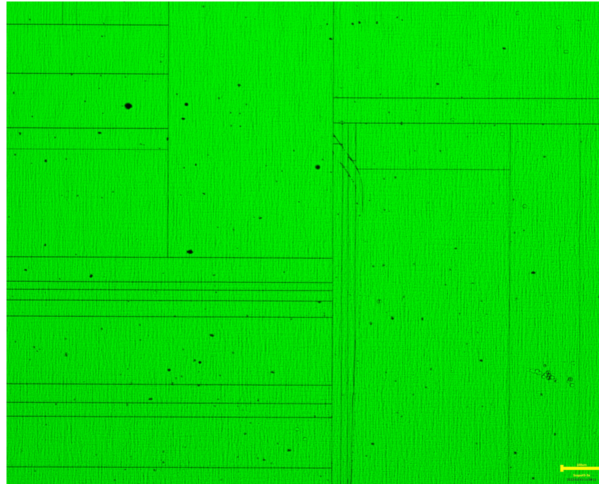

Figure 2.8: Example of cracking on GaAs surface due to thermal expansion mismatch between GaAs and the underlying Si substrate.

Lasers on Silicon and the Problem of Coupling

By utilizing the techniques discussed above, multiple demonstrations of lasers grown on Si have been reported. Fig. 2.9 shows two examples of lasers grown on Si. Fig. 2.9(a) [84] is a 1550 nm QW laser grown entirely by MOCVD on CMOS-compatible (001) Si. This example uses a GaAs buffer grown on nano V-groove patterned Si, followed by growth of the InP-based laser epitaxy. Continuous wave (CW) lasing was demonstrated at room temperature. Fig. 2.9(b) [58] is a QD laser with emission near 1.3 µm. The QD laser epitaxy was grown by MBE, but the underlying buffer was grown by MOCVD, again on CMOS compatible Si, but in this case unpatterned. These lasers demonstrated room temperature, CW lasing with threshold current density as low as 34.6 A/cm^2 per QD layer, and operation up to 80 °C. Both of the examples mentioned here, as well as many others, require the use of a thick buffer layer between the silicon and the III-V to trap defects and allow for growth of high quality laser epi. The presence of this buffer appears to be unavoidable. In terms of integration this presents a major challenge because the laser is separated from the underlying Si by several microns of highly defective material.

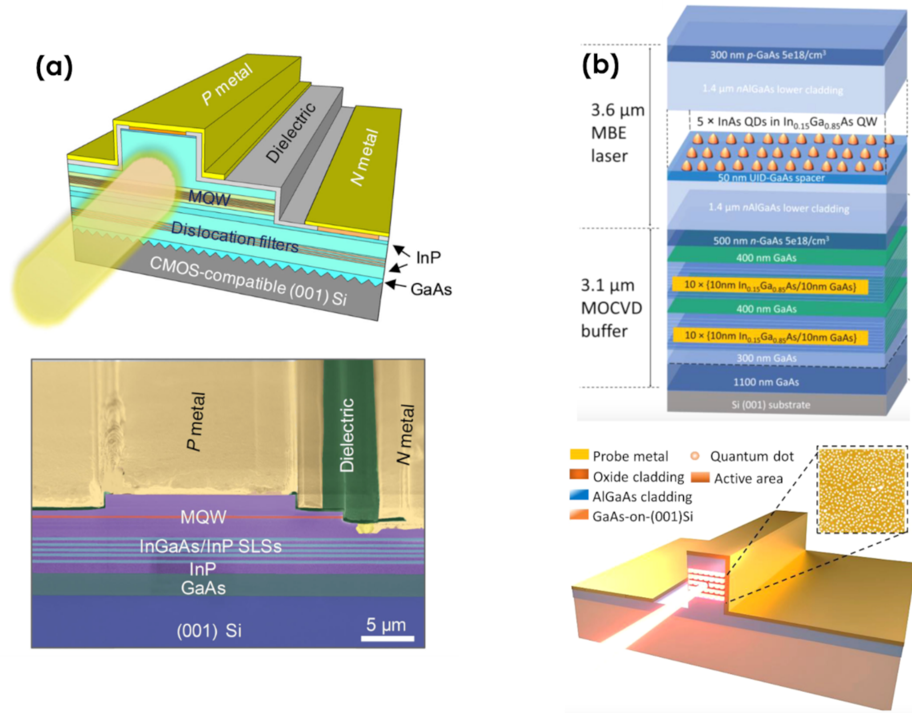

Figure 2.9: Examples of lasers monolithically grown on silicon. (a) MOCVD grown 1550 nm QW laser [84] and (b) MBE grown QD laser on MOCVD grown buffer [58].

This makes coupling from the III-V laser to the underlying Si impractical, if the laser is grown on a planar substrate. One solution that is being actively pursued is to start with a SOI template and etch deep recesses, or trenches, through the oxide and into the Si substrate below. Lasers can then be grown inside the recess, which places the buffer layer well below the device layers, and the III-V laser can be aligned with Si or SiN waveguides in the SOI. Another advantage of this approach is that the difference in CTE becomes less relevant because the smaller surface area is less prone to cracking during cool down. Early demonstrations have been reported with electrically pumped MBE QD lasers grown in trenches over an MOCVD grown GaP-on-Si buffer [93, 94]. These results are quite promising in terms of demonstrating direct coupling from a III-V laser on Si to SiPh for a monolithic SiPh platform.

As mentioned earlier, MOCVD has some advantages over MBE due to the higher growth rate which make it preferrable for high-volume production. Since the buffers are already grown by MOCVD, it would also be advantageous to use the same growth technique for the laser epi. Another advantage of MOCVD is the ability to perform selective area growth. In the MBE demonstration, III-V material is deposited across the entire wafer and becomes polycrystalline in the areas outside the trenches. This excess material must be removed with a time-consuming chemi-mechanical polishing (CMP) process post-growth. MOCVD on the other hand, grows material selectively in the recess, leaving the oxide field area relatively clean. Some III-V particles do tend to form on the oxide surface, however these are quickly removed with a wet etch after growth. The selective growth of MOCVD also enables the crystalline III-V material to grow all the way to the edge of the oxide trench without an air gap or polycrystalline material at the edges. This is advantageous for coupling since the gap between the clean III-V waveguide and SiPh waveguides is minimized. Optically pumped lasers grown by MOCVD selective area heteroepitaxy (SAH) on Si have been demonstrated [60, 61]. In the latter portion of this thesis, efforts to demonstrate electrically pumped lasers on Si by MOCVD SAH are presented. Some of the specific challenges and progress towards this goal will be discussed in later chapters.

2.3 Summary

The preceding two chapters provided an overview of common III-V and Si based PIC platforms. InP and SiPh are the most mature in terms of photonic integration, whereas GaAs has traditionally been used for discrete devices. Table 2.1 below summarizes some of the relevant properties for the PIC materials discussed earlier - specifically, GaAs, InP, Si and SiN. Note that Si and SiN waveguides are often included together on the same

wafer [54] but they are separated in this table to highlight the differences. Also note that the wavelength range listed for GaAs and InP is the range over which emission is feasible; the transparency region for both materials extends to longer wavelengths and well into the mid-IR.

Table 2.1: Comparison of PIC Material Platforms

	GaAs	**InP**	**Si**	**SiN**
Wavelength Range (µm)	0.8-1.3	1.1-2.0	> 1.1	> 0.4
Native Light Emission?	Yes	Yes	No	No
Laser Wall-Plug Efficiency	> 70% [66]	< 50% [63, 95]	< 20% [58]	< 20%
Power	> 10 W [64–66]	> 1 W [63]	< 100 mW [58]	> 10 mW [42, 96]
Waveguide Loss	<1dB/cm (passive) [97]. >1dB/cm (active) [35]	<1dB/cm (passive), >1dB/cm (active) [49]	<1dB/cm [51]	<0.1dB/cm [52, 53]
Integration Techniques	Monolithic	Monolithic	Hybrid, Heterogeneous.	Hybrid, Heterogeneous
Wafer Size	6-8”	2-4”	8-12”	8-12”
CMOS Compatibility?	No	No	Yes	Yes

Chapter 3

Active-Passive Integration on Gallium Arsenide

In this chapter the development of an active-passive PIC platform on GaAs is discussed. The motivation for this work was to develop a tunable laser PIC with an operating wavelength at 1030 nm for Lidar, specifically for airborne and space applications where deployment on small platforms is highly desirable. Wavelengths near 1 µm are common for topographical Lidar systems owing to the relatively low atmospheric absorption and the existence of high-quality detectors, such as silicon or indium gallium arsenide (InGaAs) avalanche photodiodes (APDs), in this spectral range [36, 98]. CSWaP is of critical importance for any airborne or space-based system. Extending PIC technology to the 1 µm range would allow for multiple optical components to be integrated onto a single compact platform similar to what has been demonstrated on InP for CO_2 gas sensing Lidar [32].

3.1 Active-Passive Epitaxy Design

The active-passive PIC platform on GaAs uses an etch and regrowth process where the multi-QW (MQW) active layers are selectively removed from the passive regions to create isolated gain sections, and the upper cladding and p-contact are then formed in a

subsequent regrowth step. This is the offset QW (OQW) technique described in chapter 2. Table 3.1 shows the details of the epitaxy, with the layers formed during the regrowth step indicated, as well as the layers that were selectively removed to create passive regions. Strained $In_xGa_{1-x}As$ QWs are commonly used for wavelengths between 0.88 µm and 1.1

Table 3.1: Epitaxial Layers for Active-Passive Integration

	Material	**Thickness (nm)**	**Doping (cm^{-3})**
Regrowth Layers	GaAs	200	(p) 5e19
	$Al_{0.4}GaAs$	800	(p) 7e17
	$Al_{0.4}GaAs$	200	(p) 5e17
	$Al_{0.4}GaAs$	300	(p) 2e17→5e17
	$Al_{0.2}GaAs$	50	(p) 2e17
Selectively removed in passive regions	GaAs	20	(p) 1e17
	GaAs	20	UID
	$GaAsP_{0.1}$	8	UID
	$In_{0.271}GaAs$	5	UID
	$GaAsP_{0.1}$	8	UID
	$In_{0.271}GaAs$	5	UID
	$GaAsP_{0.1}$	8	UID
	$In_{0.271}GaAs$	5	UID
	$GaAsP_{0.1}$	8	UID
Base Structure	GaAs	90	UID
	$Al_{0.2}GaAs$	100	(n) 1e17
	$Al_{0.75}GaAs$	1600	(n) 1e18
	GaAs	500	(n) 1e18
	GaAs	625 ± 20 µm	(n) 2-5e18

µm [40]. However, the high indium (In) content required to reach wavelengths longer than 1 µm introduces significant strain that can potentially be detrimental. To maintain an acceptable cumulative strain in the MQW layers, this design uses 5 nm $In_xGa_{1-x}As$ QWs with x=0.271, and 8 nm gallium arsenide phosphide ($Ga_{1-x}AsP_x$) barriers with x=0.1 (instead of GaAs barriers) to provide strain compensation. The MQW active region is surrounded by GaAs separate confinement heterostructure (SCH) layers, and AlGaAs is used for both the upper and lower cladding layers. Prior to fabrication and

regrowth, the photoluminescence (PL) spectrum of the wafer was measured and is shown in Fig. 3.1 with peak PL emission from the QWs at 1027 nm. The smaller peak near 870 nm is emission from the GaAs substrate.

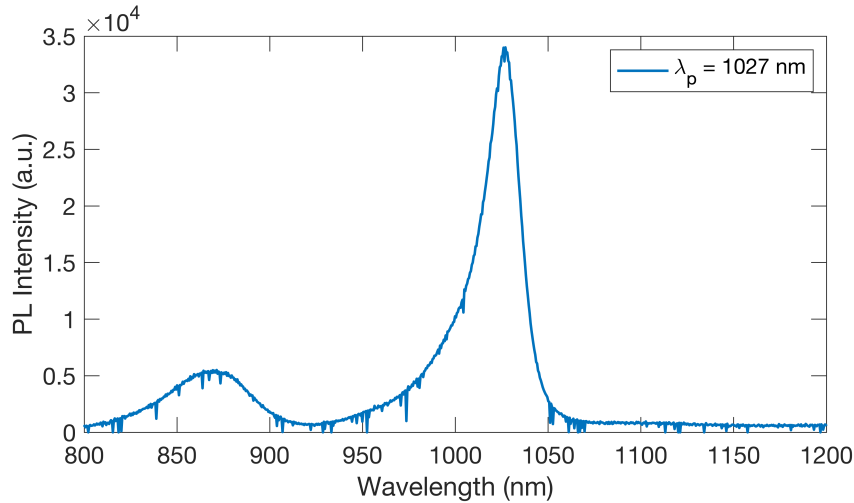

Figure 3.1: Photoluminescence spectrum of epitaxial material prior to fabrication and regrowth

This PIC platform was designed to enable efficient coupling of light between the active and passive sections, with minimal scattering and back reflection. A 3 µm wide rib waveguide structure with 1.35 µm etch depth was simulated using Ansys Lumerical. The fundamental TE mode profiles in the active and passive sections are shown in Fig. 3.2. A simple overlap integral between the modes indicates that 96% of the optical power should be coupled between active and passive waveguide sections.

To maximize optical coupling between active and passive regions, the QWs are placed near the top of the waveguiding layer stack to minimize the height of the step at the active-passive transition, to create an OQW structure. However, this comes with a tradeoff, as the QW confinement factor, Γ_{QW}, is reduced as the QWs are moved further from the center of the waveguide. The design presented in Table 3.1 vertically places the QWs in the upper half of the active region, with thinner GaAs and AlGaAs SCH layers above, to reduce the step at the interface while still achieving an overall confinement factor Γ_{QW}

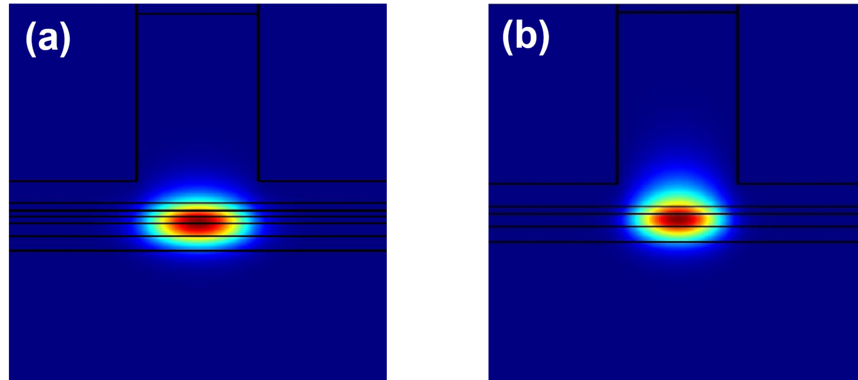

Figure 3.2: Fundamental TE mode in (a) active and (b) passive sections for a 3 µm wide rib waveguide.

of 5.02% for all three QWs. The 1.35 µm depth was determined using simulations to optimize QW overlap, active-passive coupling, and eliminate some of the higher order transverse modes. This rib waveguide structure also mitigates scattering loss due to surface roughness by burying the mode below the etched ridge, and reduces surface recombination by not exposing the active layers to air.

3.2 Device Fabrication

The epitaxy described in the previous section was used to fabricate Fabry-Perot (FP) lasers. The mask layout used for this fabrication includes lasers with various waveguide widths from 2 µm up to 20 µm broad area lasers and has both active and passive waveguide sections to demonstrate active-passive coupling. Fig. 3.3 shows a schematic diagram illustrating the primary fabrication process steps for the rib waveguide structure. The active QW material is first selectively removed to form passive regions, using inductively coupled plasma reactive ion etching (ICP-RIE) with chlorine (Cl_2) and nitrogen (N_2) gas chemistry. The upper cladding and p-contact layers are then regrown by MOCVD. Following regrowth, the rib waveguides were etched also using a Cl_2/N_2 ICP-RIE process.

The etch depth for this step was 1.35 µm, stopping in the upper p-cladding to form the structure illustrated in Fig. 3.3(d). The sample surface was passivated by depositing 100 nm of silicon nitride (SiN) followed by 300 nm of silicon dioxide (SiO_2). This was followed by etching through the dielectric layers on top of the ridge to form vias to the GaAs p-contact layer. Ti/Pt/Au (10/40/1000 nm) was used to form the top side p-contacts. The GaAs substrate was then thinned to approximately 150 µm before depositing Ti/Pt/Au (20/40/500nm) for the backside n-contact metal.

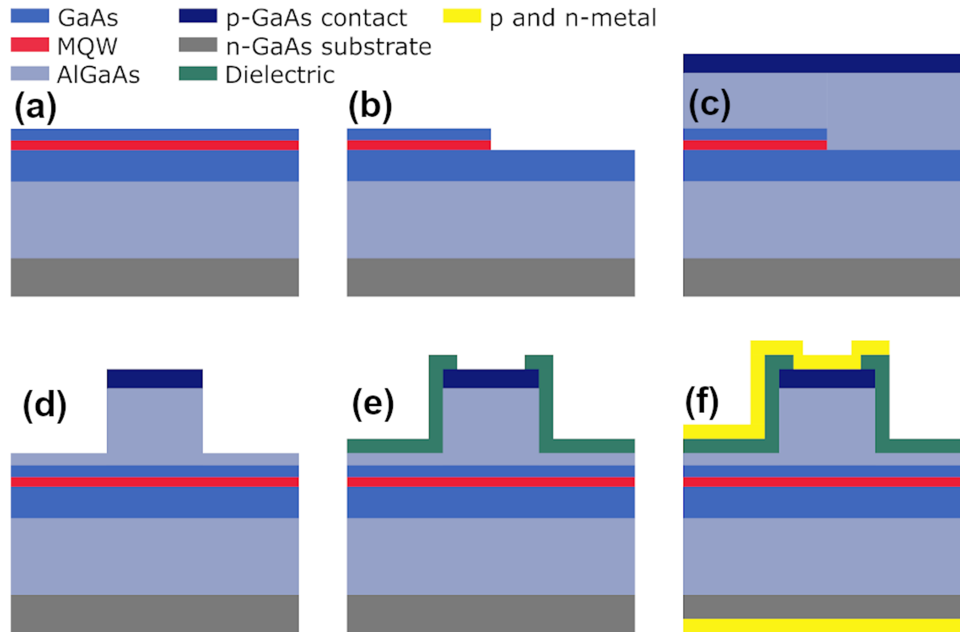

Figure 3.3: Summary of primary fabrication steps including (a) initial epitaxial layers, (b) active-passive etch, (c) upper cladding and p-contact layer regrowth, (d) ridge waveguide etch, (e) surface passivation and p-contact via opening, (f) p-metal and n-metal contact formation.

Fig. 3.4(a) is a scanning electron microscope (SEM) image of the active-passive etch prior to regrowth (corresponding to Fig. 3.3(b)), showing a step height of just under 100 nm. The target etch depth was 87 nm to completely remove the active layers in Table 3.1. Fig. 3.4(b) shows a tilted SEM image of a cleaved facet on one of the completed devices, and Fig. 3.4(c) is a top view microscope image showing a fully fabricated active

FP laser and active-passive FP laser.

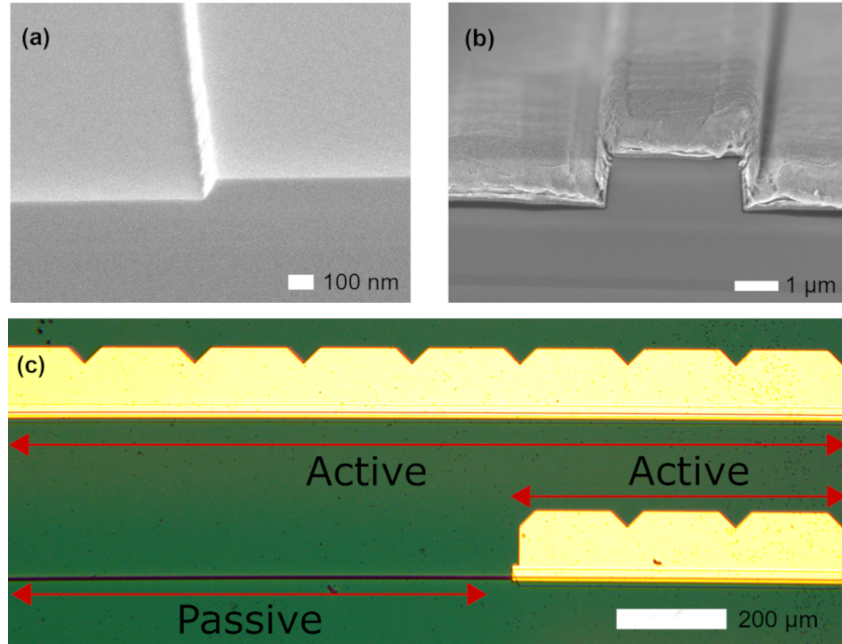

Figure 3.4: SEM image of (a) etched active-passive transition prior to regrowth, (b) active side cleaved facet of 3 μm wide fabricated laser, and (c) top view microscope image of completed devices, showing an all-active FP laser and an active-passive FP laser. The notches in the metal are spaced 200 μm apart and were placed as a visual aid for cleaving.

3.3 Device Testing and Characterization

3.3.1 Light-Current-Voltage Measurements

A significant amount of information relating to material properties and device performance can be gleaned from simple light-current-voltatge (LIV) measurements on FP lasers of varying length. From a single LI curve the threshold current I_{th}, and differential quantum efficiency η_d can be obtained, where η_d is defined as [80],

$$\eta_d = \left[\frac{q}{h\nu}\right]\frac{dP_0}{dI}. \qquad (I > I_{th}) \tag{3.1}$$

q is the fundamental electron charge, h is Planck's constant, and ν is the optical frequency. Note that the value for η_d obtained from a single LI curve is only for the side where the light was measured. The total differential efficiency must account for light output from both facets (in the case of cleaved facet FP lasers, the two sides should be identical and one can simply double η_d measured from a single side).

After fabrication, laser bars of varying length were cleaved from the sample to form facets and facilitate characterization. LI and LIV characteristics were measured for the devices under both CW and pulsed current operation using 500 ns pulse widths with 0.5% duty cycle. Fig. 3.5(a) shows a typical LIV characteristic measured from one side of a 20 µm wide, 800 µm long cleaved facet broad area laser under CW operation. The broad area laser in Fig. 3.5(a) has a total differential efficiency from both sides of 57.8%, and threshold current of 35.2 mA, with single sided output power of 120 mW (240 mW total). Additional measurements on a 20 µm wide laser with a 2 mm long cavity exhibited threshold current density as low as 94 A/cm^2. Similarly, Fig. 3.5(b) shows single-side LI curves for five different 600 µm long FP lasers with widths from 2 µm to 5 µm. These lasers all exhibit threshold current below 12.6 mA with the lowest threshold being 9 mA for the 2.5 µm wide laser. Additionally, the 3 µm, 4 µm, and 5 µm wide devices output greater than 25 mW of optical power from each facet at 100 mA CW current. The differential efficiencies from both facets are approximately 55% for all three of these laser geometries.

Fig. 3.6(a) shows LI characteristics for active-passive FP lasers with various waveguide widths, all with a 400 µm long gain section coupled to a 400 µm long passive section as shown in the schematic in Fig. 3.6(b), and the device image of Fig. 3.4(c). The optical power from both the active and passive side facets was measured as reported in Fig. 3.6(a). The slightly lower power from the active side is to be expected as the active layers create a more reflective cleaved facet mirror due to the slightly higher effective

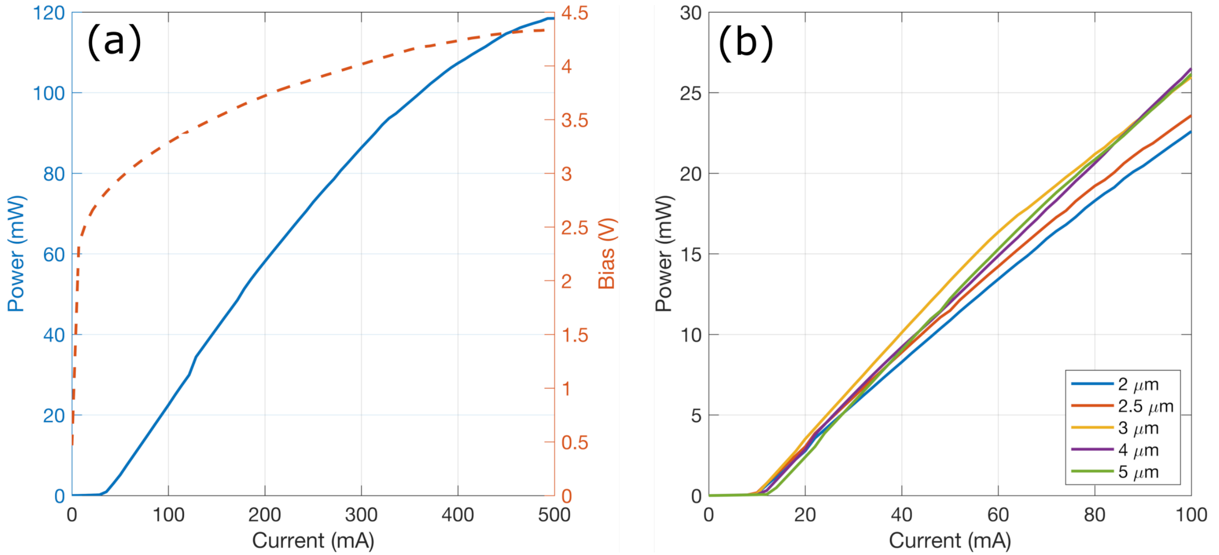

Figure 3.5: Light-current characteristics for (a) 20 μm wide by 800 μm long broad area laser and (b) 600 μm long lasers between 2 μm and 5 μm wide under CW current injection.

index in this section, and it is the facet reflectivity that determines the fractional power out of each end [80]. The active-passive devices demonstrate comparable performance in terms of power output, differential efficiency, and threshold current, to the all-active lasers shown in Fig. 3.5. All five of the active-passive lasers measured here exhibit threshold currents below 10.7 mA and as low as 7 mA for the 2 μm wide laser. The total output power from both sides was measured to be greater than 50 mW for all devices and as high as 62 mW for the 5 μm wide laser at 100 mA CW current.

3.3.2 Extracting Loss and Efficiency

The internal loss $\langle\alpha_i\rangle$ and injection efficiency η_i are related to differential efficiency η_d by the following equation [80],

$$\frac{1}{\eta_d} = \frac{\langle\alpha_i\rangle}{\eta_i ln(1/R)} L + \frac{1}{\eta_i} \tag{3.2}$$

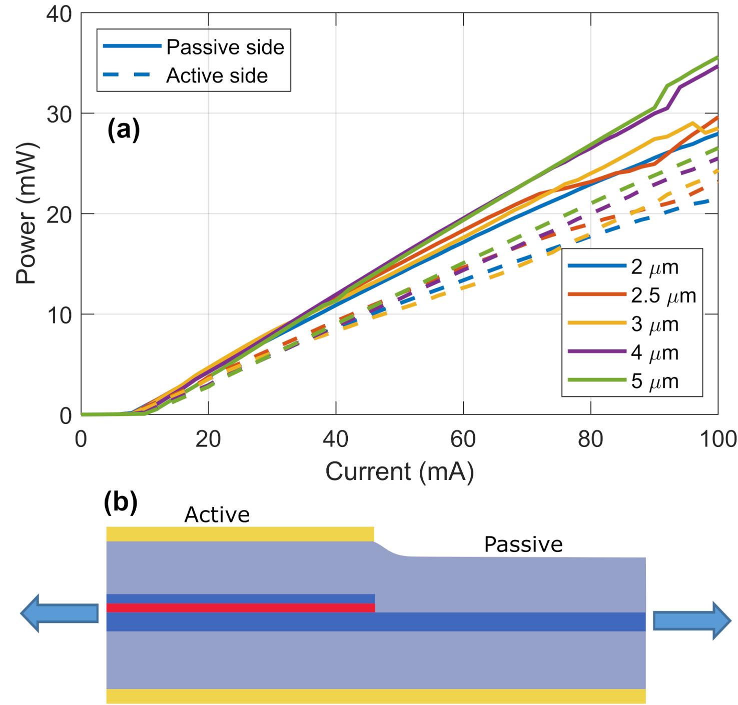

Figure 3.6: (a) LI characteristics for active-passive lasers with 400 μm long active section and 400 μm long passive section. (b) Side-view schematic diagram of a generic active-passive laser cavity.

where R is the mean mirror reflectivity and L is the cavity length. Determining $\langle \alpha_i \rangle$ and η_i from (3.2) requires the use of at least two lasers of different length that are otherwise identical. Accurate values can be obtained by plotting $1/\eta_d$ versus length for multiple devices, and using a linear fit to extract the slope and y-intercept. In this case, a cutback measurement was performed where a single device was cleaved and tested, and then cleaved to a shorter length and tested again, repeating until the laser bar was too short to be cleaved further ($\sim$250 μm). Broad area lasers typically give more accurate values for $\langle \alpha_i \rangle$ and η_i, since lateral current spreading and carrier leakage can be neglected, and some of the excess losses associated with surface recombination and scattering due to sidewall roughness are minimized. Additionally, to reduce the effects of self-heating in the device, these measurements were performed under pulsed current operation with

the stage temperature set to 20° C. Results are shown in Fig. 3.7 which plots inverse differential efficiency versus cavity length for a 20 µm wide laser, with lengths varying from 2800 µm down to 250 µm. Using eq. (3.2) and a linear fit to the data a value of 3.44 cm^{-1} was obtained for $\langle\alpha_i\rangle$ with $\eta_i = 0.988$.

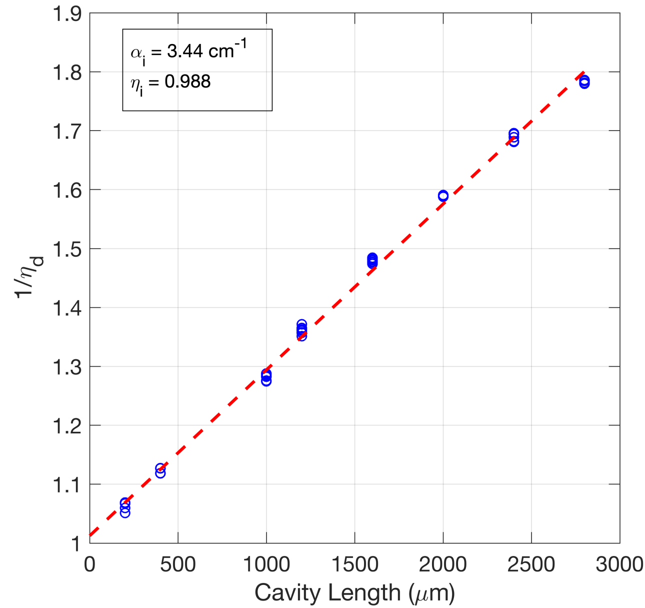

Figure 3.7: Inverse differential efficiency as a function of cavity length for 20 µm wide broad area lasers under pulsed current operation and linear fit to extract loss and efficiency.

The loss value obtained from the analysis in Fig. 3.7 is only the internal loss in the active section. Additional measurements are required to obtain the passive waveguide loss. This can similarly be obtained from LI measurements on lasers with both active and passive waveguide sections, however the analysis is somewhat more complex. For such a device, the total differential efficiency considering both sides is [80],

$$\eta_d = \eta_i \eta_{da} \eta_{dp}, \tag{3.3}$$

where,

$$\eta_{da} = \frac{ln\sqrt{1/R_1R_2}}{\langle\alpha_{ia}\rangle L_a + ln\sqrt{1/R_1R_2}} \tag{3.4}$$

and,

$$\eta_{dp} = \frac{(1-R_1)/\sqrt{R_1} + (1-R_3)/\sqrt{R_3}}{(1-R_1)/\sqrt{R_1} + (1-R_3e^{-2\alpha_{ip}L_p})/\sqrt{R_3}e^{-\alpha_{ip}L_p}} \tag{3.5}$$

and R_1 is the reflection coefficient at the active-air interface, R_2 is the reflection coefficient at the active-passive interface, R_3 is the reflection coefficient at the passive-air interface, L_a is the gain section length, L_p is the passive section length, $\langle\alpha_{ia}\rangle$ is the internal loss in the active region (3.44 cm^{-1} from Fig. 3.7) and α_{ip} is the internal loss in the passive waveguide section. For the purpose of calculations, R_1, R_2, and R_3 were obtained from simulations as, 0.290, 6.86e-5, and 0.284, respectively. Equation (3.3) is plotted as a function of length to visualize the change in η_d with increasing passive loss and is shown in Fig. 3.8(a). The simulated curves in Fig. 3.8(a) use a 400 µm long gain section and the previously calculated values for α_{ia} and η_i.

LI measurements were performed under pulsed current operation for 3 µm wide active-passive FP lasers with a 400 µm long active section length and a passive section that was incrementally cleaved back from 2800 µm to 600 µm. Power output was measured from both sides at each length to obtain the total η_d for each laser, and these data points are plotted versus passive section length in Fig. 3.8(b). Combining equations (3.4) and (3.5) with equation (3.3) and using the previously obtained values for $\langle\alpha_{ia}\rangle$ and η_i in the active region, α_{ip} is the only remaining unknown quantity and therefore can be extracted. To obtain an accurate value a fit to equation (3.3) was applied to the experimental data points shown in Fig. 3.8(b). The extracted internal passive loss is 4.05 cm^{-1}. It is worth noting that the passive waveguide loss is higher than in the active waveguide. However, the epitaxial layer structure was originally designed with a higher Al content p-cladding but 40% Al was used due to concerns with higher Al content regrowth. The lower Al

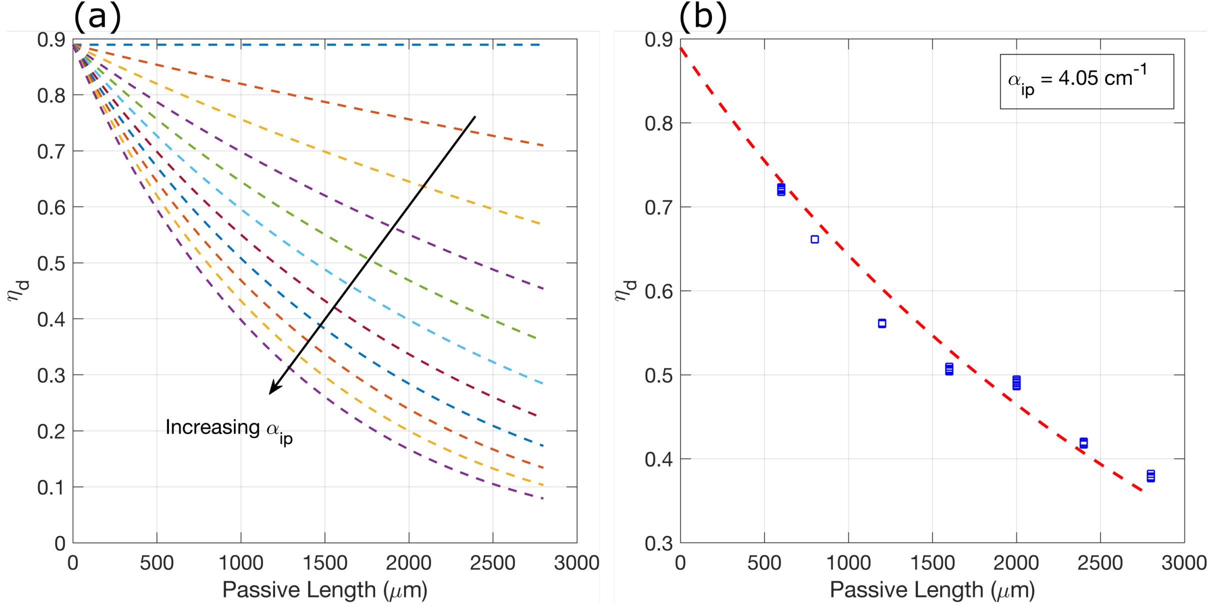

Figure 3.8: (a) Simulated η_d as a function of passive section length for varying passive loss from 0 cm^{-1} to 10 cm^{-1} in 3 µm wide active-passive FP lasers with 400 µm long gain sections. (b) Measured η_d points with curve fit to extract $\alpha_{ip} = 4.05$ cm^{-1}.

content leads to higher refractive index (3.236 at 1030 nm for $Al_{0.4}GaAs$), and therefore lower index contrast between the core and cladding. This in turn reduces the mode confinement leading to greater overlap with the p-doped cladding, which increases loss from free-carrier absorption. In future designs, this issue could be mitigated either by increasing Al content in the upper cladding, or by increasing the thickness of the GaAs waveguiding layer.

3.3.3 Gain Characteristics

Threshold modal gain for an in-plane laser is given by,

$$\Gamma g_{th} = \langle \alpha_i \rangle + \frac{1}{L} ln \left(\frac{1}{R} \right). \tag{3.6}$$

If internal loss, $\langle\alpha_i\rangle$, and QW confinement factor, Γ_{QW}, are known then threshold gain versus cavity length can be calcluated easily from (3.6). From the same set of measurements used to generate Fig. 3.7, the threshold current, I_{th} was obtained for each length, and this can be converted to threshold current density since η_i is already known using,

$$J_{th} = \frac{\eta_i I_{th}}{wL} \tag{3.7}$$

where w is the width of the active region.

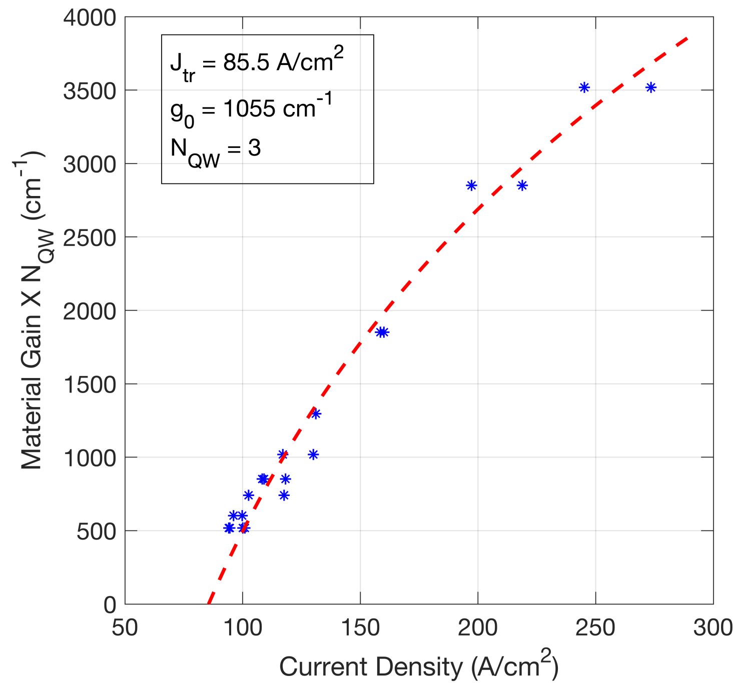

Figure 3.9: Material gain as a function of current density for three 5 nm $In_xGa_{1-x}As$ (x=0.271) QWs with 8 nm $Ga_{1-x}AsP_x$ (x=0.1) barriers, obtained from 20 µm wide lasers measured under pulsed current operation.

With threshold gain and current density known at multiple device lengths, a gain versus current density characteristic can be constructed. This data can typically be fitted to a two parameter exponential curve given by,

$$J = J_{tr} e^{\frac{g}{g_0}} \tag{3.8}$$

where J_{tr} is the transparency current density and g_0 is a fitting parameter. The experimental data points are shown in Fig. 3.9, using the simulated value $\Gamma_{QW} = 5.02\%$ to calculate threshold material gain from eq. (3.6). This was then fitted to eq. (3.8) to extract $J_{tr} = 85.5\ A/cm^2$ and $g_0 = 1055\ cm^{-1}$.

3.3.4 Temperature Characteristics

An increase in temperature has a deleterious effect on the performance of semiconductor lasers. This is usually observed as an increase in threshold current, and decrease in differential efficiency, both of which have an exponential dependence on temperature. The relative changes in I_{th} and η_d at different temperatures can be directly measured and used to extract characteristic temperatures with the following relationships:

$$\frac{I_{th1}}{I_{th2}} = e^{(T_1 - T_2)/T_0} \tag{3.9}$$

$$\frac{\eta_{d1}}{\eta_{d2}} = e^{-(T_1 - T_2)/T_\eta} \tag{3.10}$$

where the subscripts 1 and 2 for I_{th} and η_d correspond to the temperatures T_1 and T_2, respectively.

LI curves were obtained, using pulsed-current to mitigate self-heating, on a 20 µm wide, 400 µm long laser. The temperature of the stage used to mount the laser was varied from 20 °C to 70 °C. Threshold current and differential efficiency were measured at each temperature and these data points are plotted in Fig. 3.10. Using eqs. (3.9) and (3.10), the characteristic temperatures were extracted resulting in $T_0 = 205\ K$ and $T_\eta = 577\ K$, which are consistent with typical values for this material system [80].

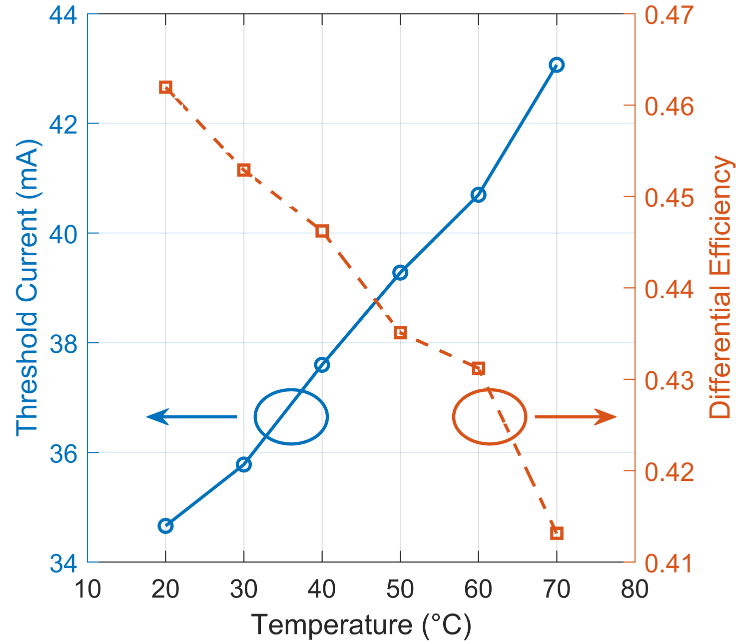

Figure 3.10: Threshold current and single-sided differential efficiency as a function of temperature for a 20 µm wide, 400 µm long broad area laser. Measurements were performed with pulsed current to mitigate self-heating, while the stage temperature was varied from 20 °C to 70 °C.

3.3.5 Lasing Spectra

The light output from a 3 µm wide active-passive laser with 400 µm long active and passive sections (800 µm total length) was coupled to a lensed optical fiber and the lasing spectrum at varying levels of current injection was recorded with an optical spectrum analyzer (OSA). These spectra are shown in Fig. 3.11. The spectrum is red-shifted compared to the PL emission, showing a lasing peak near 1045 nm just above threshold (10 mA current), compared to the PL emission wavelength of 1027 nm. This is expected as self-heating causes the laser output to shift to longer wavelengths under CW current injection. It should also be noted that this waveguide is not single mode in the transverse direction, as evidenced by the two distinct peaks in the lasing spectrum particularly at higher current injection levels. This multi-mode behavior was expected based on simulations, which showed that the 3 µm wide waveguide supports the horizontal

TE1 mode in addition to the fundamental TE00 mode. However, this is not a concern since future applications planned for this platform will include grating mirrors to provide mode filtering. Fig. 3.12 shows the temperature dependence of lasing wavelength. The

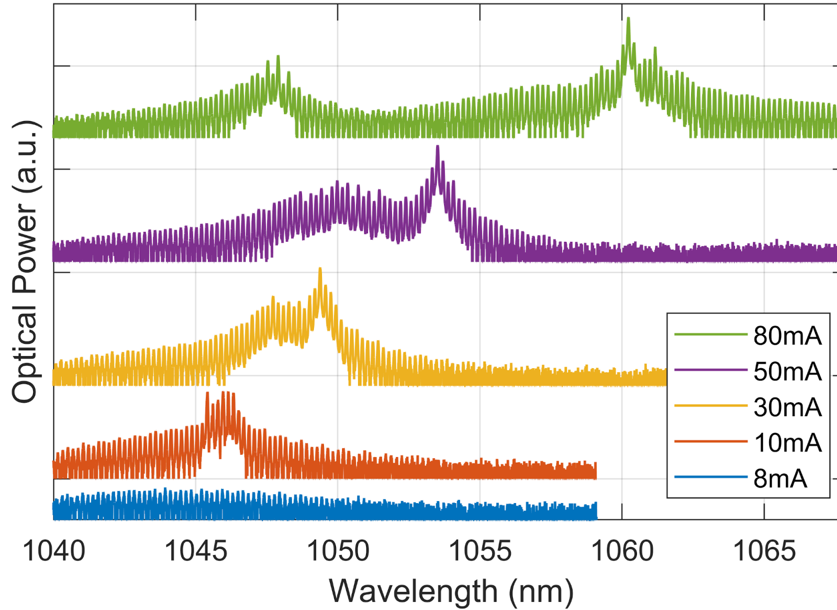

Figure 3.11: Lasing spectra for 3 µm wide active-passive laser with 400 µm long gain section and 400 µm long passive section under various levels of CW current injection.

same 3 µm wide active-passive laser from Fig. 3.11 was held at a constant 40 mA current level while the stage temperature was varied from 10 °C to 70 °C. The peak wavelength shifts to longer wavelengths at a rate of approximately 0.32 nm/°C as the temperature is increased. It should be pointed out that these measurements were performed under CW operation, so the actual temperature shift in the active region may be slightly higher than what is shown in the figure.

In this chapter, an active-passive PIC platform on GaAs was demonstrated for operation near 1030 nm. This platform integrates active sections, with passive sections, while maintaining state-of-the-art FP laser performance. In the next chapter, the design and fabrication of a widely tunable laser will be demonstrated on this platform. Such a tunable laser PIC is valuable, in particular for airborne or space-based Lidar applications

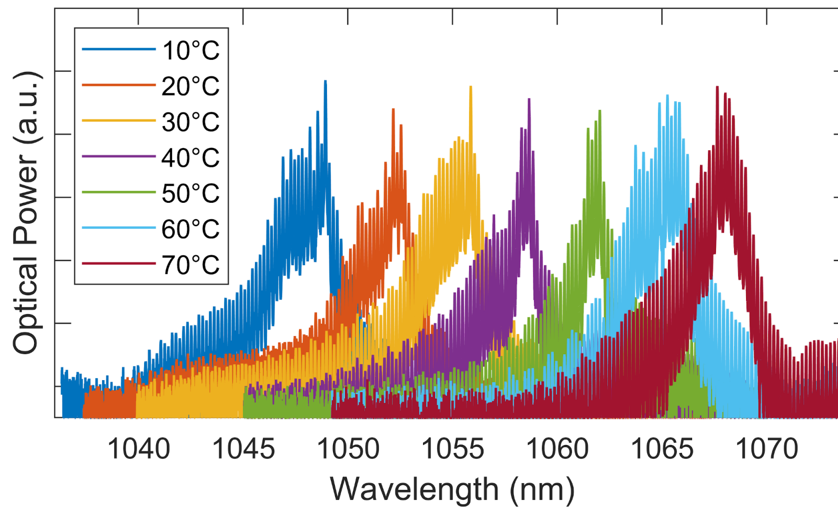

Figure 3.12: Lasing spectra with varying temperature for 3 µm wide devices at 40 mA CW current injection.

that require low system CSWaP for deployment on small platforms.

Chapter 4

Widely Tunable GaAs Lasers

Tunable semiconductor lasers are relevant for a variety of applications ranging from wavelength division multiplexing (WDM) systems used for optical communications, to Lidar and free space optical communications, and other sensing applications [5, 32, 33]. Originally developed for WDM around 1550 nm [99], the sampled grating distributed Bragg reflector (SGDBR) laser has since been demonstrated for a variety of applications [5, 32, 33, 47, 100], primarily on InP. While there have been some demonstrations of similarly wide tuning SGDBR lasers on GaAs for operation near 1 µm [101, 102], these are significantly less mature than their InP based counterparts. In this chapter, the active-passive GaAs PIC platform discussed in chapter 3 is utilized to demonstrate a SGDBR laser centered around 1030 nm with greater than 20 nm tuning range. This effort was part of a Nasa funded project with the goal of developing a widely tunable laser source for remote sensing of foliage, water and ice. Nasa's Ice Cloud and Land Elevation Satellite (ICESat) and ICESat-2 missions [39, 76, 103] have been used specifically to measure the changes in ice sheets and sea ice which have occurred due to climate change in recent decades. This is shown schematically in Fig. 4.1. ICESat is equipped with 1064 nm Nd-YAG lasers (it also uses frequency doubling for a 532 nm channel). However, Nd-YAG lasers are bulky and inefficient compared to semiconductor lasers which is an issue for space-based systems where low SWaP is critical. The goal of this project was to develop

a suitable semiconductor laser, with low SWaP, for potential use on similar missions in the future. Wavelength tunability can be used in conjunction with a diffractive optical element (DOE) to split the beam into multiple spots [104]. The laser spots are pulsed with a repetition rate of ∼10 kHz (higher than this and the pulses become indistinguishable) and elevation is measured using the time-of-flight (TOF) technique. By using multiple spots with different wavelengths, a higher effective repetition rate is achieved even though each individual spot is limited to 10 kHz. This places a requirement on the laser's tuning speed as well as total tuning range - higher tuning speed allows for more individual spots. The target metrics for the tunable laser in this project are shown in Table 4.1.

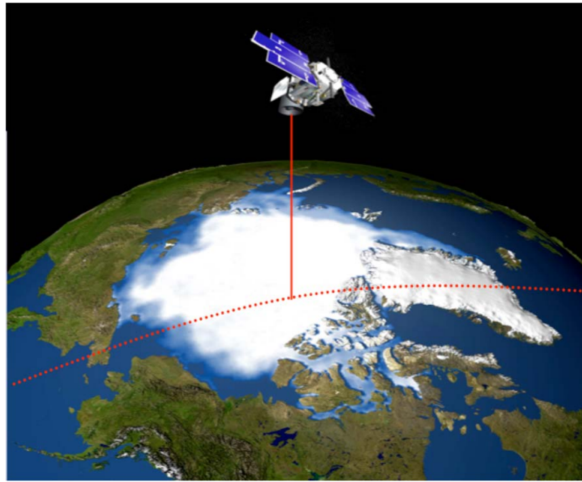

Figure 4.1: Schematic diagram of NASA's ICESat over the Arctic. Figure adapted from [39].

Table 4.1: Laser Specifications

Wavelength	Tuning Range	Output power	Laser Linewidth	Tuning Speed
1030 nm	20 nm	> 10 mW	< 10 MHz	> 1 MHz

4.1 Sampled Grating Distributed Bragg Reflector Mirrors

There are many different architectures that have been implemented to realize extended tuning range in lasers [105]. For this work, the SGDBR implementation was chosen since the tuning range is sufficient to reach 20 nm, the fabrication complexity is relatively low and it is compatible with the GaAs active-passive integration platform described in chapter 3. The essential concept of any grating mirror is that a periodic variation of the refractive index in the propagation direction creates small reflections at each interface. When the period of the grating is equal to half of the optical wavelength in the material, these small reflections will be in phase, leading to a large net reflection. This is known as the Bragg condition. For a basic DBR mirror this results in a strong peak in the reflectivity spectrum at the Bragg wavelength. The strength of the reflection is determined by the difference in effective index in a single period, and the total length of the grating. By modulating the index of refraction in the mirrors, the Bragg wavelength shifts, which leads to a shift in the lasing wavelength - i.e. tuning. For a DBR mirror, total tuning range is directly dependent on the magnitude of the shift in refractive index. The relation between change in refractive index and the corresponding wavelength shift is,

$$\frac{\Delta\lambda_g}{\lambda_g} = \frac{\Delta\bar{n}_{DBR}}{\bar{n}_{DBR}} \tag{4.1}$$

where λ_g is the Bragg wavelength and $\bar{n}_{DBR}$ is the effective index of the DBR.

For InP based DBR mirrors utilizing carrier injection tuning, this results in a wavelength shift of about 8-9 nm [80, 106]. However, for some applications a wider tuning range is desirable so a different architecture is required. Sampled grating DBR (SGDBR) mirrors extend the concept of DBRs, but rather than continuous gratings over some

length, the grating is periodically blanked to create short grating bursts separated by blank waveguide sections. This spatial modulation of the DBR results in a comb-like reflectivity spectrum with periodic reflection peaks in wavelength space. In a four-section SGDBR laser, the front and back mirrors are designed such that the peaks in their reflectivity spectra have slightly different spacing. Adjacent peaks can be aligned with a relatively small amount of tuning in one or both mirrors to achieve significant shift in the wavelength by exploiting the Vernier effect. Fig. 4.2(a) shows a schematic of a four-section SGDBR laser and a close-up of the SGDBR mirror section and Fig. 4.2(b) shows the simulated reflectivity spectrum of a single SGDBR mirror. Z_1 is the length of a single grating burst, Z_0 is the spacing between bursts or the sampling period, d is the grating etch depth, and Λ is the grating period. The coupling constant for a sampled

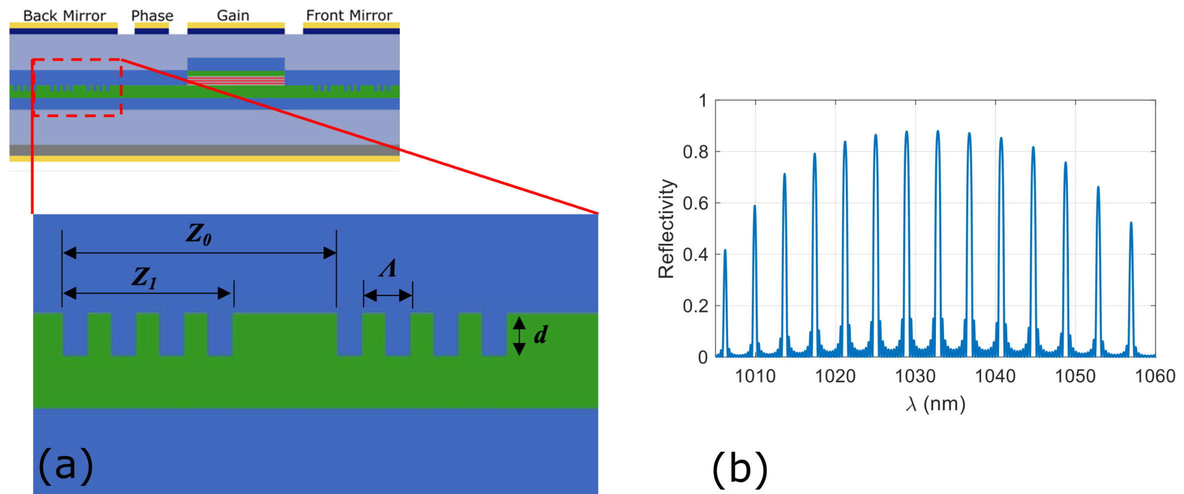

Figure 4.2: (a) Four section SGDBR laser with close-up view of SGDBR mirror and (b) example of simulated reflectivity spectrum for a single SGDBR mirror.

grating is given by the following equation,

$$\kappa_p = \kappa_g \frac{Z_1}{Z_0} \frac{sin(\pi p Z_1/Z_0)}{\pi p Z_1/Z_0} e^{-j\pi p Z_1/Z_0}, \tag{4.2}$$

where p is an integer representing the order of the peak ($p = 0$ for the central peak),

and κ_g is the coupling constant for an unsampled grating. The spacing between adjacent peaks is determined by the sampling period Z_0 and is given by,

$$\Delta\lambda_{peak} = \frac{\lambda^2}{2\bar{n}_g Z_0} \tag{4.3}$$

and the bandwidth of the envelope is obtained from the grating burst length Z_1 with

$$\Delta\lambda_{env} = \frac{\lambda^2}{2\bar{n}_g Z_1} \tag{4.4}$$

Another useful metric when designing SGDBR mirrors is the repeat mode spacing, which roughly corresponds to the maximum tuning range. This represents the range over which only one reflection peak in each mirror spectrum can be aligned to each other, and is calculated with

$$\Delta\lambda_{rep} = \frac{\Delta\lambda_{FM} \cdot \Delta\lambda_{BM}}{|\Delta\lambda_{FM} - \Delta\lambda_{BM}|} \tag{4.5}$$

where $\Delta\lambda_{FM}$ and $\Delta\lambda_{BM}$ are the peak spacing for the front and back mirrors, respectively.

An accurate method for obtaining the reflectivity spectrum is to use the **S** and **T** matrix method, as described in [80]. The simulated reflectivity shown in Fig. 4.2(b) was obtained with this approach.

4.2 Tunable Laser Design

The SGDBR laser is a four-section device consisting of front and back mirrors, a passive phase shifting section, and a gain section as shown in the diagram in Fig 4.3. Mirrors for this laser were designed to meet the 20 nm tuning range metric, with continuous tuning. MATLAB was used to create a transmission matrix model for each mirror, and an iterative approach was employed to finalize the dimensions (i.e. burst length,

sampling period, etch depth, and grating pitch). Several different mirror variants were designed and placed on the final mask layout.

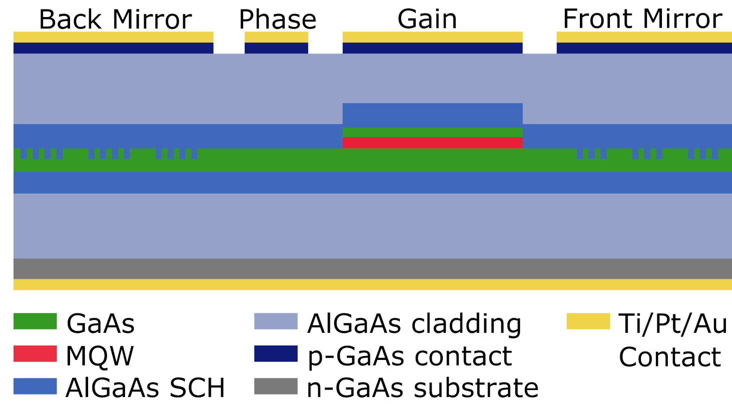

Figure 4.3: Side view diagram of a four section SGDBR laser.

4.2.1 Transmission Matrix Method

The transmission matrix method can be used to represent gratings with a series of **T**-matrices [80], which are 2x2 matrices of the form,

$$\mathbf{T} = \begin{bmatrix} T_{11} & T_{12} \\ T_{21} & T_{22} \end{bmatrix}. \tag{4.6}$$

Grating mirrors typically consists of a combination of just two elements, each with its own **T**-matrix: a dielectric interface, and a blank waveguide section, or transmission line. The **T**-matrix representing a dielectric interface going from medium 1 to medium 2 is given by,

$$\mathbf{T} = \frac{1}{t_{12}} \begin{bmatrix} 1 & r_{12} \\ r_{12} & 1 \end{bmatrix} \tag{4.7}$$

where r_{12} and t_{12} are the reflection and transmission at the interface, respectively. A waveguide of length L simply imposes a phase shift on the propagating mode, and the

corresponding **T**-matrix is,

$$\mathbf{T} = \begin{bmatrix} e^{j\phi} & 0 \\ 0 & e^{-j\phi} \end{bmatrix} \tag{4.8}$$

where $\phi = \tilde{\beta}L$ is the phase shift, and $\tilde{\beta}$ is the complex propagation constant in the material. Because $\tilde{\beta}$ is complex, it also includes any propagation loss that may be present in the waveguide. For rectangular gratings, the reflection and transmission coefficients can be approximated from the modal effective indices $\bar{n}_1$ and $\bar{n}_2$ in the two waveguide segments (etched and unetched grating regions). The reflectivity going from region 1 to region 2 is then given by,

$$r_{12} \approx \frac{\bar{n}_2 - \bar{n}_1}{\bar{n}_2 + \bar{n}_1} \tag{4.9}$$

and the transmission can be obtained with

$$r_{12}^2 + t_{12}^2 = 1. \tag{4.10}$$

It can easily be seen from (4.7) that going from region 2 to region 1 simply reverses the sign of the reflection coefficient, $r_{21} = -r_{12}$ and thus $t_{21} = t_{12}$. To obtain the total **T**-matrix for a grating mirror, individual matrices for each element in the mirror must be cascaded together. A single grating period consists of four **T**-matrices as shown in Fig 4.4, so the matrix for a single period is given by $\mathbf{T}_p = \mathbf{T}_1\mathbf{T}_2\mathbf{T}_3\mathbf{T}_4$. The matrix for a grating burst is then $\mathbf{T}_b = {\mathbf{T}_p}^m$ where m is the number of periods in a single grating burst. $\mathbf{T}_b$ can then be multiplied by the matrix for the waveguide section between bursts, $\mathbf{T}_{wg}$ and then raised to the number of bursts to obtain the total **T**-matrix for the entire SGDBR mirror, $\mathbf{T}_{SGDBR}$. From the final **T**-matrix, $\mathbf{T}_{SGDBR}$, the total reflection coefficient is simply $r = T_{21}/T_{11}$, and the power reflectivity is $R = |r|^2$.

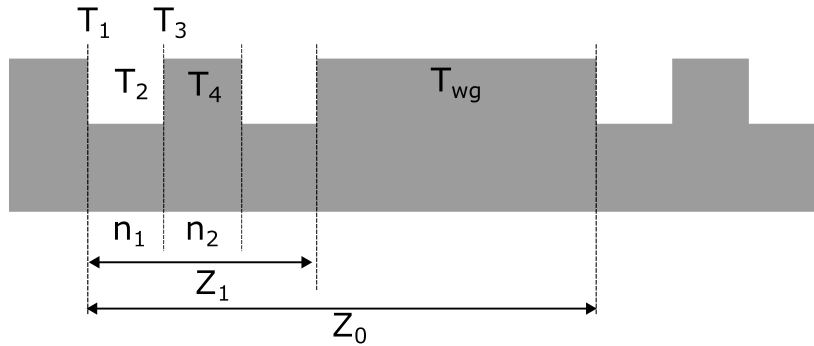

Figure 4.4: Diagram of grating period and corresponding **T**-matrices.

4.2.2 Mode Effective Index Simulations

Lumerical MODE simulations were used to calculate the effective indices for the transmission matrices. Using a grating etch depth of 35 nm, the mode was simulated in the etched area and the unetched areas of the grating. The simulation wavelength was swept over a 100 nm bandwidth centered around 1030 nm. Results from the wavelength sweep simulation are depicted in Fig. 4.5(a), which shows the simulated effective indices versus wavelength. The etch depth of the gratings was also swept in the simulation from 0 to 60 nm, and Fig. 4.5(b) depicts the calculated coupling constant, κ for the unsampled grating as a function of grating etch depth at a wavelength of 1030 nm.

4.2.3 SGDBR Mirror Variants

Multiple SGDBR laser variants were designed and included on the mask for fabrication. Various parameters for the six different design are summarized in the following tables. Table 4.2 is for the front mirror designs, Table 4.3 is for the back mirrors, and Table 4.4 is for the total mirror (i.e. combination of the front and back mirrors for each of the six different designs).

In Table 4.4, 'Peak R' is the peak total mirror reflectivity when the central mirror peaks are aligned, and 'FWHM' is the full-width half maximum of this reflectivity peak.

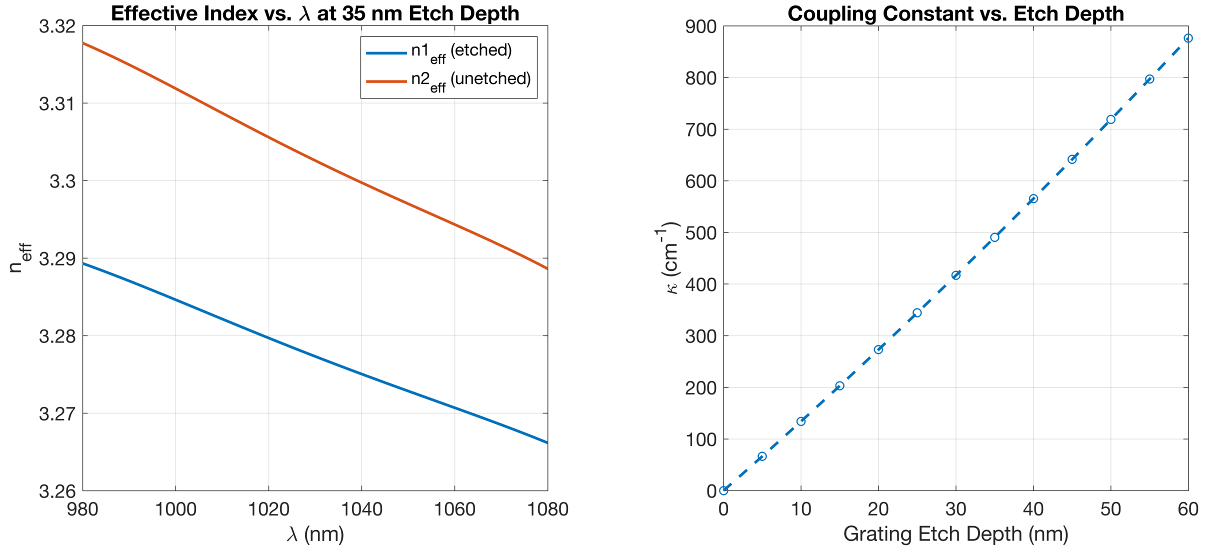

Figure 4.5: (a) Fundamental mode effective index vs. wavelength for a 35 nm deep grating etch and (b) coupling constant κ vs. etch depth.

Table 4.2: Front Mirror Parameters.

Design	$\Delta\lambda_{peak}$ (nm)	Z_1 (μm)	Z_0 (μm)	N_{bursts}	L (μm)	Peak R
1	4.450	0.780	33.112	10.000	331.124	0.116
2	4.450	1.248	32.959	10.000	329.587	0.253
3	4.450	1.560	32.960	10.000	329.598	0.355
4	4.450	1.560	32.960	12.000	395.517	0.449
5	5.750	0.936	25.496	10.000	254.962	0.161
6	3.300	1.248	44.462	8.000	355.692	0.173

Table 4.3: Back Mirror Parameters

Design	$\Delta\lambda_{peak}$ (nm)	Z_1 (μm)	Z_0 (μm)	N_{bursts}	L (μm)	Peak R
1	5.000	3.120	29.546	15.000	443.183	0.896
2	5.000	3.120	29.546	15.000	443.183	0.896
3	5.000	3.120	29.546	15.000	443.183	0.896
4	5.000	3.120	29.546	15.000	443.183	0.896
5	6.300	3.120	23.328	16.000	373.244	0.918
6	3.900	3.744	37.631	11.000	413.940	0.864

Fig. 4.6(a) shows the simulated reflectivity spectra for the front and back mirrors of design 6, and Fig. 4.6(b) is the total mirror reflectivity of the two mirror spectra multiplied together. The center wavelength for this design is 1032.8 nm. This value is not

Table 4.4: Total Mirror Parameters.

Design	Peak R	FWHM (nm)	Approx. Tuning Range (nm)
1	0.095	0.380	40.455
2	0.218	0.410	40.455
3	0.309	0.420	40.455
4	0.392	0.380	40.455
5	0.139	0.510	65.864
6	0.143	0.370	21.450

at exactly 1030 nm because the grating dimensions must be an integer multiple of 1 nm, which is the resolution of the electron beam lithography (EBL) system used for writing the gratings and 1032.8 nm was the closest peak given this constraint. Fig. 4.6(c) is a microscope image of a fabricated laser with these mirror designs, with the relevant section lengths indicated. This design ended up demonstrating the best overall performance and was the only one capable of demonstrating continuous tuning between supermodes. In order to provide effective mode filtering and ensure single-mode operation, the FWHM of the total reflectivity spectrum must be narrow enough to select only one cavity mode. Cavity mode spacing is given by the following equation [80], and for the laser design in Fig. 4.6, design 6, this comes out to 0.31 nm.

$$d\lambda = \frac{\lambda^2}{2\left(\bar{n}_{ga}L_a + \bar{n}_{gp}L_p + \bar{n}_{gp}L_{eff}\right)} = 0.31\,\mathrm{nm} \tag{4.11}$$

Here, $d\lambda$ represents the cavity mode spacing, $\bar{n}_{ga}$ is the group index in the active section, $\bar{n}_{gp}$ is the group index in the passive section, L_a is the active region length, L_p is the total passive length excluding the mirrors (in this case, the phase section), and L_{eff} is the effective length of the two mirrors. Fig. 4.7 shows the position of the cavity modes superimposed on the central reflectivity peak from Fig. 4.6(b) showing that the FWHM, 0.37 nm, is narrow enough to filter out a single cavity mode.

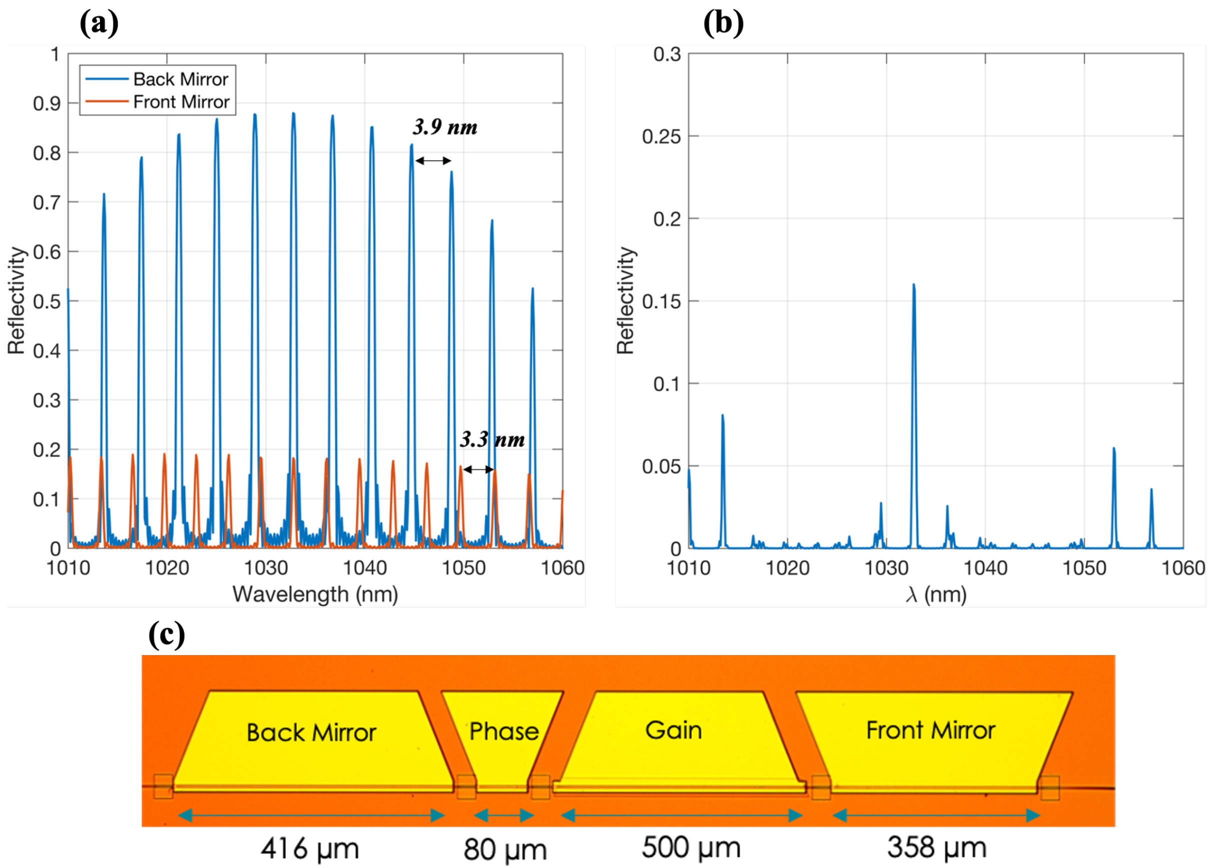

Figure 4.6: (a) Simulated reflectivity spectra of front and back SGDBR mirrors for design 6, (b) total reflectivity sepctrum for laser design 6, and (c) microscope image of fabricated laser with section lengths indicated.

4.3 Tunable Laser Fabrication

The SGDBR lasers were fabricated on the same platform described in chapter 3, so the fabrication steps are essentially the same but with the addition of grating lithography and etching after the active-passive isolation etch. The base epitaxy, before regrowth, is identical to what is shown in Table 3.1, but the regrowth layers are slightly modified for the tunable lasers as described below.

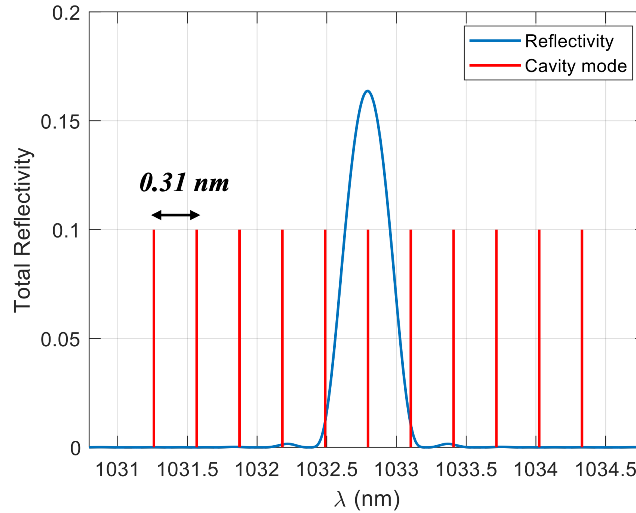

Figure 4.7: Cavity mode spacing overlaid on total mirror reflectivity spectrum of design 6 showing effective mode filtering capability.

4.3.1 Mask Layout

The mask layout for a single die is shown below in Fig. 4.8(a). This layout included all the SGDBR mirror variations listed in the previous section, as well as SGDBR lasers with SOA gain sections after the front mirror and absorbers at the back. A few test structures such as TLM patterns and Fabry Perot lasers are also included. Fig. 4.8(b) shows a microscope image of a full die after fabrication and a close-up of two four-section SGDBR lasers.

4.3.2 Grating Formation

The first step in the fabrication was the active-passive etch to isolate the gain and passive sections. This was performed in the same manner as described in chapter 3. After active-passive etching, electron beam lithography (EBL) was used to pattern the gratings for the laser mirror sections. First a 25 nm thick SiO_2 hard mask is deposited, followed by spinning on EBL resist. The resist is then exposed with EBL and developed, and the

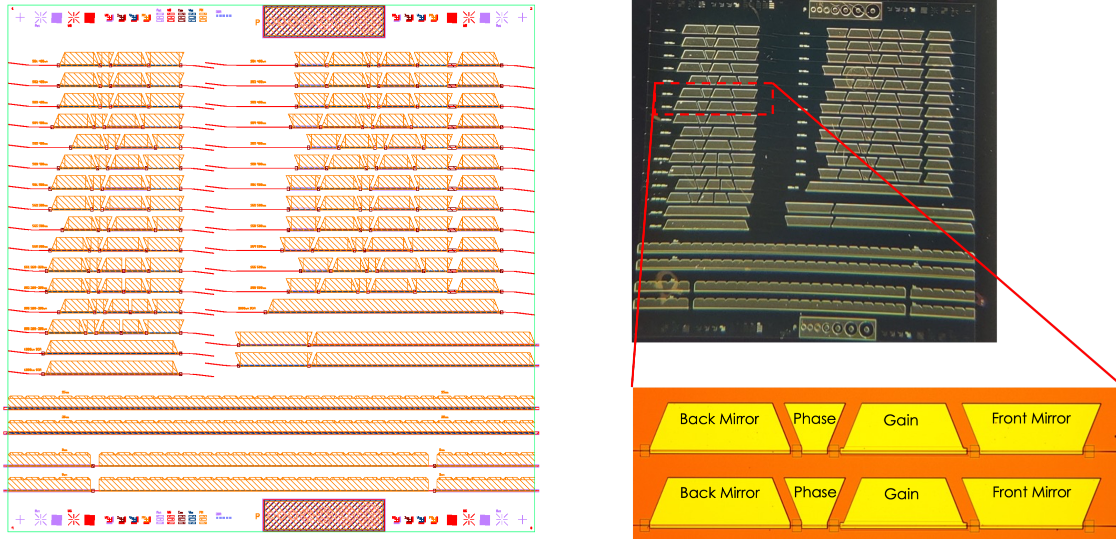

Figure 4.8: (a) Mask layout and (b) microscope image of fabricated die with close up of four section SGDBR laser in inset.

hard mask is etched with CF_4/CHF_3 ICP dry etching. The EBL resist is then stripped and the gratings are etched into the GaAs waveguide layer. For the grating etch, an ICP dry etch recipe with a slow etch rate was developed using Cl_2/N_2 gas chemistry - the rate was approximately 90 nm/min. Before forming gratings on the real device samples, a calibration mask was used to optimize the dose and current of the EBL on a dummy sample to achieve consistent gratings with close to 50% duty cycle. Fig. 4.9(a) shows an SEM image of the etched gratings with 157 nm pitch and 74 nm wide etched regions. Fig. 4.9(b) is a cross section SEM of gratings etched on one of the calibration samples, with the hard mask still intact on the top. The final depth of the gratings for the real samples was measured with atomic force microscopy (AFM) and was 37 nm. Fig. 4.9(c) shows this AFM scan.

4.3.3 Regrowth and Remaining Fab

After etching the gratings, the upper SCH layers, p-cladding and p-contact were regrown by MOCVD. The regrowth layer details are shown in Table 4.5; the underlying

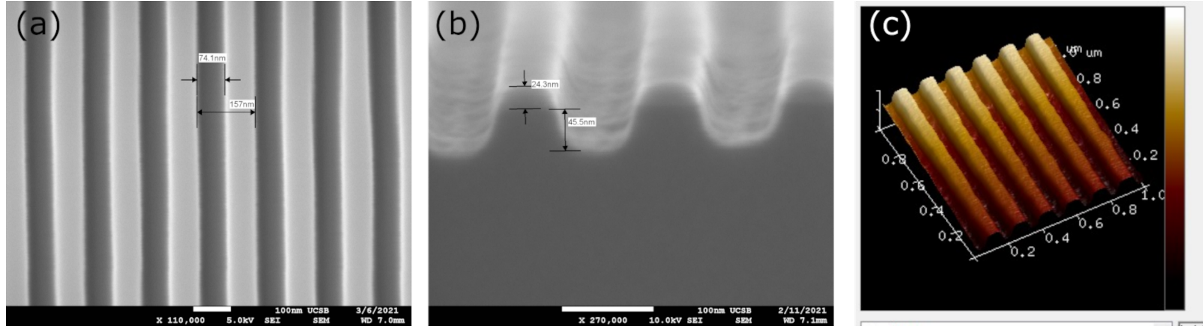

Figure 4.9: (a) Top-view SEM of etched gratings, (b) cross-section SEM image of gratings, and (c) AFM image showing 37 nm etch depth.

epi is identical to what was used in chapter 3 and can be found in Table 3.1. The sample was prepared for regrowth with UV ozone followed by a dip in a buffered hydrofluoric acid (BHF) solution diluted with DI water. This removes the hard mask from the grating etch and any native oxide that may have formed on the GaAs surface. The sample was then immediately loaded into the MOCVD reactor to avoid extended exposure to air and reduce the chance of additional native oxide forming on the surface. After regrowth,

Table 4.5: Regrowth Layers for SGDBR Laser

	Material	**Thickness (nm)**	**Doping (cm^{-3})**
Regrowth Layers	GaAs	200	(p) 1e20
	$Al_{0.4}GaAs$	200	(p) 5e17
	$Al_{0.6}GaAs$	1000	(p) 6e17
	$Al_{0.2}GaAs$	120	(p) 1e17
	$Al_{0.1}GaAs$	40	(p) 1e17
	$Al_{0.1}GaAs$	10	(p) 1e18

the remaining fabrication steps - waveguide ridge formation, passivation, via opening, and contact deposition - are identical to the process described in chapter 3. One small sample was shipped out for imaging of the gratings. A focused ion beam (FIB) cut was performed in the grating section and scanning tunneling electron microscopy (STEM) was used to image the overgrown gratings. The results from this analyis are shown in

Fig. 4.10 with the location of the FIB cut indicated as well as a close up image of the gratings. The gratings are clearly present and the regrowth interface looks very clean, although the shape of the gratings is slightly rounded compared to the images before regrowth, however this is to be expected due to the high growth temperature which causes the surface to coalesce slightly.

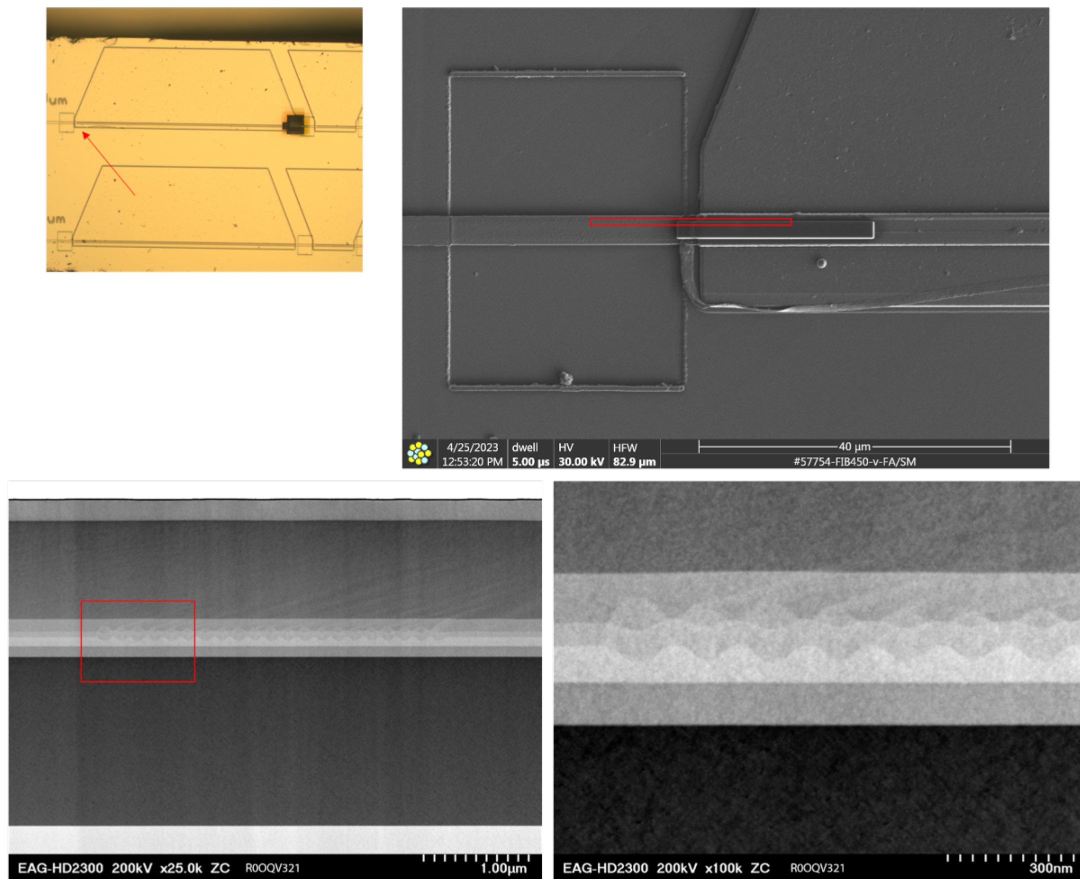

Figure 4.10: FIB cut and STEM image of the gratings after regrowth.

4.3.4 Cleaving and Mounting Laser Bars

After fabrication the sample was thinned down to about 150 µm before depositing backside n-contact metal and singulating individual die. Several die were then sent out for laser bar cleaving and anti-reflection coating of the SGDBR laser facets. Multiple

individual lasers were tested to select the highest performance devices to be cleaved and mounted to an AlN carrier. Fig. 4.11(a) shows two lasers that were cleaved from a larger bar and soldered to a carrier provided by Freedom Photonics. The four contacts on the laser are wirebonded to metal contact pads on the carrier for easier probing. In this picture there are two lasers on the bar but only one is wirebonded - this is because the lasers are spaced too closely on the mask to reliably cleave out one at a time. Fig. 4.11(b) is a side-view SEM image of a similar bar with two lasers, soldered to a carrier. In this case both lasers are wirebonded to metal pads on the carrier.

Mounting and wirebonding facilitates easier characterization as the metal pads on the carrier are easier to probe than the pads on the laser, and the carrier is easier to handle than the small bars. Additionally, mounted devices typically perform better because the backside n-contact is soldered to the metal on the carrier, which reduces resistance (as opposed to setting the bar on a copper stage, which would be the alternative). The AlN carrier also creates a better heatsink for greater thermal stability. All the measurement data presented in the following section was obtained from mounted and wirebonded laser bars.

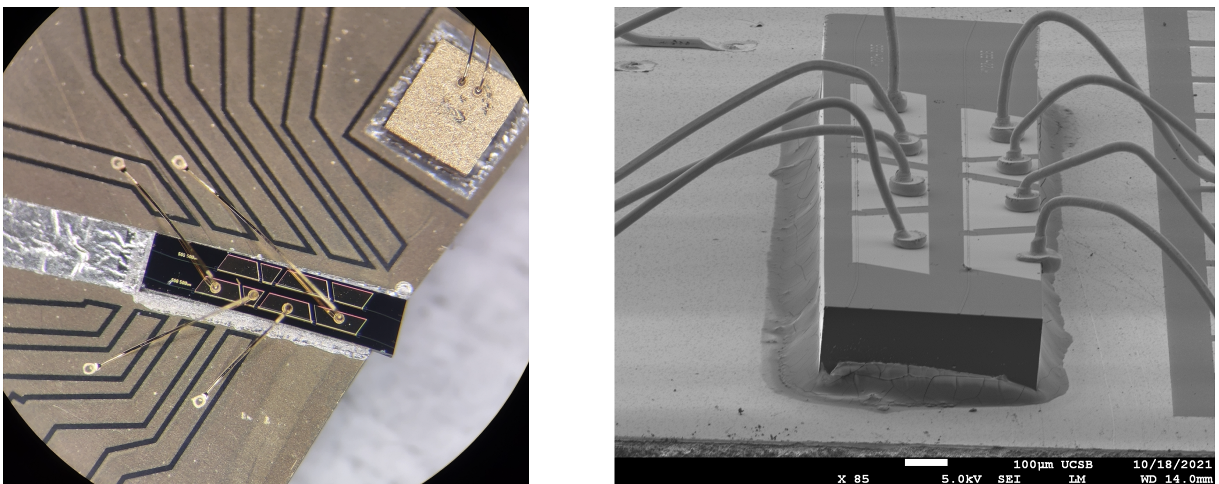

Figure 4.11: (a) Microscope image of cleaved four section SGDBR laser bar mounted and wirebonded to AlN carrier and (b) side view SEM of a similar device also mounted and wirebonded.

4.4 Laser Measurements

Thorough testing of the fabricated lasers was performed to characterize their performance in terms of both power output and tunability.

4.4.1 Laser Power Output

Fig. 4.12 shows a typical LIV characteristic for a four-section SGDBR laser mounted on a carrier - in this case laser design number 6. This measurement was performed at room temperature under CW operation and without any tuning of the mirror or phase sections. The lasing threshold current is 20 mA and greater than 35 mW is demonstrated out of the front mirror facet at 100 mA current injection. Tuning the wavelength via

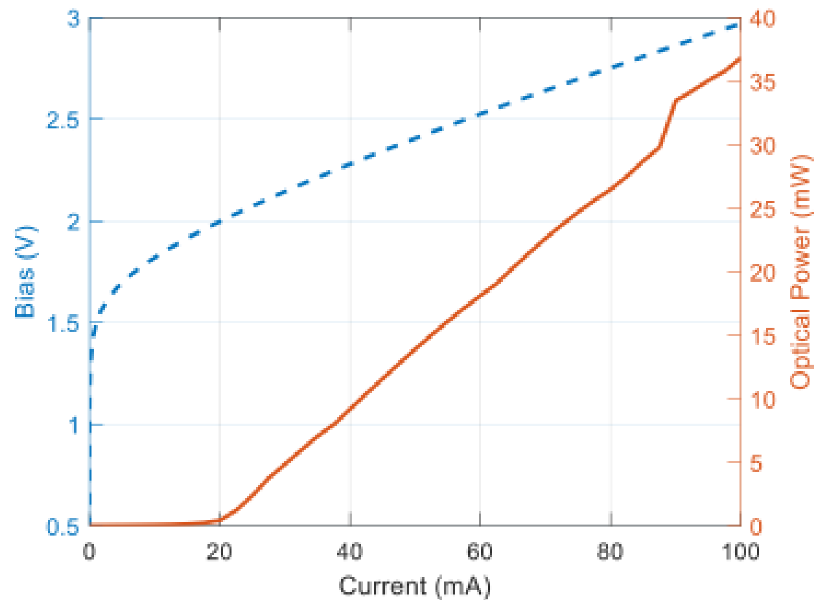

Figure 4.12: LIV characteristic from SGDBR laser design number 6 after antireflection coating and mounting to AlN carrier. Optical power shown here is only out of the front mirror facet and exhibits more than 35 mW output at 100 mA CW current injection.

current injection in the front and back mirrors induces excess loss due mainly to free-carrier absorption in the mirror sections. This loss is quantified in Figure 4.13 where the

current in the gain section was held steady while the front and back mirror currents were swept from 0 to 150 mA. Fig. 4.13(a) shows the power decrease as a function of front mirror current, Fig. 4.13(b) shows power decrease as a function of back mirror current and Fig. 4.13(c) shows power decrease as a function of the current in both mirrors. In Fig. 4.13(c) the total power decreases from 44 mW with no tuning to about 15.1 mW when both mirrors are being driven at 150 mA. This represents a total loss of approximate 4.6 dB. As will be shown in the next section, 150 mA in both mirrors is sufficient to tune continuously across the whole range, however coarse tuning between the channels requires significantly less total current and only one mirror section at a time.

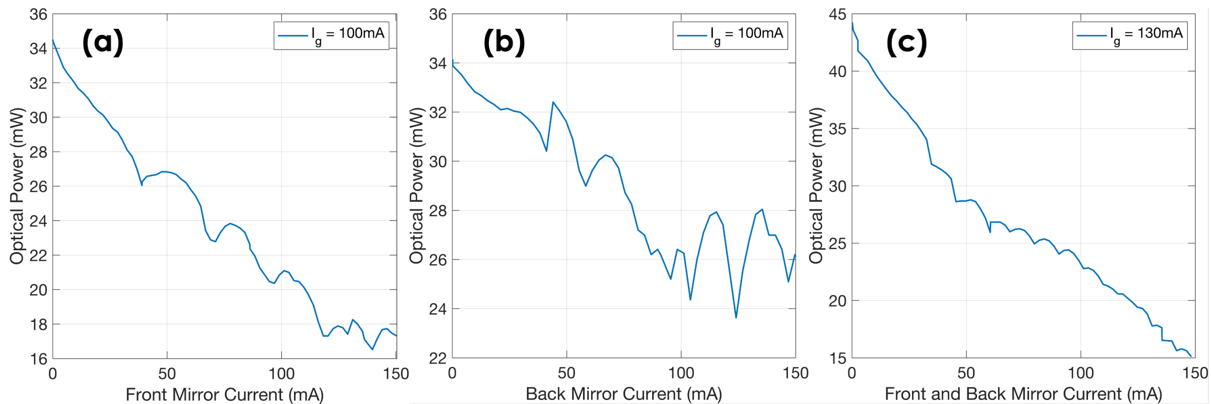

Figure 4.13: Total power output while varying mirror current from 0 to 150 mA in (a) front mirror, (b) back mirror and (c) both mirrors simultaneously.

4.4.2 Wavelength Tuning

Wavelength tuning is accomplished by injecting current into the mirror and phase sections to modulate the refractive index and shift the peak of the mirror's reflectivity and the position of the cavity modes. As can be seen in the simulated reflectivity spectra in Fig. 4.6(a), a small shift in one of the mirrors will align different reflection peaks and cause a mode hop from the central peak to the newly aligned peaks. This is known as coarse tuning and is accomplished by tuning only one mirror at time. The laser's

tuning characteristics were obtained by coupling light from one of the mounted SGDBR lasers to an optical fiber and observing the spectrum on an optical spectrum analyzer (OSA). Fig. 4.14(a) is an overlay plot of the 8 different channels that can be accessed with coarse tuning in either the front or back mirror. Coarse tuning alone covers a total range of 22.2 nm spanning from 1026.1 nm to 1048.3 nm, which meets the target tuning range from Table 4.1. In this plot each of the 8 channels demonstrates a side-mode suppression ratio (SMSR) of 30 dB or greater. The front and back mirrors can also be tuned simultaneously. Again referring to Fig. 4.6(a) simultaneous tuning will shift both the front and back mirror spectra together, which tunes a single channel rather than mode-hopping to an adjacent one. This allows access to the wavelengths between channels. Fig. 4.14(b) demonstrates continuous tuning between the first two channels. In this plot, the blue curve is the free-running wavelength (no mirror current), and the red curve is the first accessible channel using coarse wavelength tuning of only the back mirror. Starting with the free-running laser (blue), current was injected into both mirrors simultaneously to tune that channel. This is represented by the yellow curve which demonstrates that the first channel can be tuned across the whole range between the first and second channels. In this case the yellow curve required 130 mA in the front mirror and 145 mA in the back mirror.

A wavelength tuning map was generated by tuning both mirrors in 1 mA steps from 0 to 150 mA and recording the peak wavelength of each point. This creates a 151x151 grid of wavelength points corresponding to every front-back mirror current combination. This wavelength map is shown in Fig. 4.15(a). Each point required approximately 2 seconds to give the OSA sufficient time to take an accurate measurement, so it took over 12 hours of continuous testing to acquire the data for this figure. Since each measurement recorded the full spectrum, the SMSR at each wavelength point can also be obtained. Fig. 4.15(b) shows a similar map of SMSR as a function of front and back mirror current.

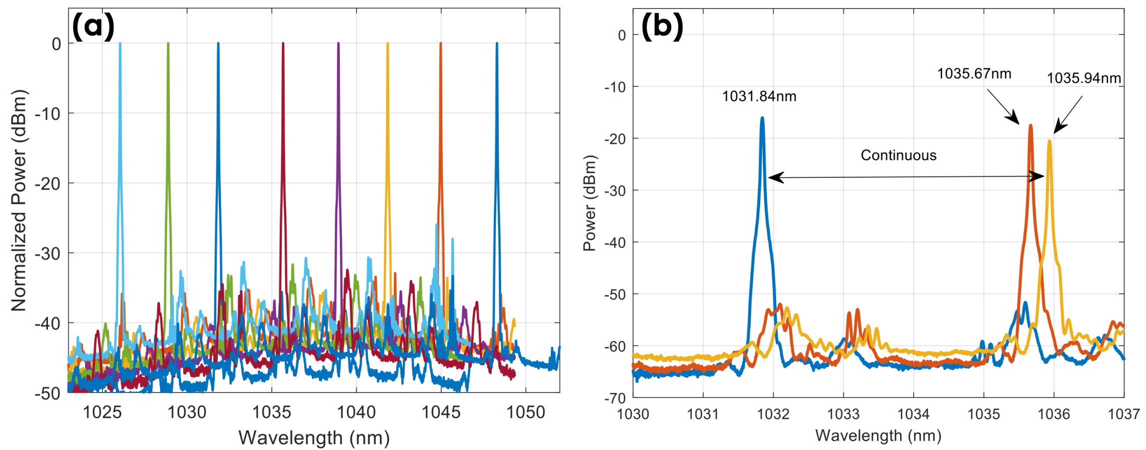

Figure 4.14: (a) Overlaid spectra of 8 channels accessible with coarse tuning and (b) demonstration of continuous tuning between the first and second channels with current injection into both mirrors.

In addition to the mirrors, the phase section adds another element of control over the output spectrum. Tuning the phase section changes the index in that section which in turn changes the effective length of the cavity without shifting the grating peaks. Referring back to Fig. 4.7 which shows the position of the cavity modes overlaid on the mirror spectrum, it can be seen that as the mirror peak is shifted, different cavity modes will fall into the reflection window. This leads to cavity mode hopping as the mirrors are tuned. However, if the phase section is tuned in addition to the mirrors, the cavity modes can be shifted along with the mirror spectrum to avoid this mode-hopping behavior. Figure 4.16(a) shows a plot of peak wavelength versus phase current without any mirror tuning. The clear steps in the plot indicate the points where one cavity mode is moved out of the reflection window and another moves in. Figure 4.16(b) shows overlaid spectra as the phase section is tuned, demonstrating 0.23 nm of tuning between mode hops. It is worth noting that the tuning maps shown in Figure 4.15 were obtained with only mirror current and no phase section tuning. The lines separating the channels in the SMSR plot of Fig. 4.15(b) show points with very low SMSR, however with the

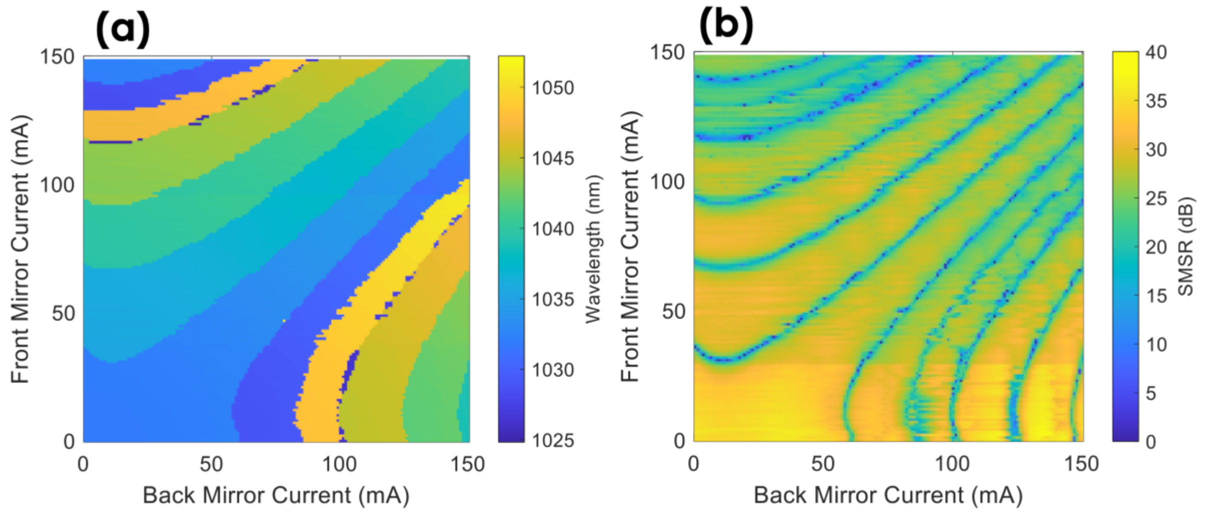

Figure 4.15: (a) Map of wavelength vs. front and back mirror current and (b) SMSR vs front and back mirror current.

addition of phase tuning many of these points could be tuned out to improve the SMSR as the laser is tuned between channels. The laser's Lorentizian linewidth was also measured to extract a linewidth of approximately 650 kHz, easily meeting the requirement of less than 10 MHz linewidth.

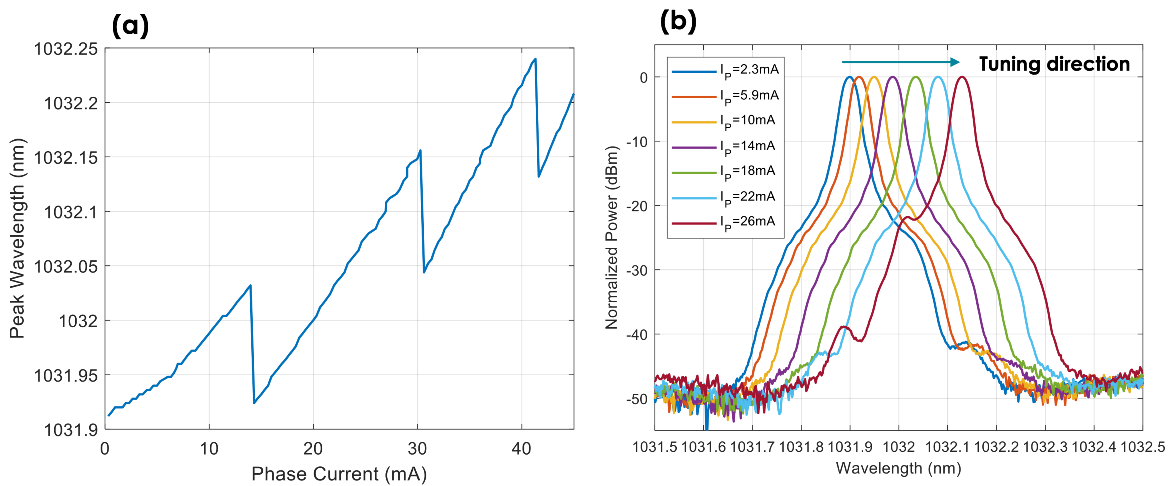

Figure 4.16: (a) Peak wavelength vs. phase section current and (b) overlaid spectra with varying phase section current and no mirror tuning.

4.5 Laser Packaging and Collaboration with Freedom Photonics

Several of the SGDBR laser bars were sent to Freedom Photonics for packaging and further testing. These were mounted on carriers like the one shown in Fig. 4.11(a) and then packaged in a butterfly package with fiber pigtail. Fig. 4.17 shows a typical butterfly package and Freedom Photonics' InstaTune module used for wavelength tuning measurements. Our collaborators at Freedom Photonics performed measurements with the packaged lasers such as the wavelength tuning map shown in Fig. 4.18 which was obtained using their InstaTune driver module.

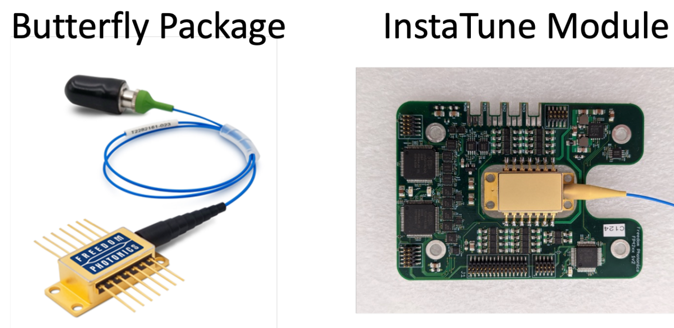

Figure 4.17: (Left) Butterfly package with fiber coupled output from Freedom Photonics and (right) InstaTune module for wavelength tuning measurements.

4.5.1 Wavelength Switching Experiment

One of the target metrics for these lasers was fast wavelength tuning speed (>1 MHz). A wavelength switching measurement can be performed by applying a square wave to the mirrors to tune between two wavelength points, filtering out one wavelength with an optical bandpass filter, and using a photodetector to observe the resulting waveform on an oscilloscope. This technique is described in [107]. Fig. 4.19 shows a screenshot of the oscilloscope waveform during this measurement when a square wave tuning current is

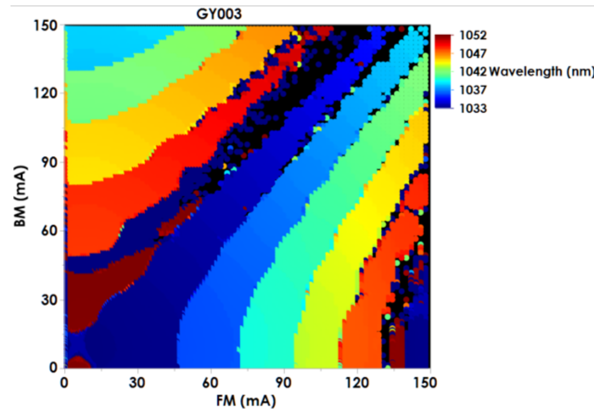

Figure 4.18: Tuning map showing wavelength versus front and back mirror current for one of the packaged SGDBR lasers.

applied with 200 µs pulse widths. The applied waveform tunes between two wavelengths, $\lambda_1 = 1033.419\ nm$ and $\lambda_2 = 1033.575\ nm$. The rise time when switching from λ_1 to λ_2 is significantly faster than the decay when switching from λ_2 to λ_1, indicating that there are two time constants influencing the tuning speed. Based on this measurement it is not possible to extract a single number for the wavelength switching speed. The next chapter will discuss in detail the physical mechanisms that influence wavelength tuning in GaAs, but briefly, the two primary mechansims are carriers and temperature. Carrier based effects are typically quite fast (MHz-GHz range) whereas temperature based tuning is slower (kHz range). The measurement in Fig. 4.19 shows a fast rise and slow decay, indicating that both effects may be influencing wavelength tuning in this laser.

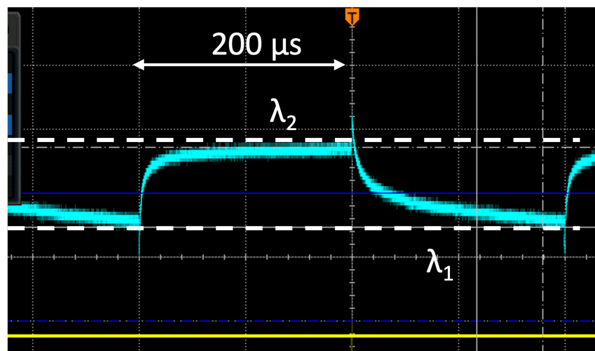

Figure 4.19: Screenshot of oscilloscope waveform during wavelength switching experiment using 200 µs pulses. Fast rise time and slow decay indicate two different time constants affecting the wavelength tuning speed.

Chapter 5

Wavelength Tuning Mechanisms in GaAs

For most tunable lasers, the desired shift in wavelength is directly related to a change in the index of refraction in the laser cavity. In the case of tunable DBR or SGDBR lasers, this tunability is achieved by varying the index in the mirror section(s) which translates to a shift in reflectivity spectrum and thus a shift in the lasing wavelength. There are several physical mechanisms that can contribute to a modulation of the refractive index and this chapter explores that physics, focusing primarily on GaAs. Section 5.1 covers the theory related to specific types of index tuning, such as carrier based tuning, and electric field related effects. Section 5.2 takes a closer look at data from the SGDBR lasers presented in chapter 4 to analyze the effects that may be influencing the observed behavior. Finally, section 5.3 presents data from a regrowth and time-resolved photoluminescence (TRPL) experiment to analyze the effect that surface preparation has on carrier recombination rates.

The real and imagninary parts for refractive index of GaAs, used in the simulations, were obtained from [108]. This n-k data, which was obtained experimentally, is plotted in Fig. 5.1 as a function of photon energy. Similar data was obtained from the same website for AlGaAs of various compositions. Absorption is related to the imaginary part

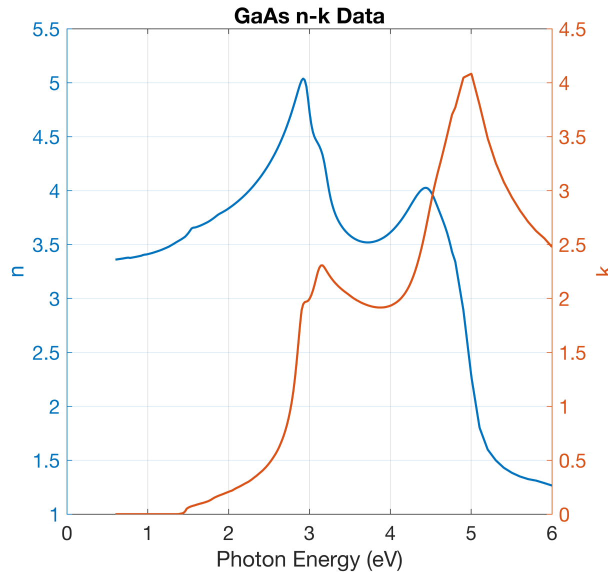

Figure 5.1: n-k data for GaAs

of refractive index, k, with the following equation,

$$\alpha_0 = \frac{4\pi \cdot k}{\lambda}. \tag{5.1}$$

This equation is used with the data in Fig. 5.1 to obtain experimental values for absorption, in the absence of carriers or electric field, and is used later for calculating the shift in index due to various effects.

5.1 Refractive Index Tuning

There are three primary effects that are commonly used to induce a shift, either positive or negative, in the refractive index of semiconductor devices. These are carriers (accomplished with current injection), electric fields (accomplished by applying forward or reverse bias), and temperature. While these all have different underlying physics they are, in practice, seldom isolated from each other. For example, injecting current requires

a forward bias which introduces an electric field and the associated power dissipation leads to heating in the device. In the context of laser engineering, it's important to understand which effects are dominant in order to predict the magnitude and sign of the resultant index shift, which in turn relates to the tuning efficiency. The discussion below assumes carrier injection due to forward biasing a diode, but the same effects also apply in the case of carrier depletion due to reverse bias. However, in the case of tunable lasers, the optical waveguide region where the index change is most relevant is typically undoped, or only lightly doped, so carrier depletion has a much smaller effect than carrier injection.

5.1.1 Carrier Based Effects

Carrier based tuning is not one single physical mechanism, but actually three different effects that each contribute differently to the overall shift in index [109, 110]. Often the change in absorption is more readily calculated and the corresponding change in index is then obtained via the Kramers-Kronig integral. For a given change in absorption, $\Delta\alpha$, the corresponding change in index is:

$$\Delta n = \frac{2c\hbar}{e^2}\, \mathcal{P} \int_0^\infty \frac{\Delta\alpha}{E'^2 - E^2} dE' \tag{5.2}$$

where $\mathcal{P}$ indicates the principal value of the integral, E is the photon energy, c is the speed of light, $\hbar$ is Planck's constant and e is the fundamental electron charge. A more thorough treatment of carrier based index tuning is given by Bennet et al. in [109], but a brief overview is provided here.

Bandgap Shrinkage

Bandgap shrinkage occurs when injected electrons occupy states at the bottom of the conduction band (and holes at the top of the valence band). When the carrier concentration is high, individual wavefunctions begin to overlap significantly. The electrons are repelled by the Coulomb force, and electrons with the same spin will avoid each other due to the Pauli exclusion principle. The net effect is a decrease in the elctrons energy to accomodate the overlapping wavefunctions and also the repellant forces, which results in a shift of the effective conduction band edge. The inverse is true for holes in the valence band thus causing the bandgap to shrink, hence the name. Based on the analysis from Bennet et al. [109], the total change in bandgap energy as a function of carrier density is,

$$\Delta E_g(\chi) = \begin{cases} \frac{\kappa}{\epsilon_s}\left(1 - \frac{\chi}{\chi_{\text{cr}}}\right)^{1/3} & \chi \geq \chi_{\text{cr}} \\ 0 & \chi < \chi_{\text{cr}} \end{cases} \tag{5.3}$$

where χ is the free carrier density (electrons or holes), κ is a fitting parameter, and χ_{cr} is the critical carrier density below which bandgap shrinkage effects are insignificant. The value for χ_{cr} used in [109] is given by the following which is a fit based on experimental data and is in units of cm^{-3}

$$\chi_{\text{cr}} = (1.6 \times 10^{24}) \cdot \left(\frac{m_e}{1.4\epsilon_s}\right)^3 . \tag{5.4}$$

If parabolic bands are assumed then the absorption coefficient near the bandgap can be modeled with the square root law as:

$$\alpha_0(E) = \begin{cases} \frac{C}{E}\sqrt{E - E_g} & E \geq E_g \\ 0 & E < E_g \end{cases} \tag{5.5}$$

where C is a constant that includes various material parameters. The change in absorption due to bandgap shrinkage is then simply obtained with

$$\Delta\alpha(\chi, E) = \alpha_0(E - \Delta E_g(\chi)) - \alpha_0(E) \tag{5.6}$$

and the resultant shift in index can be calculated from the Kramers-Kronig integral in (5.2). The change in absorption due to bandgap shrinkage is always positive for energies below the bandgap, and thus the change in index is also positive.

Band Filling

The band filling effect, unlike bandgap shrinkage, leads to a decrease in absorption (and thus negative index shift). This occurs when free carriers fill the lowest states in the conduction band. In order to for a photon to be absorbed, the energy must be high enough to excite electrons from the valence band to the conduction band. When the lowest energy states are filled, a higher energy is required for this excitation as the only available states are at energies further above the conduction band edge. This leads to a shift in the effective absorption edge to higher energies when the carrier density is high. The absorption coefficient for a semiconductor under current injection is given by,

$$\alpha(N, P, E) = \alpha_0(E) \left[f_v(E_a) - f_c(E_b) \right], \tag{5.7}$$

where N and P are the elctron and hole densities, respectively, $f_v(E_a)$ is the probability of a valence band state with energy E_a being occupied and $f_c(E_b)$ is the probability of a conduction band state with energy E_b being occupied. The probabilities f_c and f_v are

given by the Fermi-Dirac distribution,

$$f_c(E_b) = \left[1 + e^{(E_b - E_{Fc})/k_B T}\right]^{-1} \tag{5.8}$$

$$f_v(E_a) = \left[1 + e^{(E_a - E_{Fv})/k_B T}\right]^{-1} \tag{5.9}$$

where k_B is Boltzmann's constant, T is temperature and E_{Fc} and E_{Fv} are the quasi-Fermi levels, which are carrier dependent. Absorption as a function of carrier density can be calculated from (5.7) and the change in absorption is then simply

$$\Delta\alpha(N, P, E) = \alpha(N, P, E) - \alpha_0(E). \tag{5.10}$$

The corresponding change in index is again obtained with the Kramers-Kronig relation. There are multiple approximations for quasi-Fermi level as a function of carrier density [80], but for this the Nilsson approximation [111] was used as described in [109].

Free Carrier Absorption

A free carrier in a semiconductor can absorb a photon and move to a higher energy state. This free-carrier absorption, or plasma effect, also leads to a change in the refractive index. Using the Drude model for free carrier absorption [112], the change in index can be calculated directly from the carrier concentration and material parameters. The change in index due to the plasma effect is always negative and is given by [109],

$$\Delta n = -\left(\frac{e^2\lambda^2}{8\pi^2 c^2 \epsilon_0 n}\right)\left(\frac{N}{m_e} + \frac{P}{m_h}\right). \tag{5.11}$$

A Matlab script was written to calculate refractive index change in GaAs as a function of carrier concentration resulting from the 3 effects discussed above. The empirical data in

Fig. 5.1 was used as a starting point for the unperturbed index and absorption in GaAs. For bandfilling and bandgap shrinkage, the absorption shift was calculated directly and the Kramers-Kronig integral was solved numerically to obtain Δn. The results are plotted in Fig. 5.2 for 5 different carrier concentrations The sum of all three effects is shown in

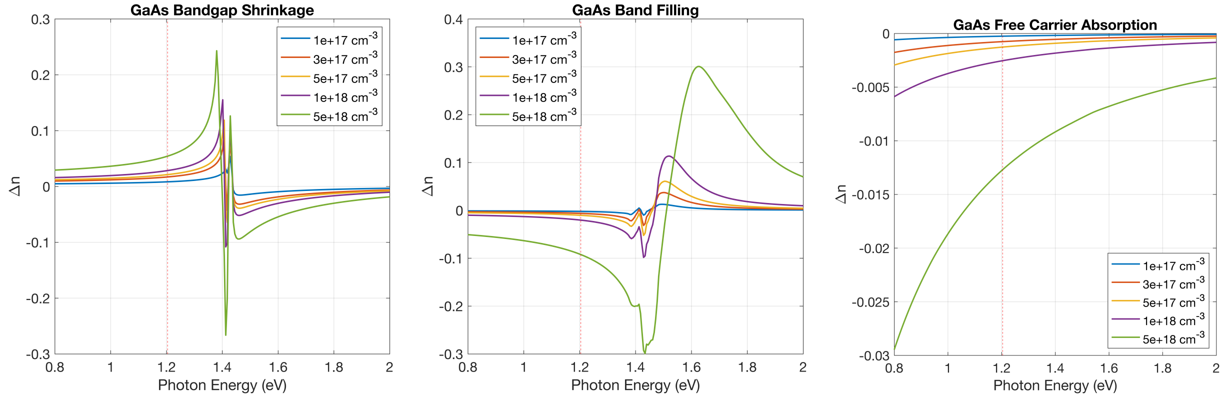

Figure 5.2: Carrier induced refractive index change in GaAs due to (a) bandgap shrinkage, (b) band filling, and (c) free carrier absorption. The vertical line in all three plots is at 1.204 eV which corresponds to a wavelength of 1030 nm.

Fig. 5.3(a) at a wavelength of 1030 nm. Fig. 5.3(b) is a plot from Bennet et al. [109] showing the same calculation as a function of electron concentration in n-type GaAs at a photon energy of 1.2 eV. The calculation in Fig. 5.3(a) compares favorably to the result from Bennet with the key difference being that the transition from a net positive index change to net negative index change occurs at a higher carrier concentration in our calculation. However, our calculation used experimental data for absorption whereas in [109] they calculate unperturbed absorption by assuming parabolic bands and using the square root law. Additionally, the plot from [109] in Fig. 5.3(b) is specifically for electron concentration in n-type GaAs, whereas in Fig. 5.3(a) we assume injected electrons and holes (with N=P), which will influence the calculations, particularly for free-carrier absorption. In both cases however, it's worth noting that the net index shift is indeed positive in GaAs for low carrier concentrations at this wavelength (1030 nm = 1.204 eV). This is something which is not observed in InP, either in theory or practice,

for the common InP laser wavelengths of 1.3 µm and 1.55 µm. Fig. 5.4 shows a similar plot of Δn versus carrier density in InP from [109]. This figure shows the absolute value of Δn to accomodate a log scale, but it is specified in the text that Δn is indeed negative across the whole carrier density range.

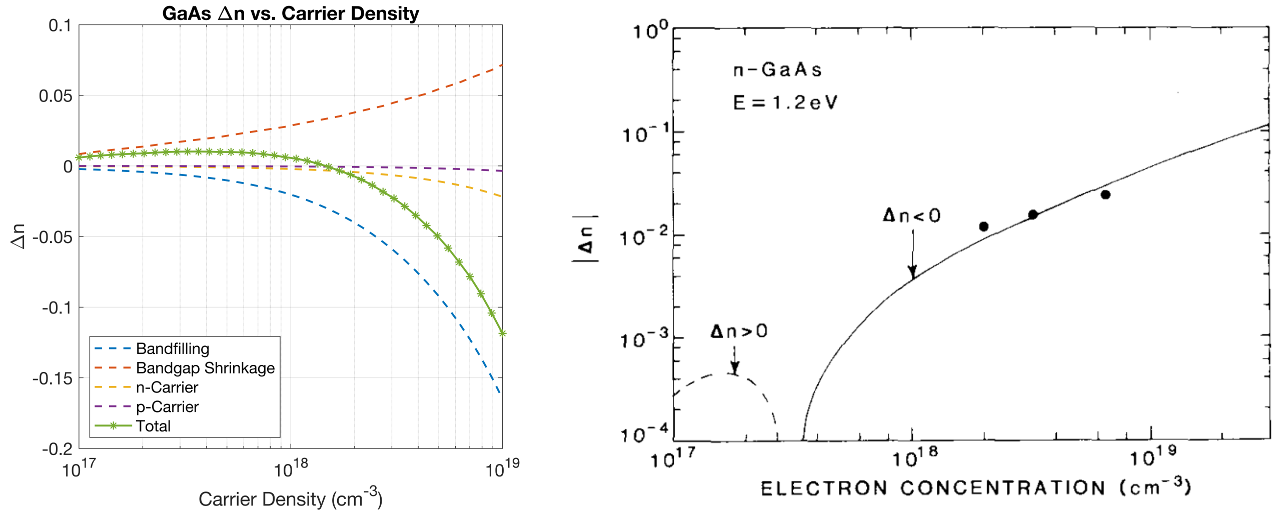

Figure 5.3: (a) Calculation of change in refractive index versus carrier density for GaAs and (b) similar data calculated in [109] for n-type GaAs.

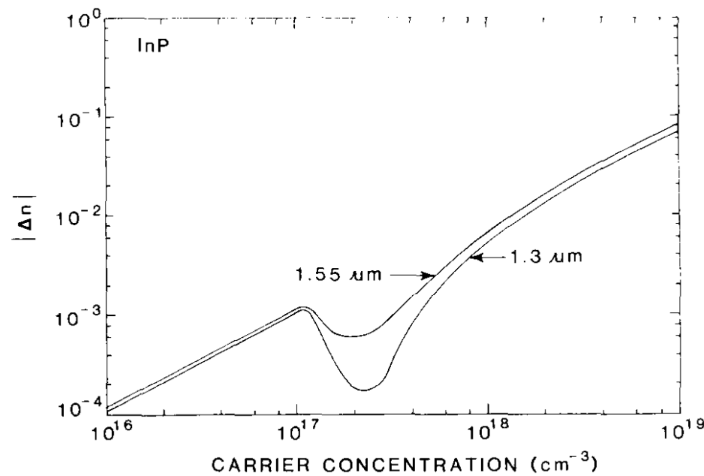

Figure 5.4: Calculated Δn versus carrier density in InP at two different wavelengths from [109].

5.1.2 Electric Field Effects

In addition to the influence of free-carriers, an electric field in a semiconductor also induces a shift in the wavelength. The two primary field related effects are the linear electrooptic effect (LEO) and electrorefractive effect (ER) [110, 113].

Linear Electrooptic Effect

The linear electrooptic effect, also known as Pockel's effect, occurs in GaAs crystals as a result of the lack of inversion symmetry. For an electric field oriented in the crystal's [001] direction, the change in index is given by [110],

$$n_{x'} = n_0 - \frac{n_0^3}{2} r_{41} E_z \tag{5.12}$$

$$n_{y'} = n_0 + \frac{n_0^3}{2} r_{41} E_z \tag{5.13}$$

where E_z is the electric field component in the z-direction (or [001] crystal axis, in this case), n_0 is the index in the absence of electric field, r_{41} is the LEO coefficient, the subscript x' indicates the [110] direction and y' represents the [$\bar{1}$10] direction. The direction of the index change due to the LEO effect is therefore dependent on the orientation of the waveguides relative to the crystal axes.

Electrorefractive Effect

The elcrorefractive effect, also known as Franz-Keldysh effect, occurs due to tilting of the band edges in the presence of an applied electric field. Tilting of the band edges increases the overlap of electrons in the conduction band and holes in the valence band thus increasing the probability of tunneling across the gap. This leads to a change in the overall absorption, which in turn results in a shift in the index of refraction. For a constant

wavelength it has been found that the change in index has a quadratic dependence on electric field strength [110, 113]. Based on a fit to empirical data for GaAs, the index shift is calculated with

$$\Delta n(ER) = 3.45 \times 10^{-16} \exp\left(\frac{3}{\lambda^3}\right) \boldsymbol{E}^2 \tag{5.14}$$

where λ is wavelength in microns, and $\boldsymbol{E}$ is electric field strength in V/cm. For the ER effect, Δn is always positive regardless of crystal orientation.

In terms of refractive index tuning, the electric field related effects are typically much smaller than carrier injection. Fig. 5.5 shows a plot from [110] showing Δn as a function of applied reverse bias for an AlGaAs/GaAs/AlGaAs heterostructure waveguide. Here the maximum index change achieved under reverse bias is $1e^{-3}$ at -6 V at a wavelength of 1.06 µm, which is more than an order of magnitude smaller than what can be achieved with carrier injection in Fig. 5.3. Based on the equation for wavelength tuning in a DBR

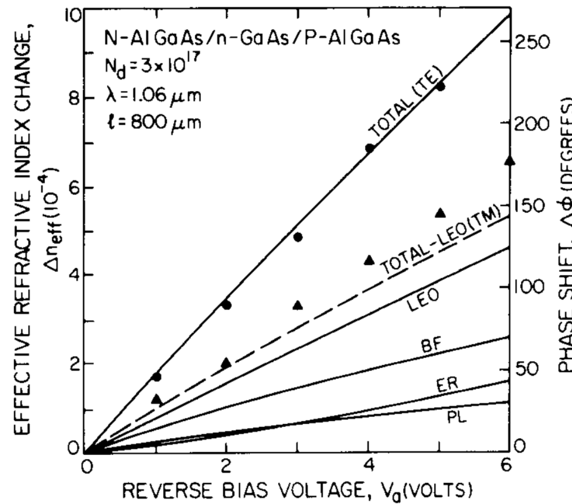

Figure 5.5: Δn versus reverse bias in the AlGaAs/GaAs/AlGaAs heterostructure described in [110].

mirror,

$$\frac{\Delta\lambda}{\lambda} = \frac{\Delta\bar{n}_{DBR}}{\bar{n}_{DBR}} \tag{5.15}$$

an index shift of $1e^{-3}$ would correspond to $\Delta\lambda \approx 0.3\ nm$, however a wavelength shift of at least several nm is typically desirable in tunable lasers. For this reason, carrier injection techniques are typically preferred for wavelength tuning. Electric field based effects are more commonly used for phase modulation, which is the application in [110], because the response time is typically higher, and power consumption is very low in reverse bias. Residual amplitude modulation (RAM) in phase modulators is also lower for reverse biased devices [114, 115]. For current injected devices, there is of course still some influence from electric field effects because the device is biased. But for typical diodes, a normal forward operating voltage is in the range of 1-2 V, so the field induced refractive index is change is much smaller than the influence of carriers.

5.1.3 Thermorefractive Effect

Temperature is another factor that influences the refractive index in semiconductors. The thermal dependence is typically linear. For GaAs, the slope of the linear relationship between index and temperture has been measured in [116] as,

$$\left(\frac{dn}{dT}\right)_{GaAs} = (2.67 \pm 0.07) \times 10^{-4}/°C. \tag{5.16}$$

Fig. 5.6 shows a plot from [116] showing the measured shift in index versus temperature for GaAs and AlAs. Thermal tuning offers the widest practical tuning range, and for real devices is typically accomplished with micro-heaters placed above the tuning section. With the use of micro-heaters, the tuning section does not need to be conductive as in the case of carrier based tuning. Thermal tuning is therefore the most common method

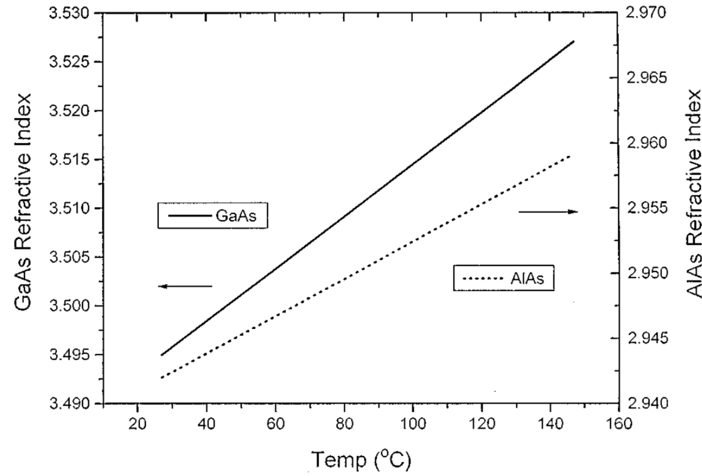

Figure 5.6: Refractive index vs. temperature of GaAs and AlAs at a photon energy of 1.2 eV. Figure adapted from [116].

for SiN based tuning elements with the heaters placed above ring mirrors [83, 117, 118]. However, the major downside to thermal tuning is its slow response time. Tuning speed using micro-heaters is typically on the order of kHz as opposed to many MHz or more for carrier and field based effects.

5.2 Analysis of Tuning in GaAs SGDBR Lasers

Based on the wavelength tuning data from the SGDBR lasers presented in chapter 4, the wavelength clearly red-shifts with increasing current. This can be seen in the tuning map shown in Fig. 5.7. A red-shift (positive $\Delta\lambda$) indicates a positive Δn in the mirror sections during tuning. Based on the theory presented in the previous section, positive Δn should only occur at relatively low carrier concentrations if we consider only carrier based effects. From the curves calculated in Fig. 5.3(a), the maximum positive index shift is less than 0.01 at a relatively low total carrier density of ~5e17, which corresponds to a wavelength shift of approximately 2 nm. With higher carrier concentration, the total index shift should quickly become negative. However the wavelength is only observed to

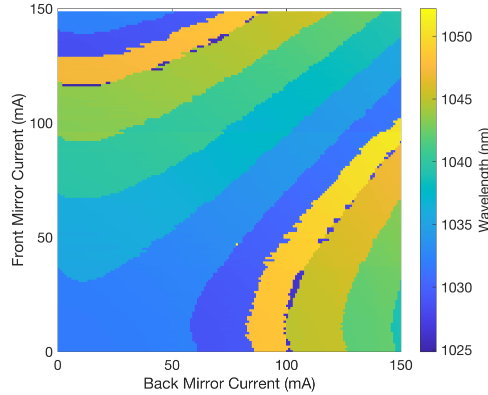

Figure 5.7: Contour map of wavelength versus front and back mirror current in 1030 nm SGDBR laser.

redshift with increasing current, and the total wavelength shift for a single mirror is over 4 nm (refer to Fig. 4.14(b)). This naturally leads one to conclude that the dominant tuning effect in Fig. 5.7 is thermal, which is almost certainly the case, at least for higher current injection levels. However, blue shifting in direct current injected mirrors has been reported for GaAs [102], although the effect is fairly small. Fig. 5.8 shows plots from this paper. The plot on the left is experimental tuning data from two different laser structures showing blueshift first before leveling off and beginning to redshift. In this paper, the authors theorized that oxygen contamination at the regrowth interface contributed to increased Shockley-Read-Hall (SRH) recombination (i.e. decreased SRH lifetime). Higher SRH recombination rates would lead to lower overall carrier density. The plot on the right in Fig. 5.8 shows simulated wavelength change versus current for 3 different SRH lifetimes in the single QW (SQW) structure. When $\tau_{SRH} = 0.5\ ns$, the wavelength never blueshifts at all indicating that by the time the carrier density is high enough to cause a blueshift, self-heating has become the dominant effect. Before drawing too close a comparison between this and our SGDBR results, it's worth pointing out that the laser in this paper had a wavelength of 970 nm, rather than 1030 nm. This is significantly closer to the band edge of GaAs where the bandfilling effect (blueshift) becomes more significant

(refer to Fig. 5.2(b)). To see the effect of SRH lifetime on the tuning performance of our

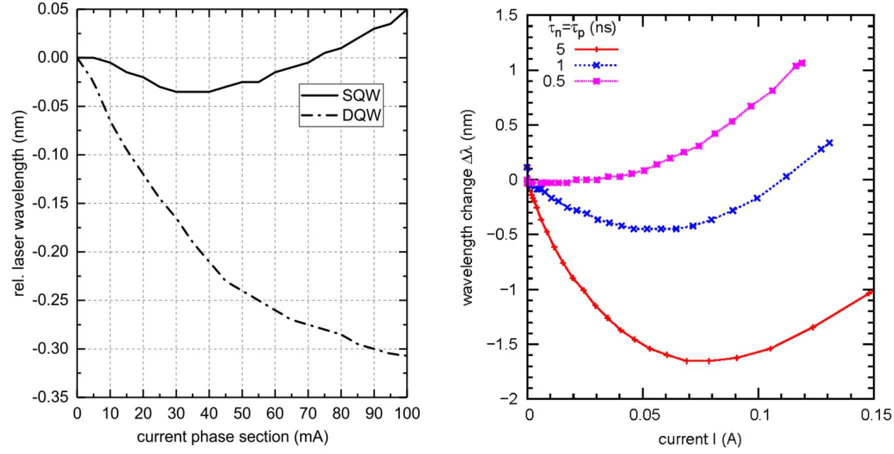

Figure 5.8: Wavelength change versus passive section current: experimental results for two different structures (left), and theory for the SQW structure (right) with varying SRH lifetimes and taking into account self-heating. Figure adapted from [102].

lasers, the passive mirror section was simulated using Ansys Lumerical CHARGE and HEAT. This simulation takes into account SRH recombination, Auger recombination, and spontaneous recombination as well as simulating the effects of self-heating due to current injection. Fig. 5.9 shows the simulated diode IV compared to measurement in the mirror section; the simulation shows slightly faster turn-on but otherwise similar IV behavior. Heat maps for the diode are shown on the right in Fig. 5.9 for two different SRH lifetimes, showing that self-heating is more significant for shorter τ_{SRH}. The Lumerical CHARGE and HEAT simulations calculate the carrier distribution and temperature throughout the entire structure. This can then be imported into Lumerical MODE and used as an index perturbation, based on the model for index vs. carrier concentration in Fig. 5.3(a). In this way, the expected change in effective index as a function of injected current can be simulated for the specific geometry of our device. The results of this simulation are shown in Fig. 5.10 for 4 different SRH lifetimes. Fig. 5.10(a) shows Δn vs current without considering heating and Fig. 5.10(b) includes the effect of self-heating. In the case with self-heating, for $\tau_{SRH} = 0.5\ ns$, the slope of the index

change eventually becomes negative but not until around 80 mA. However, I suspect that these simulations are underestimating the self-heating effects based on the difference in measured and simulated IV curves in Fig. 5.9 and further analysis needs to be performed to verify. The general trend is still relevant though, and it's clear that with shorter τ_{SRH} the carrier density is lower, and self-heating is higher. These together contribute to the overall positive index shift that was observed in our devices regardless of current injection level, and is consistent with the data in [102].

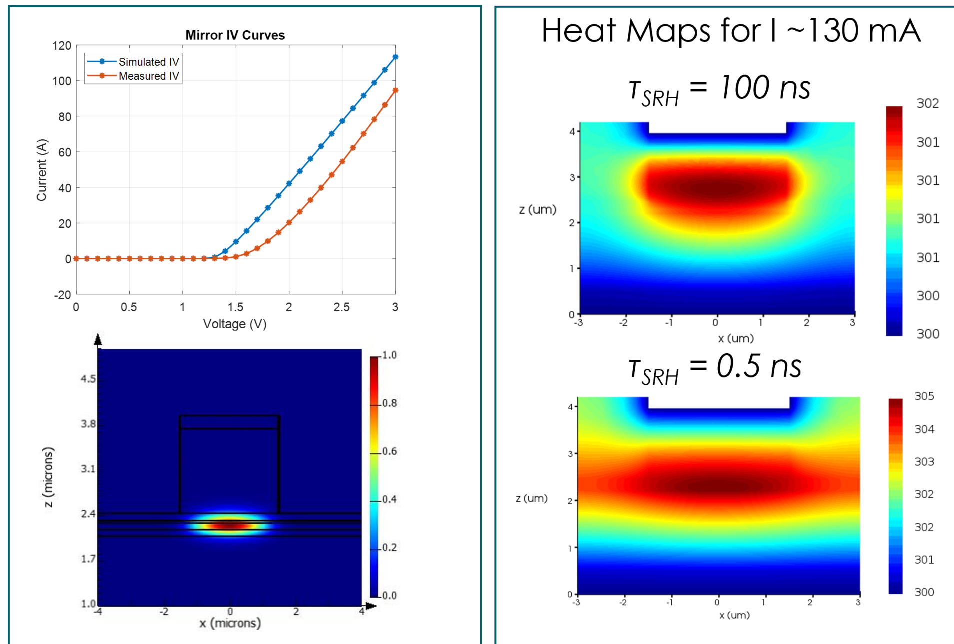

Figure 5.9: (left) Simulated and measured IV curves and optical mode profile in mirror section and (right) simulated heat map at 130 mA for two different SRH lifetimes.

5.3 Time Resolved Photoluminescence on GaAs/AlGaAs Regrowth Samples

Based on the discussion in the previous section, the obvious question is: what can be done to reduce SRH recombination in the waveguide? Oxygen incorporation during

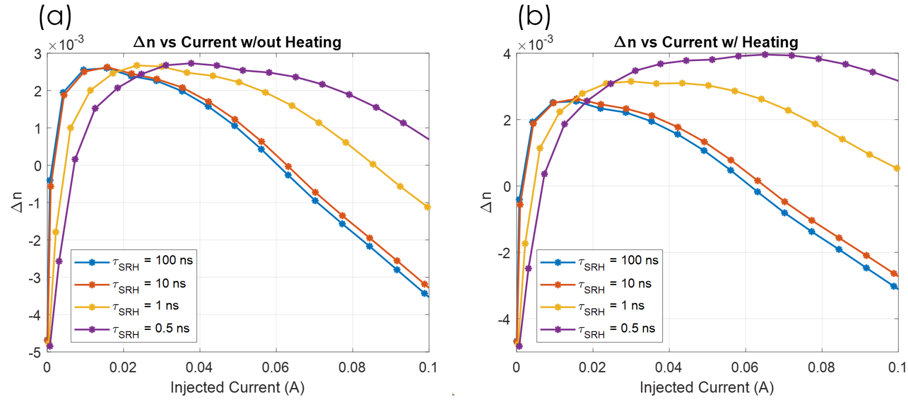

Figure 5.10: Index change versus mirror section current: (a) without self-heating and (b) with self-heating.

growth leads to trap states which act as non-radiative SRH recombination centers. For the regrown epi structure used for these lasers, it is possible that oxygen contaminated the regrowth surface leading to a higher density of these trap states. With our collaborators at Freedom Photonics, we theorized that different methods of surface preparation may have an influence on the level of oxygen incorporation at the regrowth interface. While it is difficult to directly measure a value for τ_{SRH}, the overall effect of carrier recombination can be observed with time-resolved photoluminescence (TRPL) measurements [119]. To test this, multiple samples were prepared with different surface treatments and slightly different regrowth conditions. Fig. 5.11 shows the epitaxial layer structure for these regrowth tests, which includes 980 nm QWs below a 10 nm GaAs cap, and regrown 1350 nm thick AlGaAs and 100 nm thick GaAs. Table 5.1 lists details for the regrowth samples with different surface treatments and regrowth conditions. Every sample was treated with either HF or NH4OH before growth, and the A and B samples also underwent an 800 °C bake. Some of the samples had a SiO_2 hard mask deposited and then removed with BHF, to emulate the fabrication process for real devices, as indicated in the last column of the table. The samples were small pieces diced from a 3 inch GaAs wafer, each piece approximately 1 cm^2. TRPL measurements were performed on each sample

Table 5.1: GaAs/AlGaAs Regrowth Sample Information

Batch	Label	Surface treatment	800 °C bake	Regrowth temp (°C)	Hard mask deposition & removal (BHF)
1	A1	NH4OH	yes	720	no
1	A2	HF	yes	720	no
1	A3	HF	yes	720	no
1	A4	NH4OH	yes	720	yes
1	A5	HF	yes	720	yes
1	A6	HF	yes	720	yes
2	B1	NH4OH	yes	670	no
2	B2	HF	yes	670	no
2	B3	HF	yes	670	no
2	B4	NH4OH	yes	670	yes
2	B5	HF	yes	670	yes
2	B6	HF	yes	670	yes
3	C1	NH4OH	no	670	no
3	C2	HF	no	670	no
3	C3	HF	no	670	no
3	C4	NH4OH	no	670	yes
3	C5	HF	no	670	yes
3	C6	HF	no	670	yes

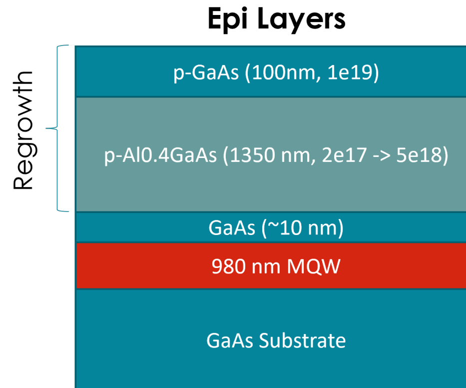

Figure 5.11: Epitaxy for regrowth tests.

after regrowth. The measurement setup used a 730 nm laser for excitation, which is lower energy than the $Al_{0.4}GaAs$ bandgap so it excites carriers only in the GaAs and QW layers. The detector was broadband, but two measurements were performed with different bandpass filters to measure both 870 nm emission from GaAs, and 980 nm emission from the QWs. The 100 nm p-GaAs contact layer was left in place for most of the samples, which means that some of the excitation occurs in that layer, and not at the regrowth interface which is the region of interest. A quick calculation based on reported absorption values predicts that about 80% of the 730 nm excitation passes through the top layer, so the TRPL data is still dominated by recombination below the interface. However, the p-GaAs layer was etched away for 3 of the samples, A1, B1, and C1, and the observed decay was slower for those 3, although not by a large margin. All the measurements are shown in Fig. 5.12. For 870 nm emission in Figs. 5.12(a-c), there is no immediately obvious difference between the 6 samples, except that the samples without p-GaAs show slightly slower decay. For the 980 nm measurement, however, some of the samples clearly exhibit much slower decay. In all cases of slower decay, the sample was treated with NH4OH, rather than HF, before regrowth. To more readily see the decay rate, the 1/e lifetime (i.e. time it takes to decay to 37% of the peak) was extracted for

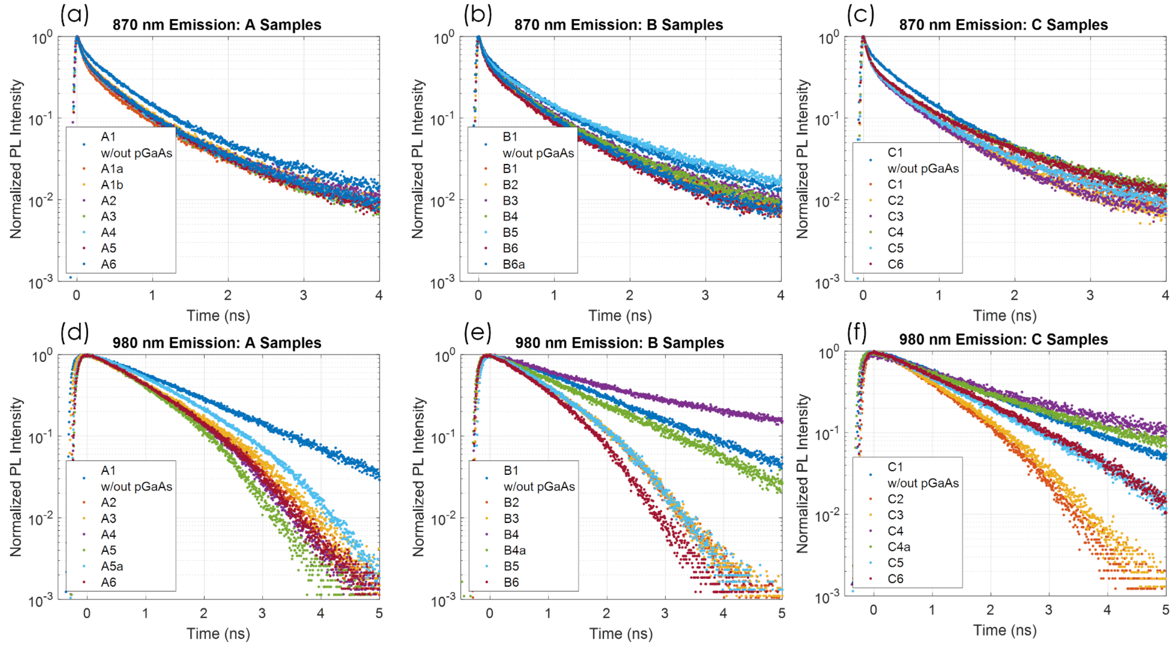

Figure 5.12: 870 nm emission vs time for (a) A samples, (b) B samples and (c) C samples. 980 nm emission vs time for (d) A samples, (e) B samples and (f) C samples.

each curve. This was chosen rather than trying to fit to the curves, because the clear multi-exponential behavior makes fitting challenging. This was also the approach used in [119], so a direct comparison can be made with their reported lifetimes. The 1/e decay time is shown for each sample in Fig. 5.13. Samples 1 and 4 (for A, B, and C) were all treated with NH4OH, and these are the samples with longest decay in Fig. 5.13(a), with the exception of A4. In Fig. 5.13(b) the trend is less clear, but the A and B samples tend to have slightly longer decay than the C samples. Referring back to Table 5.1, all the A and B samples had an 800 °C bake, whereas the C samples did not. For reference, the samples in [119] which consisted of exposed GaAs that was treated with a nitridation process to prevent oxidation, displayed very similar 1/e lifetimes at 870 nm to those shown in Fig. 5.13(b). These results are obviously not a direct measurement of SRH lifetimes, however it is instructive to note that the carrier lifetime is clearly longer for the samples that were treated with NH4OH, rather than BHF. Furthermore, there

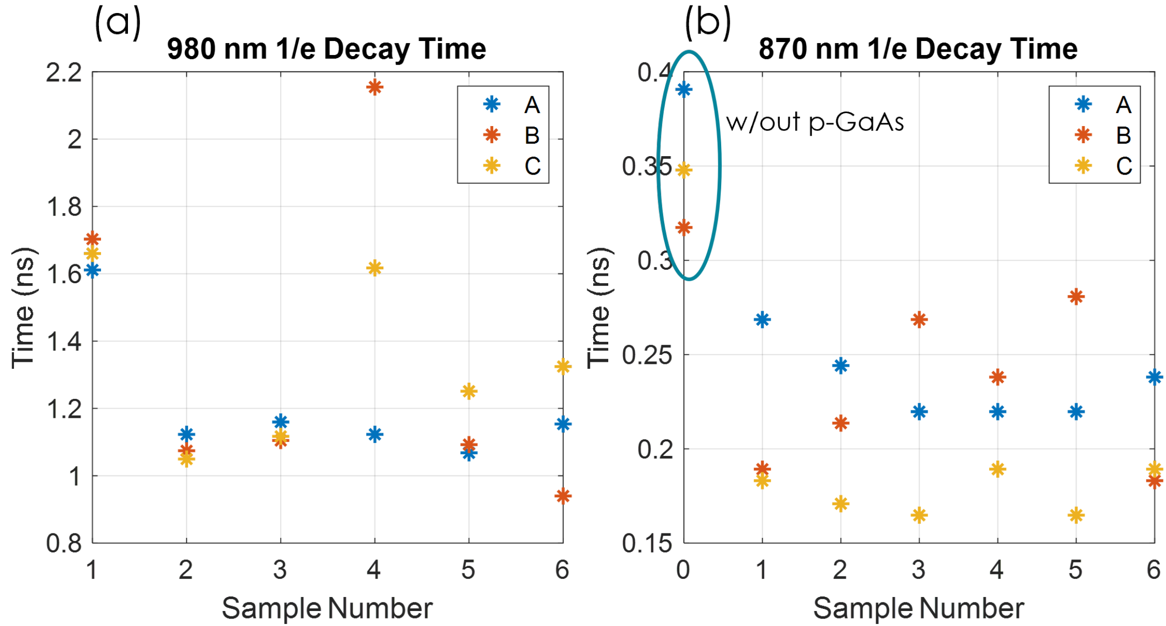

Figure 5.13: 1/e lifetime extracted from TRPL measurements for (a) 980 nm emission for QWs and (b) 870 nm emission from GaAs.

appears to be little or no dependence on regrowth temperature, at least between 670 °C and 720 °C. Depositing and removing a hard mask before regrowth also appears to have no significant effect. The SGDBR lasers fabricated in chapter 4 all used BHF in preparation for regrowth, so it is possible that the lifetime could be improved in the future by treatment with NH4OH.

5.4 Summary

This chapter began with an overview of the various physical mechanisms that influence wavelength tuning in GaAs lasers and an analysis of the tuning behavior in our SGDBR lasers. The last section included results from a regrowth experiment to compare carrier lifetimes for samples with different regrowth surface treatments. Meeting the tuning speed metric of >1 MHz will require carrier based tuning, rather than temperature based tuning, and should be the focus of future work. Based on the TRPL

measurements, improved surface treatment with NH4OH prior to regrowth may reduce SRH recombination due to oxygen incorporation, but a full device fabrication would be required to confirm if this sufficiently increases the magnitude of carrier-based tuning. Further changes to the design may also be considered, such as doping the waveguide in the mirror sections, which would simultaneously increase carriers and reduce series resistance (and thus self-heating).

Chapter 6

III-V Lasers on Planar Silicon by MOCVD Heteroepitaxy

A general discussion of III-V on Si integration techniques, including heteroepitaxy, was provided in chapter 2, detailing some of the different approaches that have been employed by various research groups using both MBE and MOCVD growth techniques. This chapter focuses specifically on the demonstration III-V lasers grown on planar Si by MOCVD direct heteroepitaxy. Section 6.1 provides a brief overview of quantum dot active regions, and some of their advantages. Section 6.2 highlights some prior work at UCSB on MOCVD grown InAs/GaAs QDs, both on native GaAs substrates and on Si. Section 6.3 provides an overview of blanket growth on planar silicon by MOCVD - specifically on a nano V-groove patterned Si template. Section 6.4 includes a discussion of process development and fabrication for lasers on Silicon, and section 6.5 presents results from laser testing and characterization.

6.1 Properties of Quantum Dot Active Regions

Quantum dots are three dimensional nano-structures that provide electron confinement in all three dimensions (as opposed to QWs which have only 1 dimension of confinement). The effect of this 3D carrier confinement is a discretization of the allowed energy

levels leading to a delta-function shape for the density of states (DOS) [24,48,74,80,120]. This reduction in DOS leads to some unique properties and advantages of QDs. Fig. 6.1 shows the progression of active regions from bulk, to quantum wells, to quantum dots and the corresponding effect that increased confinement has on the DOS. For self-assembled

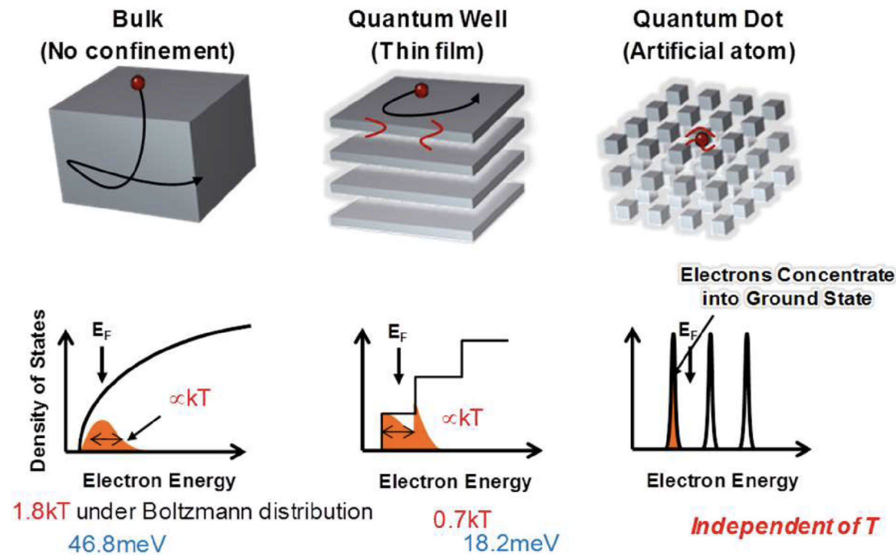

Figure 6.1: Effect that increasing electron confinement has on the density of states. Figure adapted from [74]

QDs, individual dots are not all exactly the same size, rather there is a distribution of inhomogeneous dots with varying size. The variation in size leads to a variation in allowed energy states and transitions for the overall active region, although individual dots retain the characteristic delta-function DOS. For real QD active regions this results in a broadening of the gain spectrum, which can be advantageous for some applications such as broadband wavelength division multiplexing systems.

6.1.1 Low Threshold Current and High Characteristic Temperature

Lower threshold current, and reduced temperature sensitivity are two of the most appealing properties of quantum dot lasers. The lower threshold current leads to lower overall power consumption making QD lasers attractive for energy-efficient optical transceivers. Similarly improved temperature stability reduces the cost associated with actively cooling devices, which becomes quite significant in large data centers, for example. Both the lower threshold and improved thermal performance arise as a result of the reduced density of states in QDs, and were theoretically predicted well before the first demonstration of QD lasing [24, 121, 122].

To reach the lasing threshold condition, population inversion must be maintained in the gain medium. For diode lasers, this is accomplished by pumping carriers into the conduction band via current injection. In the case of QD active regions, discretization of the density of states means there are fewer available energy states in the conduction band, so population inversion can be reached with less current compared to QW or bulk active regions [58, 123]. Strain in the QDs also leads to splitting of the degenerate light-hole and heavy-hole valence bands, which further reduces threshold as a result of selection rules (the same is true for strained QWs [80]). The high characteristic temperature achievable with QDs also results from the delta-function like density of states, which prevents carrier populations from thermally redistributing [24]. Real devices have not achieved truly temperature agnostic operation due largely to the inhomogeneous nature of self-assembled QDs which leads to some overlap of neighboring levels. However, QD lasers have demonstrated very stable operation at high temperature, with CW lasing at temperatures as high as 220 °C [124] and up to 20 Gbps modulation speeds in a silicon interposer operating at 125 °C [125].

6.1.2 Linewidth Enhancement Factor

Reduced linewidth enhancement factor, α is another advantage of QDs. α is defined as the ratio of change in the real part of refractive index n, to the imaginary part of refractive index n_i, with respect to carrier density,

$$\alpha = -\left(\frac{dn}{dN}\right)\left(\frac{dn_i}{dN}\right)^{-1} = -\frac{4\pi}{\lambda}\left(\frac{dn}{dN}\right)\left(\frac{dg}{dN}\right)^{-1}. \tag{6.1}$$

A semiconductor laser's linewidth and its susceptibility to optical feedback are both dependent on the linewidth enhancement factor [80]. Linewidth is one of the limiting factors that determines the maximum error-free modulation bandwidth - lower linewidth allows for faster modulation. Optical isolators are often used to reduce unwanted reflections in photonic integrated circuits, which is necessary for stable operation. However, these are often bulky and expensive. For QD active regions, optical isolators are often unnecessary due to their reduced sensitivity to optical feedback. Theoretical calculations predict that the linewidth enhancement factor could vanish completely for QDs, due to the symmetric density of states [24, 126]. In reality, inhomogeneous broadening leads to non-zero values for α. However, α factors as low as 0.1 have been demonstrated [127] for QDs, whereas typical values for QWs are around 4 to 6 [80].

6.1.3 Tolerance to Growth Defects

Another particularly attractive property of QDs is their reduced sensitivity to growth defects, specifically threading dislocations (TDs). As discussed in chapter 2, TDs tend to propagate vertically through the epitaxial layers and are especially problematic in the case of heteroepitaxial growth due to the significant lattice mismatch between III-V materials and Si [86]. While the use of dislocation filters and thermal cycle annealing (TCA) does

significantly reduce TD density, some TDs do inevitably propagate into the device layers. A threading dislocation in the active region creates a non-radiative recombination center in the form of a trap state - an energy level somewhere between the conduction and valence bands. In quantum wells, electrons are confined in only one dimension and can diffuse laterally before recombining, so a localized trap state can affect recombination of carriers in some radius. For quantum dots, however, 3D electron confinement means that the presence of a trap state will only affect the specific QD where the TD terminated, leaving the surrounding QDs essentially unaffected.

6.2 MOCVD Grown InAs/GaAs Quantum Dots

Indium arsenide (InAs) QDs in a GaAs matrix are generally considered the most mature. The earliest demonstrations of lasers with QD active regions, and many of the commercially available QD lasers [24,128,129] have traditionally been grown with molecular beam epitaxy (MBE). And indeed these have demonstrated many of the promised benefits of QDs described in the previous section [24,48,58,124,125]. However, higher growth rates and the fact that MOCVD doesn't require high vacuum makes it more economical than MBE and thus generally preferred for high-volume industrial needs. Significant efforts have, therefore, been undertaken to develop MOCVD-grown QDs for lasers and other applications. This development has resulted in multiple publications and another PhD thesis from UCSB [75,87,130,131], some of which is highlighted in this section.

Self-assembled QDs are grown using the Stranski-Krastanov growth method. In the case of InAs/GaAs QDs, this technique involves growing a thin 2D "wetting layer" of InAs; typically only a few monolayers. At some critical thickness, the highly strained InAs begins to relax and gives way to 3D growth forming InAs "islands", i.e. quantum dots,

on the surface. After the initial formation of 3D QDs, there is only a very narrow window of growth before dislocations begin to form due to the high strain. One of the primary challenges in demonstrating QDs by MOCVD is controlling dot size and uniformity due to the complex growth dynamics. Another challenge to realizing QD lasers relates to growth of the cladding material. AlGaAs claddings are common for GaAs based lasers, however these typically require growth temperatures around 700 °C in MOCVD systems. Such high temperatures would alter any previously grown QD layers resulting in a strong blueshift in the PL spectrum, so AlGaAs is not preferred, at least for the upper cladding. Indium gallium phosphide (InGaP) is an alternative material that can serve as cladding for GaAs lasers, and can be grown at lower temperature (typically around 500 °C). However InGaP growth tends to suffer from phase separation on GaAs, particularly for the thick layers required for cladding. These issues have been addressed in previous work at UCSB [75, 87, 130, 131]. The details of that development are not presented here as it is not the main focus of this thesis, however some key results are highlighted below.

Fig. 6.2 shows LI characteristics for MOCVD grown QD lasers on native GaAs substrates with InGaP cladding layers [131]. These devices demonstrate high CW output powers up to 200 mW from a single facet, and low threshold current. CW lasing is also demonstrated at temperatures up to 90 °C. Similar lasers have undergone aging tests with extrapolated lifetimes of up to five million hours [75]. MOCVD grown QDs on silicon were also developed for the demonstration of lasers on silicon. Fig. 6.3 shows a schematic of the epi layers for InAs/GaAs QDs grown on a GaAs on V-Groove Si (GoVS) template. AFM scans of the surface after growing 8 layers demonstrates QDs with a dot density of $\sim 5 \times 10^{10}\ cm^2$ [85]. A PL measurement of identical QDs grown on GaAs and on GoVS (samples were co-loaded to ensure identical growth conditions) shows comparable PL in terms of intensity, wavelength, and FWHM on both samples. This demonstrates that the GoVS template provides a high quality surface for QD growth [130].

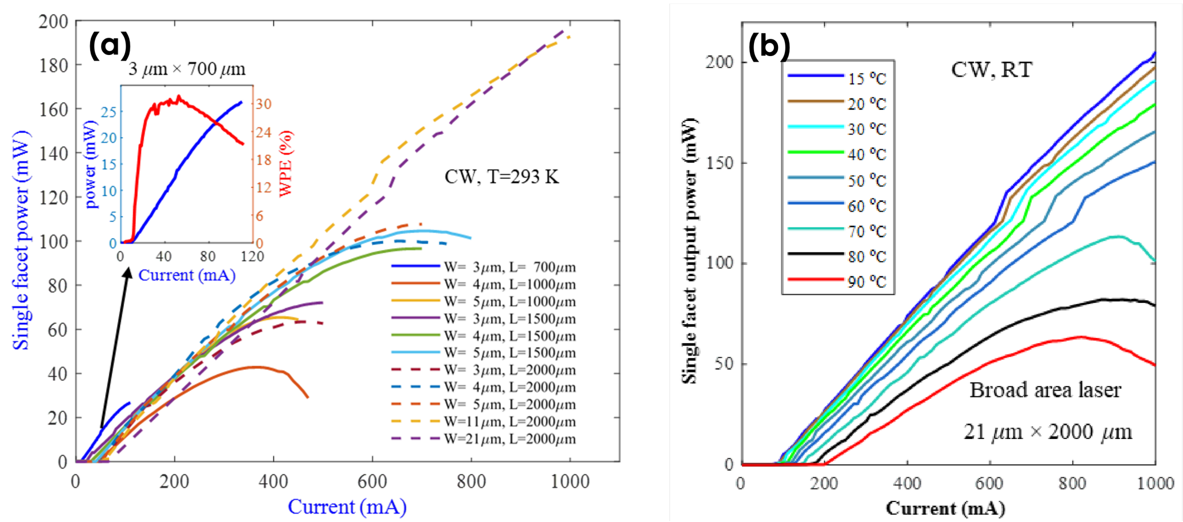

Figure 6.2: (a) MOCVD grown QD lasers on native GaAs with varying ridge widths and (b) broad area laser LI characteristics with varying temperature. Figures adapted from [87].

6.3 Gallium Arsenide Growth on Planar Silicon

6.3.1 GaAs on V-Groove Silicon Templates

The use of nano v-groove patterned Si for heteroepitaxial growth has been shown to effectively avoid the generation of anti-phase boundaries (APBs) in the III-V material [84,85,130]. The process of forming the V-groove structure, as described in [85], starts by first etching 70 nm trenches, aligned to the [110] direction, into a SiO_2 mask on the surface of an on-axis Si (001) sample, leaving 60 nm wide stripes of SiO_2 between openings. The V-grooves are then formed using a 45% dilute potassium hydroxide (KOH) solution which anisotropically etches silicon to leave the $\langle 111 \rangle$ surface exposed. After KOH etching, the sample is dipped in a 10% hydrochloric acid (HCl) solution for 60 s to remove residuals, and then the oxide mask was removed with HF acid. APBs occur as a result of the polarity mismatch between III-V materials and silicon. By creating V-grooves on the silicon surface, the initial III-V growth takes place on the Si (111) plane, which contains

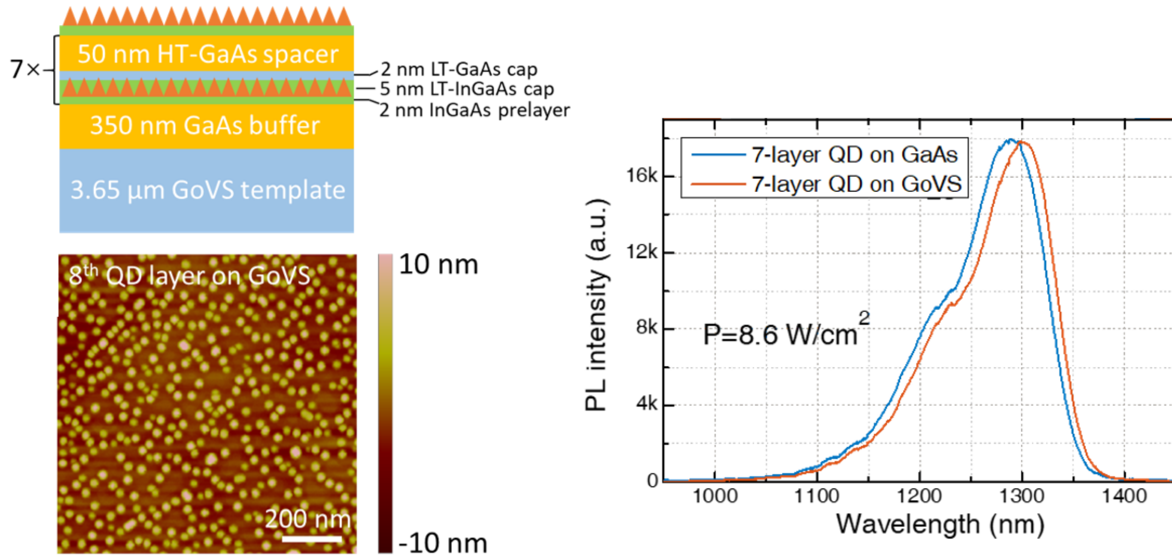

Figure 6.3: InAs/GaAs QD growth development on GoVS template showing (left) layer schematic and AFM scan of QD surface with extracted dot density of $\sim 5 \times 10^{10}\ cm^2$ and (right) PL emission comparing QDs on GoVS and native GaAs with emission peak near 1.3 µm. Figure adapted from [85].

the necessary double atomic steps to reduce the occurrence of APBs while still using a CMOS compatible Si (001) substrate. Another advantage of growing on nano-patterned Si is aspect ratio trapping (ART), where defects are encouraged to propagate laterally rather than vertically during the initial growth [86].

While the use of V-grooves reduces the occurence of APBs, other defects, specifically threading dislocations (TDs), still pose an issue due to the significant lattice mismatch. In order to eliminate TDs, the full GaAs on V-groove Si (GoVS) template consists of a GaAs buffer grown on the patterned silicon substrate, followed by thermal cycle annealing (TCA) and the growth of strained layer superlattices (SLSs) which act as dislocation filters. Fig. 6.4 (adapted from [85]) shows the details of the GoVS template with cross section SEM images highlighting the elimination of defects in the buffer, resulting in low total defect density in the device layers. This GoVS template is used as the starting point for the laser epitaxy demonstrated later.

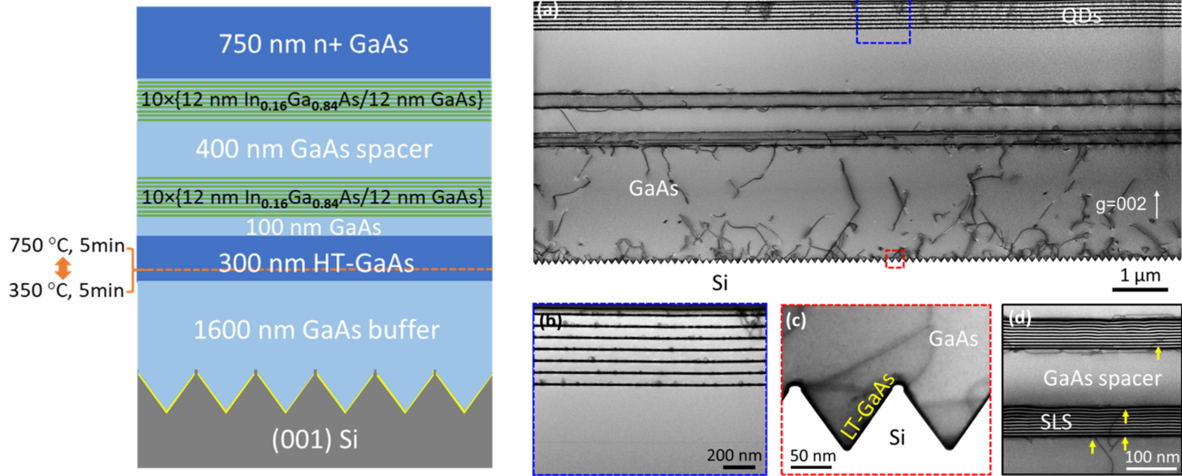

Figure 6.4: GoVS template and growth results showing annihilation of APBs and threading dislocations in the buffer layer. Figure adapted from [85].

6.3.2 Laser Epitaxy

The GoVS template was used to grow the QD laser structure shown in Fig. 6.5(a). The device epi layer stack consists of a GaAs n-contact layer, n-type $Al_{0.4}GaAs$ lower cladding, 5 layers of InAs/GaAs QDs embedded in a GaAs waveguide layer, p-type InGaP upper cladding (lattice matched to GaAs), and GaAs p-contact layer. AlGaAs was chosen for the lower cladding as it is generally easier to grow on GaAs than InGaP. If the InGaP composition is not perfectly matched to GaAs then stress in the film can lead to defects and surface roughness, especially for the thick film necessary to create the cladding layer [87]. Obtaining a high quality surface is especially important for the lower cladding since the active region is grown on top and any defects will negatively influence QD growth. AlGaAs of any composition is lattice matched to GaAs, so slight variation in the composition during growth does not affect film quality, hence the choice of AlGaAs for the lower cladding. However, the high temperature required for AlGaAs growth can influence existing QDs and shift the PL peak. Surface quality is less critical for the upper cladding, and InGaP can be grown at lower temperature (∼550 °C), so this

was used for the upper cladding. Suppressing InGaP phase separation during MOCVD growth is a significant challenge and is addressed in [87]. In the case of growth on planar Si, no phase separation is observed in the InGaP cladding. AlGaAs with 40% Al and lattice matched InGaP have similar bandgaps and refractive indices, so this layer stack is still more or less symmetrical in terms of optical confinement. Fig. 6.5(b) shows the PL spectrum for the 5-layer QD structure demonstrating a PL peak near 1300 nm. This epitaxial structure is used to fabricate the Fabry Perot lasers on Si discussed in the next section.

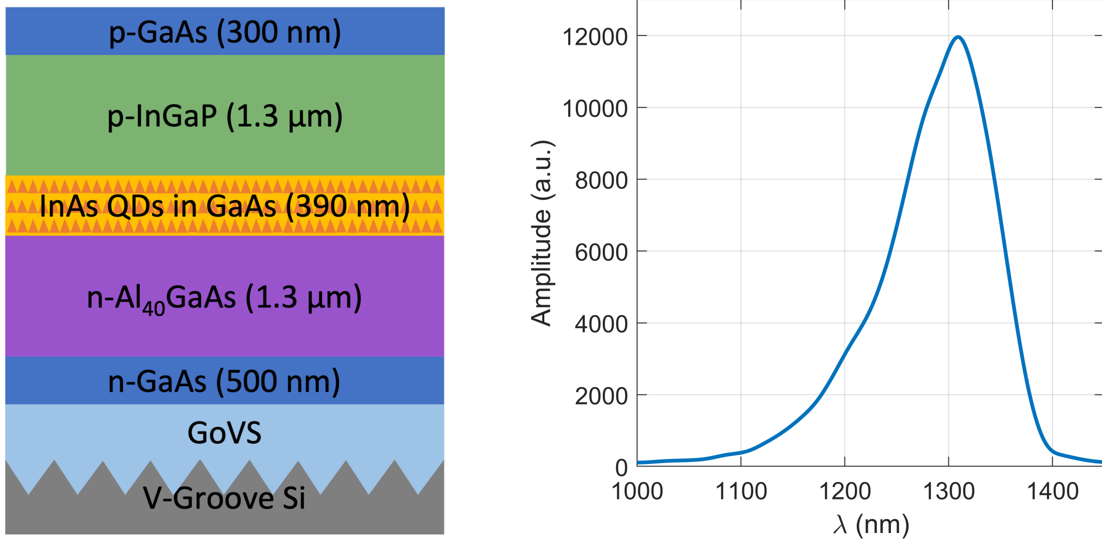

Figure 6.5: (a) QD laser epitaxial layers grown by MOCVD on GoVS template, and (b) measured QD PL spectrum.

6.4 Laser Fabrication

6.4.1 InGaP Dry Etch Recipe Development

The epitaxial layer structure for both the lasers on planar Si and SAH devices contains InGaP cladding, and in the case of the planar Si devices both InGaP and AlGaAs.

Typical InGaP dry etch recipes (based on InP etches) are performed using Cl_2/N_2 gas chemistry with substrate temperatures around 200 °C [132, 133]. However, this high temperature is not suitable for etching GaAs/AlGaAs materials and would lead to significant undercutting, particularly in the thick lower AlGaAs cladding layer used for the planar Si devices. Rather conveniently however, around the time of this work, a new Oxford ICP Etcher (PlasmaPro 100 Cobra) was installed in the UCSB nanofab, and one of its advertised capabilities was low temperature etching of InP and related materials by adding CH_4 to the gas mixture. A customized recipe was developed to reliably etch InGaP at low temperature while also etching AlGaAs and GaAs with reasonable etch rate and sidewall quality. Table 6.1 shows 5 different recipe variations that were tried before finally selecting the 5th one as the best overall. Fig. 6.6 is a collage of SEM images from each etch test showing that recipe 5 results in the best sidewall quality in terms of both verticality and surface roughness, while still having a reasonable etch rate of 0.4 µm/min. I make no claim that this is the best InGaP etching recipe that can be obtained with the Oxford ICP, however it worked reliably for this epitaxy and was used for the remainder of the device fabrications.

Table 6.1: InGaP Dry Etch Recipes

Recipe	Gas Flow	Temperature (°C)	Pressure (mTorr)	ICP Power (W)	Etch Rate (µm/min)
1	$Cl_2/CH_4/H_2$ (18/10/15)	60	3.0	800	0.22
2	$Cl_2/CH_4/H_2$ (18/10/15)	60	3.0	800	0.22
3	$Cl_2/CH_4/H_2/Ar$ (15/10/15/10)	20	2.0	800	0.4
4	$Cl_2/CH_4/H_2/Ar$ (15/10/15/10)	20	3.0	1000	0.4
5	**$Cl_2/CH_4/H_2/Ar$ (18/10/15/5)**	**20**	**2.0**	**800**	**0.4**

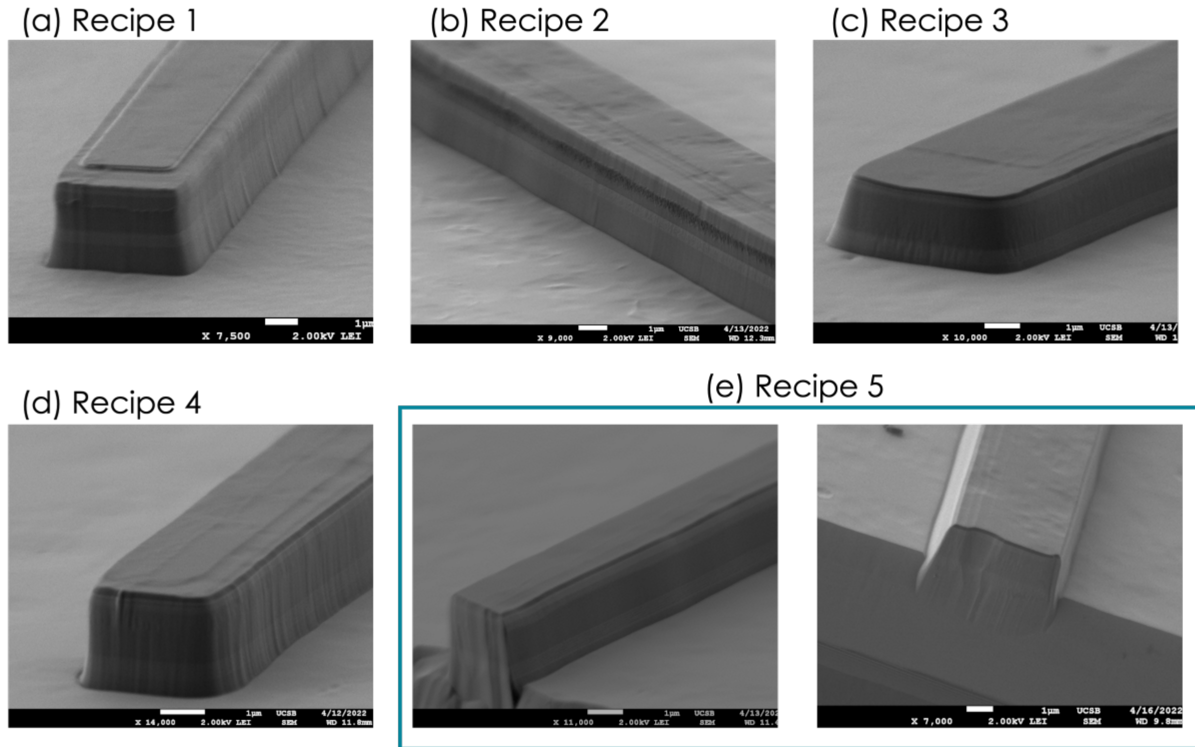

Figure 6.6: (a-e) InGaP dry etch recipe waveguide etching results from recipes 1-5 showing that recipe 5 (e) has the lowest roughness and most vertical sidewalls.

6.4.2 Device Fabrication

Fig. 6.7 shows the process flow for fabrication of Fabry Perot ridge lasers on the planar GoVS template using the epitaxy that was described in the previous section. Fabrication starts with electron beam deposition of Ti/Pt/Au for the p-contact. A SiN/SiO_2 dielectric stack is then deposited as a hard mask for the waveguide etch and the ridges are formed using the ICP dry etch recipe described above. Ridge widths on the mask varied from 3 µm to 20 µm. Since the lower cladding was AlGaAs and we had no selective etch to stop on the GaAs below, the etch was precisely timed to stop just after reaching the n-GaAs contact layer. The etch depth was verified with SEM imaging. After ridge etching, Ni/AuGe/Ni/Au contacts were deposited on the n-GaAs contact layer. The sample was then passivated with 5 nm of aluminum oxide (AlO) via atomic

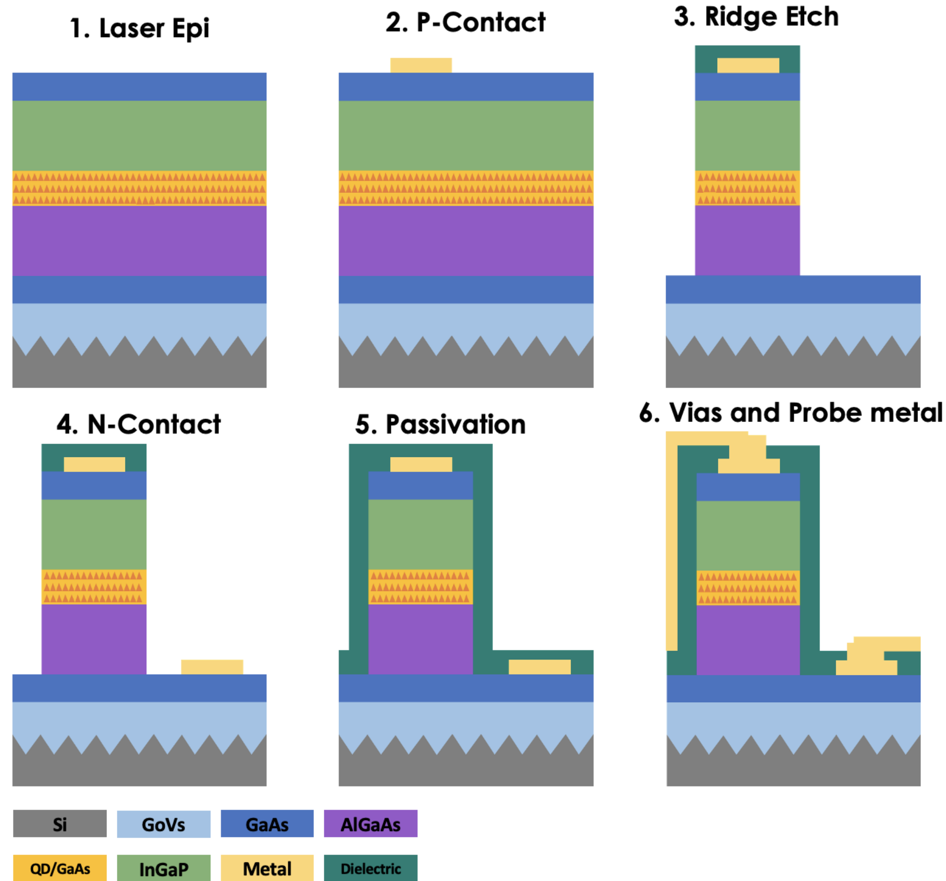

Figure 6.7: Summary of fabrication steps for Fabry-Perot ridge lasers using GoVS template on planar silicon.

layer deposition (ALD) followed by a SiN/SiO_2 stack deposited with PECVD. Vias were opened in the dielectric to reach the n- and p-contacts, and Ti/Au was deposited for the probe metal. The silicon substrate was then thinned to approximately 150 µm, and the sample was cleaved to form Fabry-Perot (FP) lasers of varying lengths.

Thermal cracks in GaAs are a known issue for blanket growth on Si [92]. These cracks naturally align to the GaAs crystal axes and to maximize yield, the waveguides should be aligned with a crack, and thus the crystal axis. The sample was inspected to find the regions with lowest crack density and the Heidelberg maskless aligner (MLA) in the UCSB cleanroom was used to manually align the first layer with the cracks. Fig. 6.8(c)

shows a microscope image after deposition of the p-contact layer, highlighting alignment to the cracks. Fig. 6.8(a) shows a tilted SEM image of the waveguide just after etching, showing reasonably low sidewall roughness using the recipe developed earlier. Fig. 6.8(b) shows a cross-section of a cleaved facet device after fabrication. The waveguide sidewalls are close to vertical and the n- and p-contact metals are clearly visible and contacted to the n- and p-GaAs layers respectively. Fig. 6.8(d) is a top-view microscope image of one of the laser bars after fabrication and cleaving.

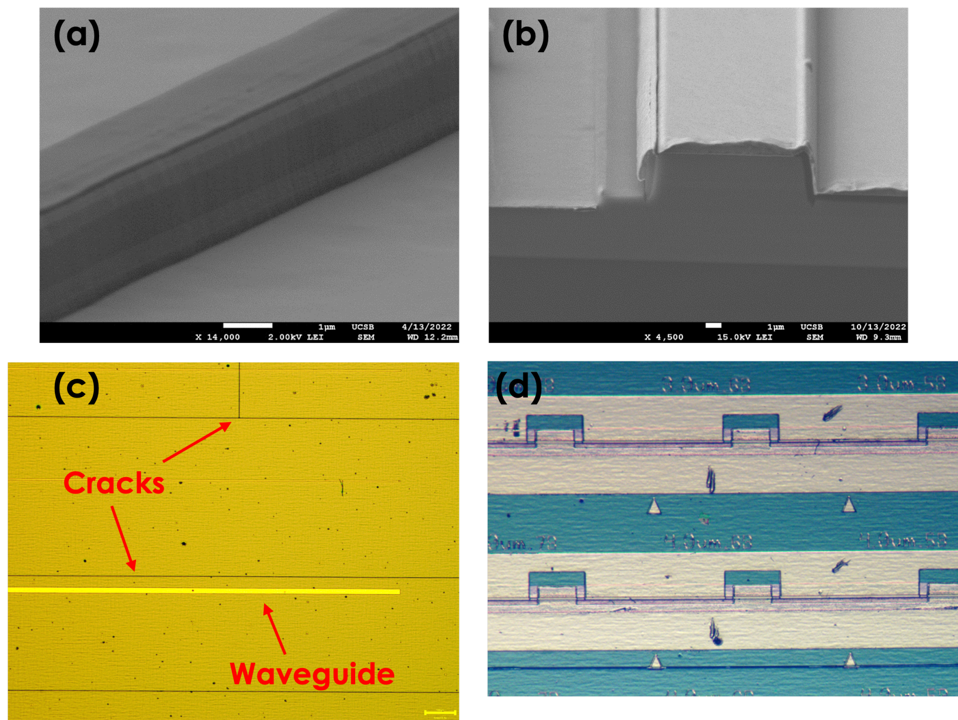

Figure 6.8: (a) Tilted SEM image of waveguide etch, (b) cross-section SEM of cleaved facet laser after fabrication and (c) top-view microscope after p-contact deposition showing relative alignment to thermal cracks, and (d) microscope image of fabricated lasers.

6.5 Laser Testing and Characterization

Following fabrication, the planar silicon sample was cleaved into laser bars for testing. Fig. 6.9(a) shows LIV characteristics for a 4 µm wide and 1850 µm long laser at room temperature under both pulsed and CW current operation. This laser demonstrates a CW threshold current of 46.8 mA (354 A/cm^2 threshold current density), and up to 16 mW CW power from a single facet. Under pulsed current operation, the single facet output power is greater than 25 mW and the threshold current is 38 mA (289 A/cm^2 threshold current density). Fig. 6.9(b) illustrates the room temperature lasing characteristic for a 20 µm wide and 1600 µm long broad area laser under pulsed current operation, demonstrating up to 100 mW output power from a single facet.

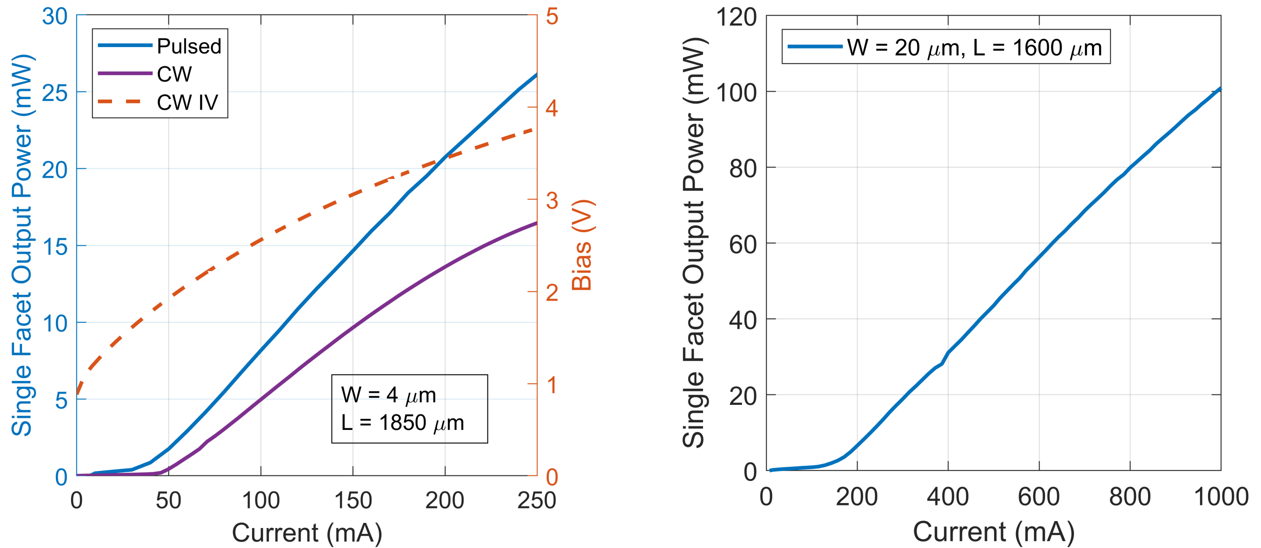

Figure 6.9: LIV characterstic for (a) 4 µm wide, 1850 µm long ridge laser under both CW and pulsed current operation and (b) LI characteristic under pulsed current for a 20 µm wide, 1600 µm long broad area laser.

The diode series resistance for these devices was higher than expected. In Fig. 6.9(a) the bias is close to 4 V to reach 250 mA, which is nearly 1 W of power dissipation. The high resistance leads to self-heating under CW operation, which explains the significant difference in threshold current and efficiency for the pulsed versus CW LI curves. How-

ever, we have attributed this to a fabrication issue in forming the n-contacts and not an issue with the epitaxial layers. It is not shown here, but the n-contact metal did not properly form ohmic contacts, and the resulting contact resistance was rather high. Several additional annealing steps were performed after fabrication and cleaving which significantly improved the overall series resistance. Fig. 6.9(a) represents one of the improved IV curves. Further annealing only ended up degrading the QD gain properties and light emission was significantly reduced. In spite of the high resistance, both the broad area and narrow ridge lasers exhibit reasonable output powers and the narrow ridge device still delivers greater than 15 mW out of each facet under CW operation.

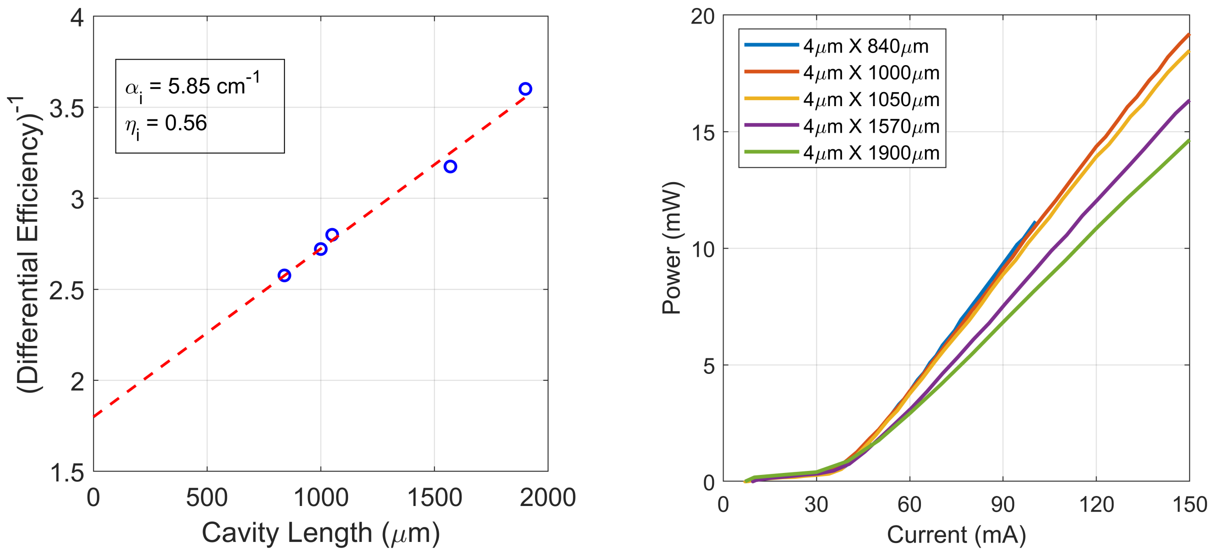

Figure 6.10: (a) Inverse differential efficiency versus cavity length to extract internal loss and injection efficiency for 4 µm wide lasers and (b) pulsed current LI curves associated with the data points in (a).

Additional pulsed measurements were performed with 4 µm wide lasers of varying lengths to extract internal loss and injection efficiency. The results are shown in Fig. 6.10(a), which plots inverse differential efficiency versus cavity length to extract internal loss, α_i, of 5.85 cm^{-1} and injection efficiency, η_i, of 0.56. Fig. 6.10(b) shows the five LI curves corresponding to the data points in Fig. 6.10(a). This value for injection

efficiency is quite close to the 60% that has been reported for 3 µm wide MOCVD grown QD lasers on native GaAs [131]. Injection efficiency as high as 87% has been reported for MBE grown, 6 µm wide QD ridge lasers on Si [134] and up to 90% for MBE grown QD broad area lasers on native GaAs [135]. It is worth noting, however, that in both of these publications injection efficiency varies considerably with laser geometry. In [134], 3 µm wide lasers have η_i in the 60-75% range and in [135], lasers with thicker active region have η_i around 70%. Ideally, it is better to use broad area lasers (e.g. 20 µm or wider) to extract internal loss and efficiency as it minimizes the influence of effects such as sidewall recombination and excess scattering loss from sidewall roughness [80]. However, the sample fabricated here did not yield a sufficient number of broad area lasers for this measurement due to the presence of cracks in the GaAs. So, while it appears that MOCVD grown QD lasers may have lower injection efficiency, it's likely that the extracted value for η_i would be higher if the measurements were performed on wider ridge lasers.

The laser's temperature dependence was also measured for a 4 µm wide ridge, as shown in Fig. 6.11. These lasers demonstrated CW lasing at up to 60 °C in spite of the high series resistance. The same device was tested with pulsed current at varying temperature in Fig. 6.11(b). With current pulsing to mitigate the effects of self heating, lasing is demonstrated at up to 80 °C which was the maximum temperature achievable with this setup. Higher temperature pulsed current operation could likely have been demonstrated with a different thermoelectric cooler (TEC).

The lasing spectrum was also measured by coupling light from one of the 4 µm wide ridge lasers to a lensed optical fiber connected to the optical spectrum analyzer (OSA). Fig. 6.12 shows lasing spectra at two different current injection levels - just above lasing threshold at $I = 1.3 \cdot I_{th}$, and high current injection at $I = 5 \cdot I_{th}$. The fundamental mode peaks at a wavelength around 1280 nm in Fig. 6.12(a). The broad gain spectrum

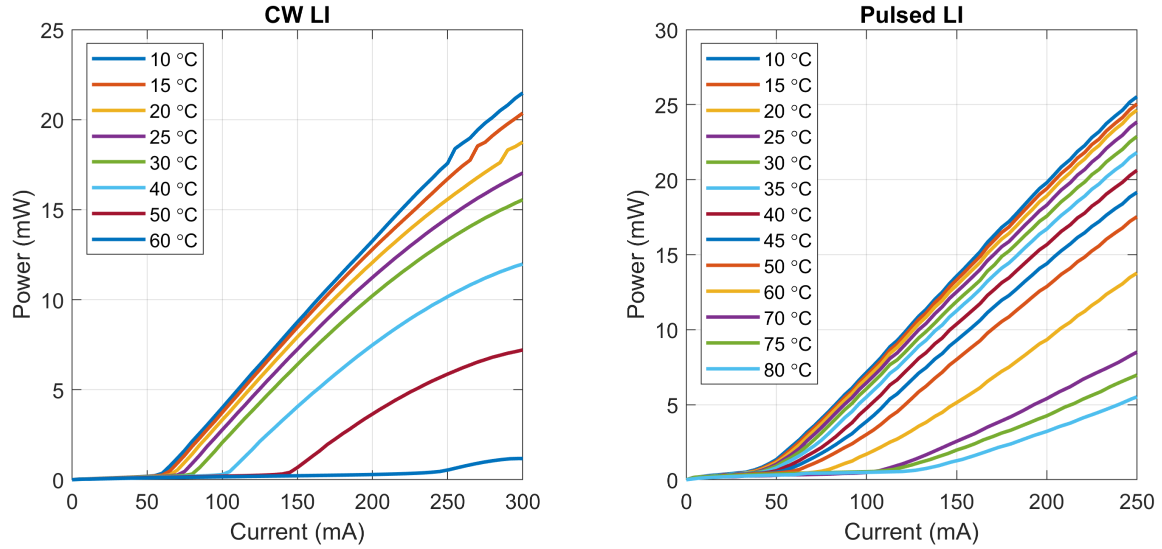

Figure 6.11: (a) CW current LI characteristic and (b) pulsed LI characteristic with varying temperature.

that is characteristic of QD lasers can be clearly seen under high current injection in Fig. 6.12(b).

In this chapter, InAs/GaAs QD lasers monolithically grown on (001) silicon entirely by MOCVD have been demonstrated. The lasers presented here exhibit reasonable output powers under both CW and pulsed current operation. This demonstrates the feasibility of MOCVD for growing QD lasers on silicon. Due to the high growth rates of MOCVD this is promising as a path towards large-scale monolithic integration of QD lasers for silicon photonics. In the next chapter, our work towards demonstrating MOCVD grown QD lasers with selective area heteroepitaxy (SAH) will be presented. Electrically pumped SAH lasers on silicon are really the ultimate goal in terms of high-volume production and monolithic integration with existing silicon photonics processes. The work presented in this chapter is a critical step towards realizing that goal.

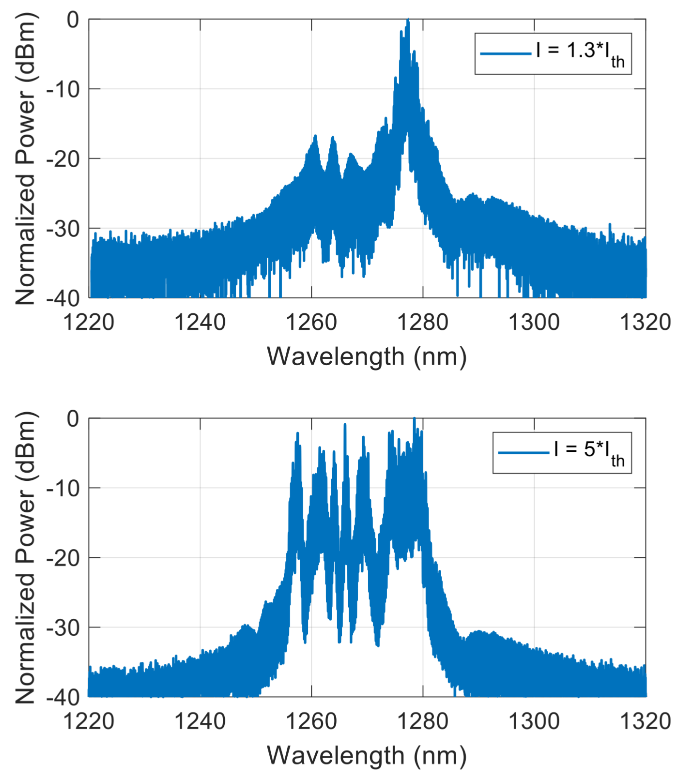

Figure 6.12: Lasing spectra at (a) just above threshold current and (b) at 5 times threshold for a 4 µm wide QD laser on Si.

Chapter 7

III-V on Silicon by MOCVD Selective Area Heteroepitaxy

Selective area growth is a technique in which a dielectric mask is deposited on a semiconductor substrate and then patterned, and epitaxial layers are grown locally in the un-masked regions. This approach is commonly used for active-passive integration on InP PICs [49]. MOCVD is the preferred technique as it allows for conformal growth on the patterned substrate, rather than MBE which is a line-of-sight technique and can lead to potential shadowing effects in the corners of the patterned area. MOCVD is also more selective and the growth parameters can be tuned such that growth primarily occurs on the exposed crystalline material, with little or no nucleation on the dielectric mask. Whereas MBE deposits across the whole sample and the material deposited on the dielectric mask ends up being poly-crystalline. This chapter specifically discusses the development of selective growth by MOCVD of III-V materials on silicon, known as selective area heteroepitaxy (SAH), with the goal of demonstrating electrically pumped lasers on silicon. Section 7.1 covers some background on MOCVD SAH in general, highlighting previous accomplishments. Process development for SAH device fabrication is presented in section 7.2, discussing some of the challenges that are specific to laser fabrication in a recess. Section 7.3 covers the fabrication process for the devices that were built for this

thesis, and section 7.4 presents corresponding test results and device characterization. Section 7.5 presents simulation results for coupling light from III-V SAH waveguides to Si/SiN.

7.1 MOCVD Selective Area Heteroepitaxy

The approach to SAH employed in this work involves etching recesses into a thick oxide layer on a silicon substrate, and growing the III-V epitaxy in the recess. There are other approaches to SAH, that involve growing laterally rather than vertically, but these will not be discussed here [136–138]. SAH has a number of advantages compared to planar growth. One advantage, and perhaps the most obvious, relates to photonic integration. For all the laser demonstrations on planar Si, the presence of a thick buffer layer has effectively prevented any chance of coupling light from the III-V waveguide to Si. With SAH however, the buffer layer is buried in the recess beneath the SiPh device layers so the waveguides can be vertically aligned. The schematic in Fig. 7.1 shows how a GaAs waveguiding layer can be aligned to SiN waveguides for coupling to SiPh. In this scheme, the light is first coupled to a dual SiN waveguide and then transitions to the Si waveguide below.

Another advantage of SAH relates to the mismatch in coefficient of thermal expansion (CTE). Stress due to the difference in CTE between Si and III-V can lead to cracking on the III-V surface, as discussed in the previous chapter. However, with SAH, the overall III-V footprint is smaller so the cumulative stress is lower. For growth in a long narrow recess, cracking is effectively eliminated in the perpendicular direction, although stress still builds up along the length of the recess and cracking can still occur. It should be noted that MBE growth in pockets (or recesses), while it is not strictly selective, still affords these two advantages; namely vertical alignment of the waveguides for integration

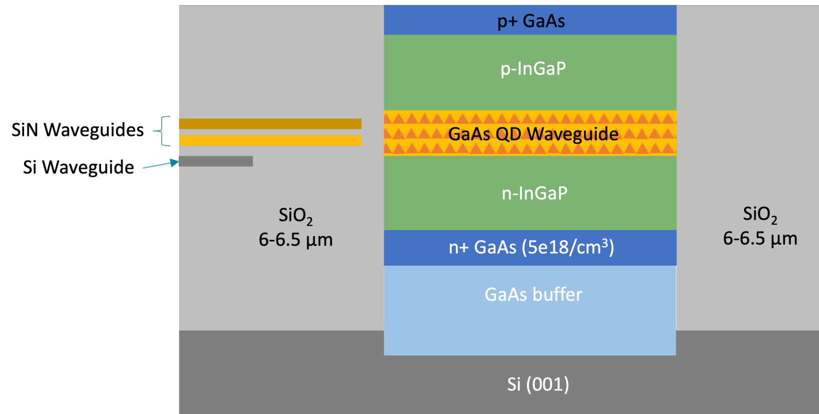

Figure 7.1: Selective area heteroepitaxy III-V laser stack showing vertical alignment to SiN waveguide layers. In this approach light is first coupled to SiN and can then be transitioned to the lower Si waveguide.

with SiPh and reduction of the thermal cracking problem. However, another advantage that is more specific to SAH by MOCVD is the absence of a gap between the crystalline III-V material and the SiO_2 sidewalls. With MBE growth, the material near the recess edges becomes polycrystalline and must be removed prior to laser fabrication which leaves a gap between the III-V and the SiPh waveguides [93, 94, 139]. This gap presents a significant challenge to efficient coupling. With selective growth by MOCVD, however, crystalline III-V material in the recess extends all the way to the SiO_2 sidewalls. Although there is some distortion, or "faceting", in the epi layers near the edges, it is typically only a few microns. It will be shown later via simulation that this is still preferrable to an air gap in terms of coupling efficiency. MOCVD growth is also desirable for high-volume production. The growth templates used later in this chapter start with a MOCVD grown GaP buffer layer. If the device layers can also be grown by MOCVD, then the entire layer stack could be grown in a single growth step, which is again advantageous in terms of production costs.

Prior to the device fabrication that was performed in this thesis, considerable work was done to optimize growth conditions and demonstrate QD and QW active regions via

MOCVD SAH. Some of this early development, specifically demonstrations of optically pumped lasers, is highlighted here before discussing the specific devices fabricated in this work.

7.1.1 Optically Pumped Lasers by SAH

While electrically pumped lasers by SAH are the ultimate goal, these are of course not possible without sufficient gain in the active layers. An intermediate step towards demonstrating electrically pumped lasers is to fabricate optically pumped lasers. This simplifies initial growth development since efforts can be concentrated primarily on optimization of the gain region (either QW or QD), without considering doping levels for electrical contacts and current injection, or the thick cladding layers necessary for electrically injected lasers. The fabrication process is also simplified as no metalization steps are required.

The growth template started with either nano V-groove patterned Si (001) or flat on-axis (001) Si, with a 6 µm-thick SiO_2 layer deposited on the surface. 15 µm wide and 25 µm wide recesses with varying lengths were then patterned and etched into the thick oxide layer to expose the underlying Si in preparation for SAH growth [60, 140, 141]. Sample preparation and growth of the GaAs buffer followed the procedures described in [142]. Optically pumped microdisk lasers (MDLs) were then fabricated on these templates with both QW and QD active regions [140, 141]. These MDLs consist of a circular cavity, a few microns in diameter, which supports a whispering gallery mode. Lasing is achieved by optically pumping the MDLs with a 660 nm pump laser in a micro-PL setup. Fig. 7.2 shows an example of MDLs grown by MOCVD SAH on both flat-bottom Si and nano V-groove Si templates. Lasing was demonstrated in both cases, however, the nano V-groove devices demonstrate lower threshold and less variation between devices. This

should come as no surprise as nano v-grooved silicon has been shown to suppress defects such as APBs leading to higher quality QD material.

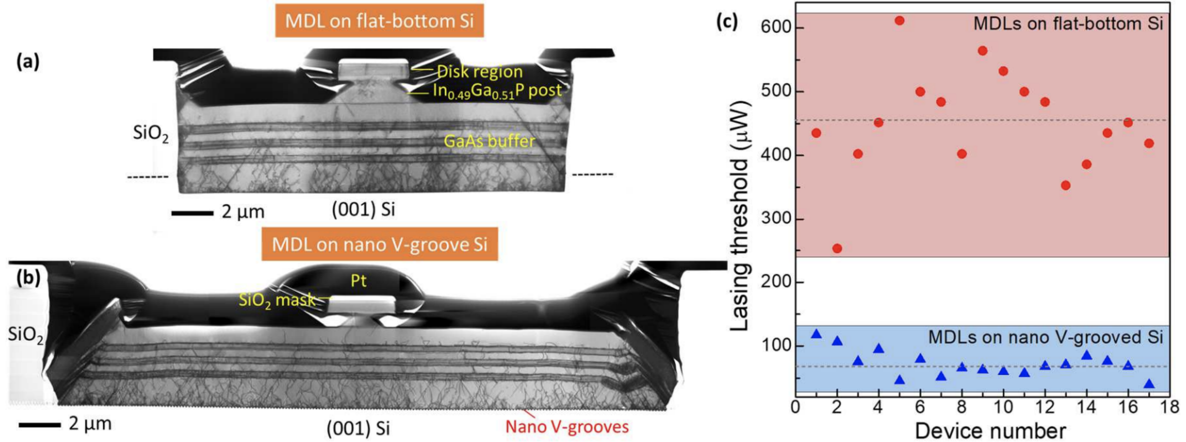

Figure 7.2: Examples of QD microdisk lasers grown by MOCVD SAH and presented at the International Semiconductor Lasers Conference (ISLC) 2022 [140]. Both flat-bottom Si and nano V-groove Si templates were used, with noticeable performance benefits for the V-groove Si devices. Figure adapted from [140].

7.1.2 SAH Laser Epitaxy for Electrical Pumping

Selective area growth presents a number of unique challenges compared to blanket growth. The MOCVD development will only be discussed briefly here, but more details can be found elsewhere [60, 85, 140–144]. Some of the challenges arise as a result of the different growth rate during SAH. The growth rate is typically higher for SAH than for planar growth, and local variation is observed across the sample (e.g. faster growth near the edges of the recess compared to the center). The difference in rate means that growth parameters must be retuned to achieve the target layer thicknesses, composition, and doping levels. With SAH grown QDs already demonstrated in the optically pumped MDLs, one of the next steps is to demonstrate high doping levels for the n- and p-GaAs contact layers. Early growths suffered from low doping in the contact layers, which prevented the formation of good electrical contacts. To experimentally verify sufficient

doping, the contact layers were grown by SAH on the same GoVS template used for the MDL demonstrations. Fig. 7.3(a) shows this structure for the n-contact with 650 nm of highly doped n-type GaAs grown on GoVS. Fig. 7.3(b) shows the mask layout for depositing metal pads on GaAs in a recess. The transfer length method (TLM) is used to determine contact resistance and GaAs resistivity [145]. Four TLM patterns with different dimensions were included on the mask. Fig. 7.3(c) shows IV measurements for the different pad spacings on one TLM pattern and Fig. 7.3(d) shows resistance versus pad spacing for the 4 different measurements. The TLM measurement measures the resistance, R_T, between metal pads with contact area width, W, and pad spacing L. These are related by,

$$R_T = \frac{R_s}{W}(L + 2L_T) \tag{7.1}$$

where R_s is sheet resistance and L_T is the transfer length. The contact resistance, R_C and semiconductor bulk resistivity ρ are calculated with the following equations, where ρ_C is the specific contact resistance (in $\Omega \cdot cm^{-2}$) and t is the thickness of the semiconductor film.

$$R_C = \frac{\rho_C}{L_T W} = \frac{R_s L_T}{W} \tag{7.2}$$

$$\rho = R_s \cdot t \tag{7.3}$$

The measurements in Fig. 7.3 resulted in contact resistance in the range of 1-2 Ω which is typical for n-type GaAs contacts [146,147], and GaAs resistivity $\rho \approx 0.003\ \Omega{\cdot}cm$. For the purpose of fabricating devices, the ability to demonstrate good contacts with reasonably low resistivity is perhaps more important than knowing the exact doping level and these measurements indicate no issue in this regard. However, the doping level can be approximated from the resistivity [148, 149]. The approximate doping level for this structure is in the range of 2.4e17 - 1.4e18 cm^{-3}. This is a range because resistivity

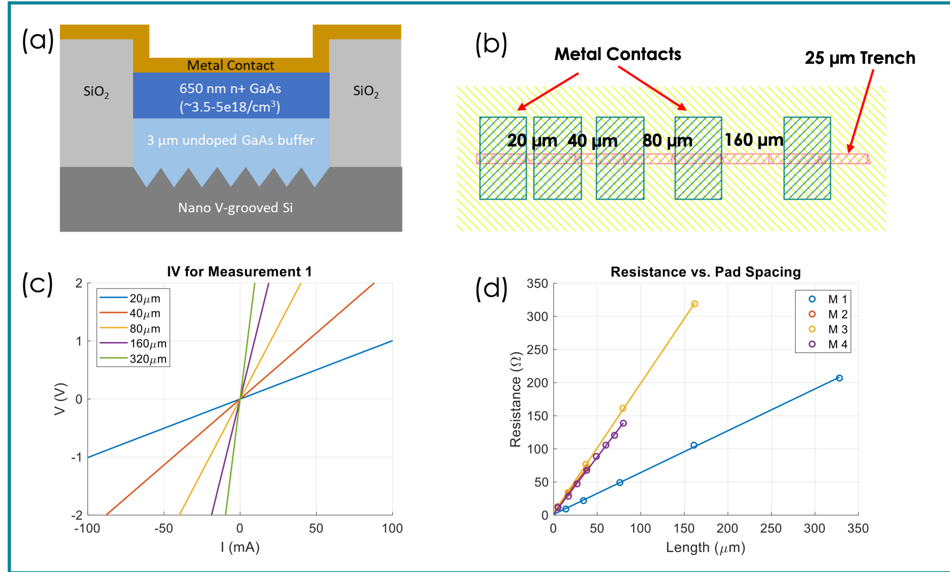

Figure 7.3: (a) n-GaAs contact layer grown on GoVS by SAH with metal contact pad, (b) layout for TLM measurements, (c) IV curves for different pad spacings on one TLM device and (d) resistance versus metal pad spacing for all 4 TLM devices.

is dependent on mobility which is not known without a priori knowledge of the doping level. Resistivity is given by,

$$\rho = \frac{1}{eN_D\mu_e} \tag{7.4}$$

where μ_e is electron mobility, and N_D is electron donor concentration. Fig. 7.4(a) shows electron mobility in GaAs versus doping concentration [150] and Fig. 7.4(b) shows measured GaAs resistivity versus doping concentration from [149]. Similar experiments demonstrated good contacts and low resistivity on p-type GaAs grown by SAH, indicating reasonable p-type doping in GaAs as well.

The full laser stack devices that will be used in the following sections were all grown on a GaP-on-Si template, rather than GoVS (although similar structures have been grown by SAH with the GoVS template [60] at UCSB). These templates were provided by our collaborators at SUNY. The samples provided were either 300 mm Si or 300 mm SOI wafers (diced into small coupons for growth and fabrication) with the recesses pre-

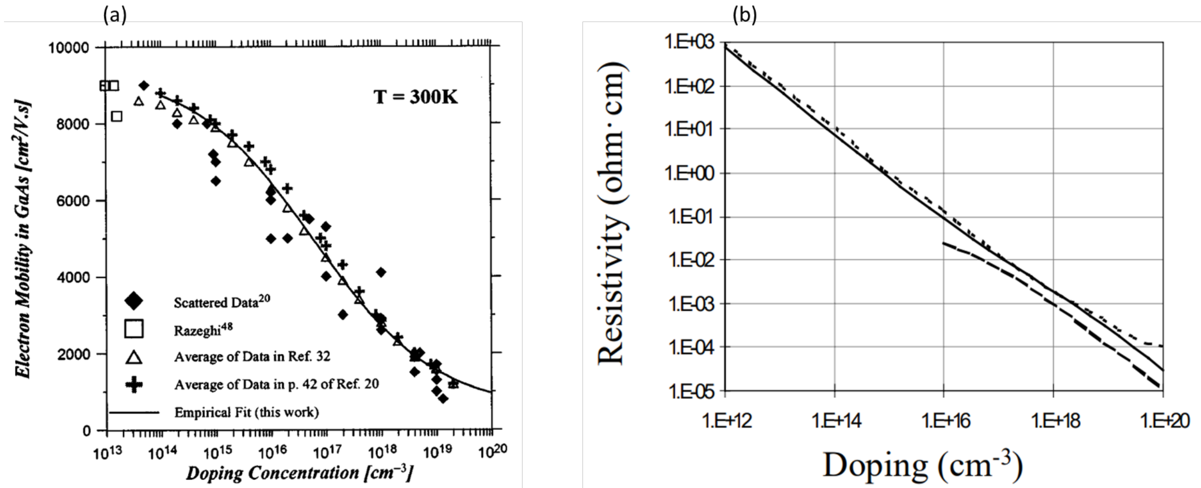

Figure 7.4: (a) Electron mobility in GaAs vs doping concentration adapted from [149], and (b) GaAs resistivity vs doping from [150]

patterned into the oxide. The MOCVD GaP buffer was grown by NAsP$_{IIIV}$ [88, 151] on a 300 mm wafer before dicing and sending to UCSB for MOCVD growth. The GaP-on-Si approach is an alternative to V-groove patterned Si that provides similar advantages in terms of reducing the occurence of APBs and other defects [89–91]. The nominal full laser stack for an electrically pumped laser is shown in Fig. 7.5. In this figure, SN and FN represent SiN waveguide layers, and SE is the Si waveguide layer, all of which are present in the SiPh process at AIM Photonics [152] where these wafers originate. The samples were already patterned with the oxide recesses when they arrived at UCSB for III-V growth. InGaP was chosen for the p- and n-cladding layers as it can be grown selectively, whereas selective growth of thick AlGaAs is extremely difficult [140]. Additionally, InGaP can be grown at lower temperatures than AlGaAs (525 °C, rather than ∼700 °C) which avoids unwanted annealing effects in the QDs [87].

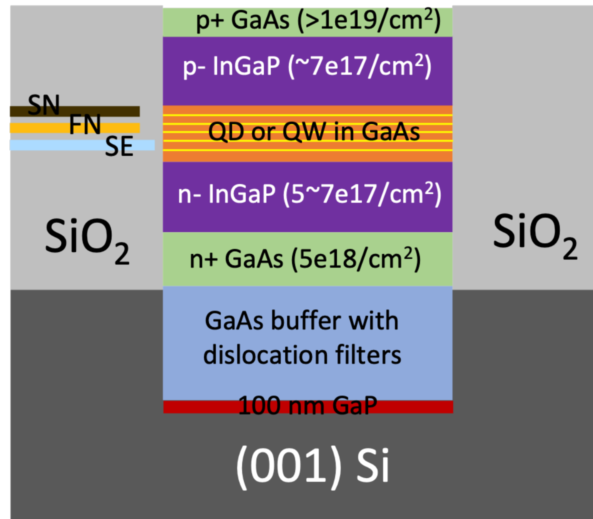

Figure 7.5: Epitaxial layers for a typical laser structure grown by MOCVD SAH, using a GaP-on-Si template. The SiN (SN, and FN) and Si (SE) waveguides shown here only indicate the vertical position of these layers in the AIM Photonics process; their horizontal position relative to the III-V layer stack depends on device design.

7.2 Fabrication Process Development

7.2.1 Parasitic III-V Particles on Selective Growth Samples

While MOCVD growth is generally selective, there is still a tendency for some parasitic III-V particles to nucleate on the SiO_2 surface [137]. While this doesn't necessarily affect the III-V material quality in the recess, these parasitic particles can present a challenge for fabrication later. Some of the particles can be multiple microns in diameter and if they are densely distributed across the surface this can inhibit the ability to get reliable photoresist coverage for lithography. Additionally, the particles can interfere with alignment marks which again presents a challenge for lithography. To remove these parasitic growths, a simple wet etch process was developed. The composition of the particles is primarily a combination of GaAs and InGaP, so the etch chemistry needs to etch both of these compounds. For this purpose a solution of hydrochloric acid (HCl), phosphporic acid (H_3PO_4) and hydrogen peroxide (H_2O_2) can be used [153]. The process

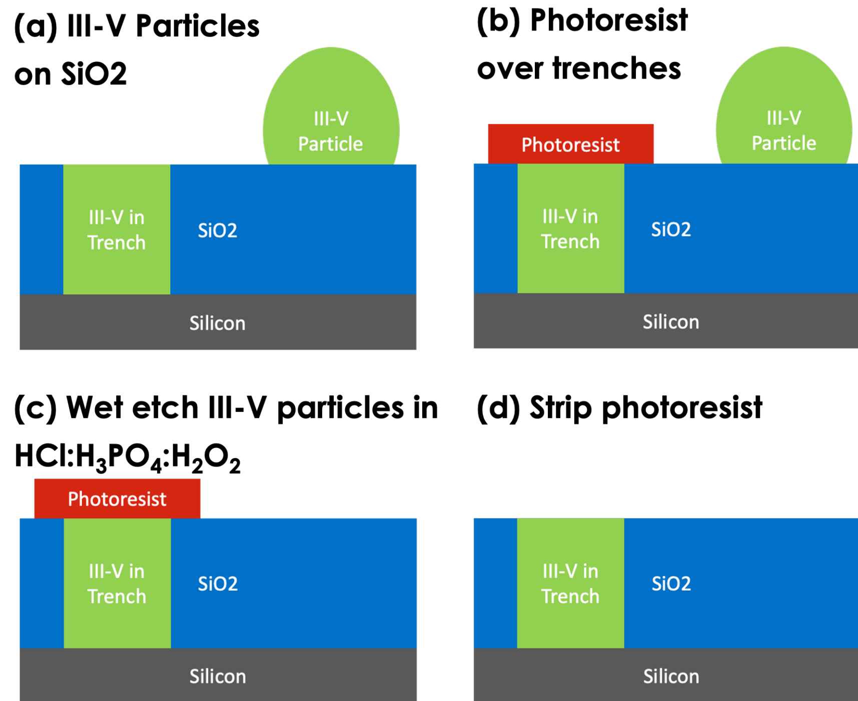

Figure 7.6: Wet etch process to remove parasitic III-V particles that form on SiO_2 during growth without damaging the epitaxial layers in the recess.

flow is shown in Fig. 7.6 and begins with spinning a thick photoresist (PR) on the sample (in this case SPR220-3.0 which is approximately 2.7 µm thick), then exposing and developing the resist to leave a protective layer of PR over the III-V. The PR extends beyond the recess edges by approximately 10 µm to avoid any chance of the wet etch undercutting the PR and etching into the III-V epitaxy. The sample is then immersed in a $HCl{:}H_3PO_4{:}H_2O_2$ (1:5:1) solution to etch the particles. GaAs is etched via an oxidation process where the H_2O_2 acts as an oxidizing agent for the GaAs surface and the resulting oxide is then etched with HCl. $HCl{:}H_3PO_4$ is a well known etchant for InP and InGaP materials. After mixing, the solution is allowed to sit for approximatlely 5 minutes, after which the sample is immersed for another 5 minutes. The surface is then inspected under a microscope and additional 1 minute etches are performed as needed until the particles are completely removed.

Results from the parisitic III-V etch are shown in Fig. 7.7. Fig. 7.7(a) shows particles on the surface before etching and Fig. 7.7(b) is a close-up SEM image of a typical parasitic growth. Figs. 7.7(c-d) show the same location on the sample before and after etching, demonstrating full removal of parasitic particles that would otherwise interfere with the alignment marks. With this simple wet etch process to remove parasitic growths, the sample is now ready for device fabrication.

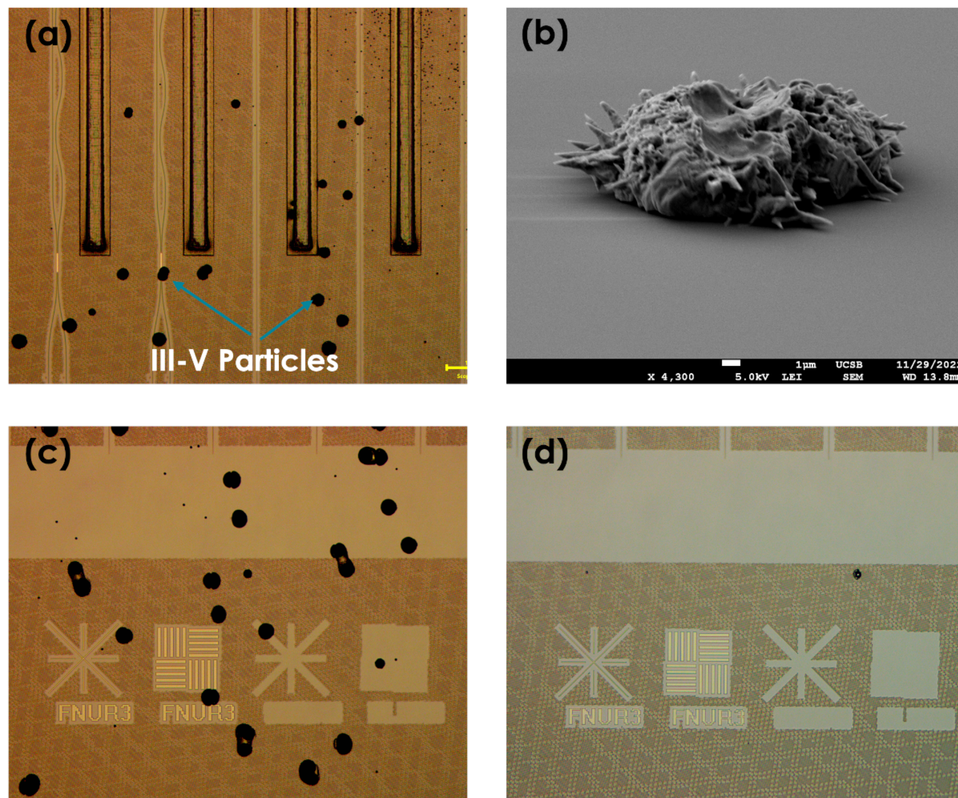

Figure 7.7: (a) Microscope image of III-V particles on sample surface with PR protecting the III-V material in the recesses; (b) SEM image of a single particle; (c) III-V particles before etching and (d) the same area on the sample after wet etching in $HCl:H_3PO_4:H_2O_2$ solution

7.3 Selective Area Heteroepitaxy Device Fabrication

Multiple fabrication runs were performed on selectively grown samples with the goal of demonstrating electrically pumped lasers by SAH. These are summarized below in Table 7.1 in the order in which they were fabricated. Two of the fabrication runs included a full laser epitaxial stack, one with QWs and the other with QDs for the active region. The other "short-loop" fabs used a reduced epi stack for the purpose of debugging which layers contributed to the high diode series resistance encountered in the first fab. All of the fab runs used the GaP-on-Si template from SUNY, and the last two used a modified version with wider recesses. This section begins with a general description of the mask layout and fabrication steps which were common to all fabrication runs, before presenting device results in the next section.

Table 7.1: Fabrication Runs

Fabrication	Epitaxy	Template
Fab 1	QW full laser stack	SUNY
Short-loop (x3)	PiN junction, reduced stack	SUNY (wide)
Fab 2	QD full laser stack	SUNY (wide)

7.3.1 Mask Layout

All of the devices fabricated in this section were grown on the GaP on Si templates described above. Fig. 7.8(a) shows the layout for a single die showing the locations of the recesses (in green) where subsequent III-V material is grown, and in the inset, a close-up of the layout with the III-V layers added for laser fabrication. The inset also shows TLM patterns that can be used for measuring contact resistance. A photograph of the diced sample before fabrication is shown in Fig. 7.8(b) with the corresponding mask area highlighted in Fig. 7.8(a).

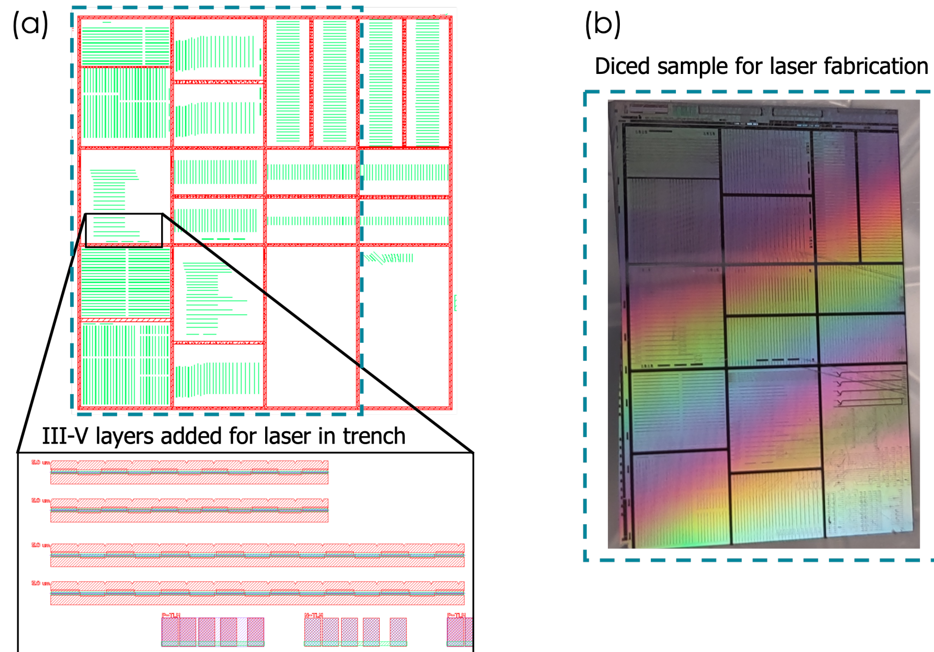

Figure 7.8: (a) Mask layout showing III-V recesses and close-up of III-V laser-in-recess layout in the inset. (b) Photograph of diced sample after MOCVD III-V growth using GaP-on-Si template, but before device fabrication.

7.3.2 Fabrication

Figure 7.9 schematically demonstrates the process flow for fabricating laser diodes in a recess. The wet etch for removing parasitic III-V growths on the oxide was performed prior to starting the process shown here (step 1 is the "clean" sample). After parasitic growth removal the next step is the p-contact deposition (step 2). This consists of a Ti/Pt/Au (20/40/200 nm) metal stack deposited via electron beam deposition. After the p-contact, the sample is covered with a SiN/SiO_2 stack (∼500 nm total) to serve as a hard mask for waveguide etching. Waveguide lithography was performed with the Heidelberg maskless aligner (MLA) in the UCSB nanofab using SPR220-3.0 photoresist, the hard mask was etched and then the waveguide ridge was etched using the InGaP dry etch recipe described earlier (step 3). Due to the nature of selective growth with MOCVD, the III-V stack thickness varies across the length of the recess, tending to be

thicker near the edges and thinner in the middle. So, the waveguide dry etch does not reach the n-GaAs at the same time across the length of the recess. To ensure that the n-GaAs is exposed across the whole length, and to avoid the risk of accidentally etching through the n-GaAs, the waveguide etch is deliberately stopped in the lower cladding. This is followed by another lithography step, and a selective wet etch to remove the remaining InGaP lower cladding and stop at the n-GaAs (step 4). After etching to the n-type GaAs layer, another metal deposition is performed to form the n-contact with Ni/AuGe/Ni/Au (5100/20/300 nm) (step 5). The sample is then passivated with 5 nm of AlO and 10 nm of SiO_2 using atomic layer deposition (ALD) followed by a 700 nm thick SiN/SiO_2 stack deposited with PECVD (step 6). Vias were then opened to access the n- and p-contacts (step 7) in two separate lithography and etch steps. Finally the metal pads were deposited for the probe metal (step 8).

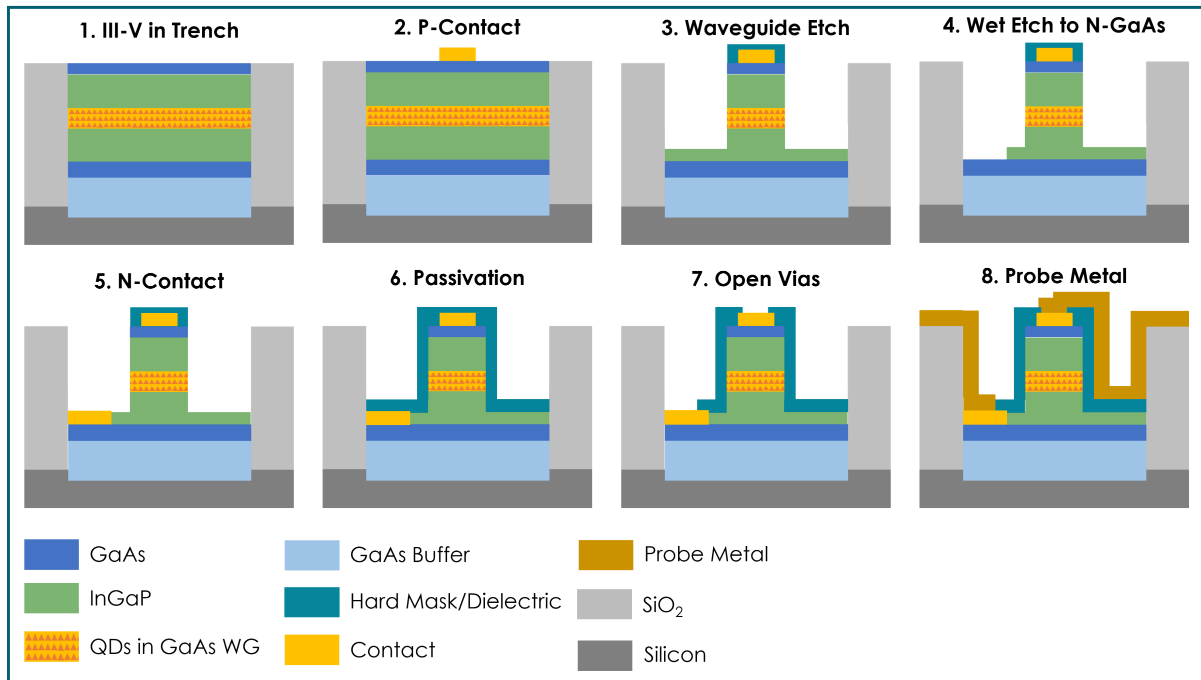

Figure 7.9: Overview of fabrication process for selective area heteroepitaxy devices grown in a recess, after removal of parasitic III-V growths.

Fig. 7.10 shows images from various stages of fabrication. Fig. 7.10(a) is an SEM image of the waveguide ridge after both dry etching and wet etching to remove lower InGaP cladding. The smooth surface on either side of the ridge is the n-GaAs contact layer where the selective wet etch stopped. The leftover material around the edges of the recess is a result of the uneven growth; when the non-selective dry etch was stopped, most of the exposed surface was InGaP (see Step 3 in Fig. 7.9), but some of the surface near the edge was GaAs because the stack is, on average thicker near the edge. So, the selective etch only removed the exposed InGaP, and left some GaAs material in place near the edge. Fig. 7.10(b) shows a top-view SEM of the waveguide ridge after depositing probe metal. Fig. 7.10(c) is a cross-section after cleaving the fabricated devices into bars. Figs. 7.10(d-e) show top-view microscope images after depositing the p-contact, and before etching the ridge. Fig. 7.10(f) is a microscope image of devices after fabrication.

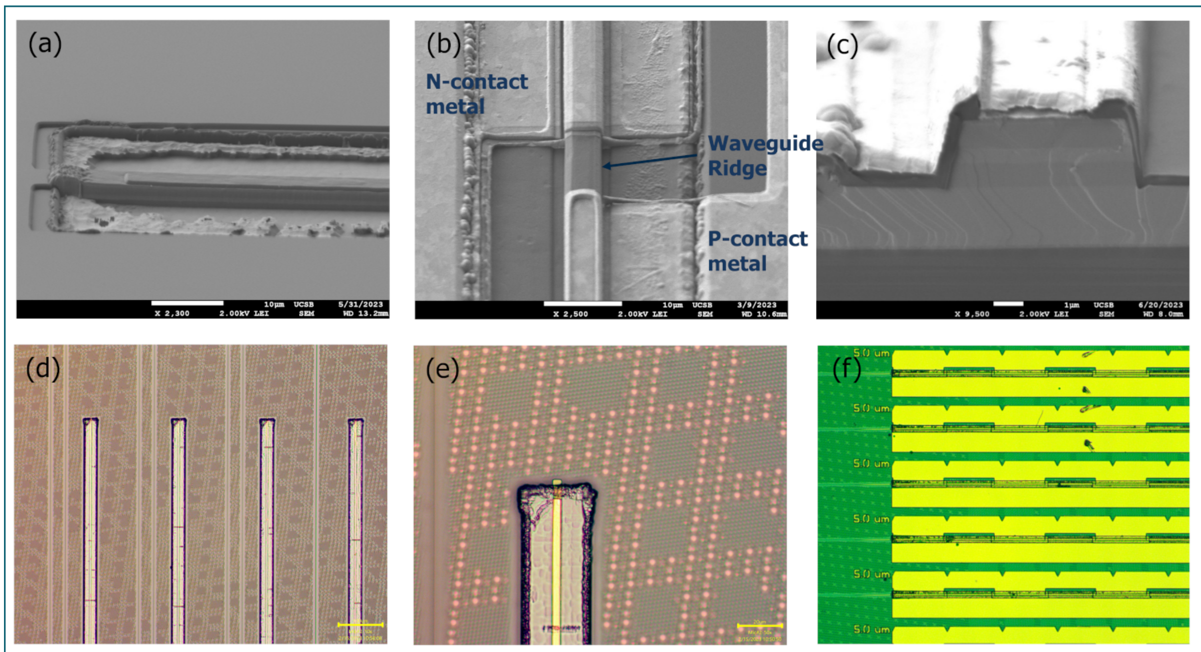

Figure 7.10: SEM images of (a) waveguide ridge after etching, (b) top-view after probe metal deposition, (c) cleaved facet after fabrication. Microscope images of (d-e) III-V material in recesses after p-contact but before ridge etch, and (f) fully fabricated devices before cleaving. III-V material grown on the GaP-on-Si template.

7.3.3 Device Results

Fabrication 1 - QW Devices

The first fabrication used a QW active region and was grown using the GaP-on-Si template. The mask layout, shown in Fig. 7.7 contained primarily 20 µm and 30 µm wide recesses oriented both vertically and horizontally. PL measurements on the QWs showed a strong peak near 980 nm which is shown in Fig. 7.11. After fabrication, the

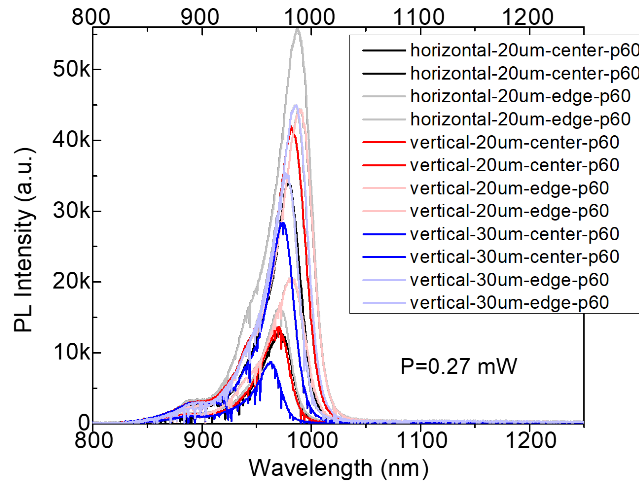

Figure 7.11: PL emission measured for SAH QWs with peak around 980 nm, and strongest PL from 20 µm wide recesses. QW epitaxy grown on a GaP-on-Si template.

diodes were tested on the die before cleaving or thinning the sample. The mask layout included TLM test structures for measuring contact resistance as well; these results are shown in Fig. 7.12(a). Both the n- and p-contacts appear ohmic with typical contact resistance ($\sim 1 - 2\ \Omega$ for both) and reasonable sheet resistance. However, the diodes exhibited very high series resistance under forward bias. Fig. 7.12(b) shows a typical IV curve from one of the devices which demonstrates less than 0.5 mA of current even when biased at 4 V. Because the contacts are good, we can reasonably assume that the high series resistance likely originated from the InGaP cladding layers.

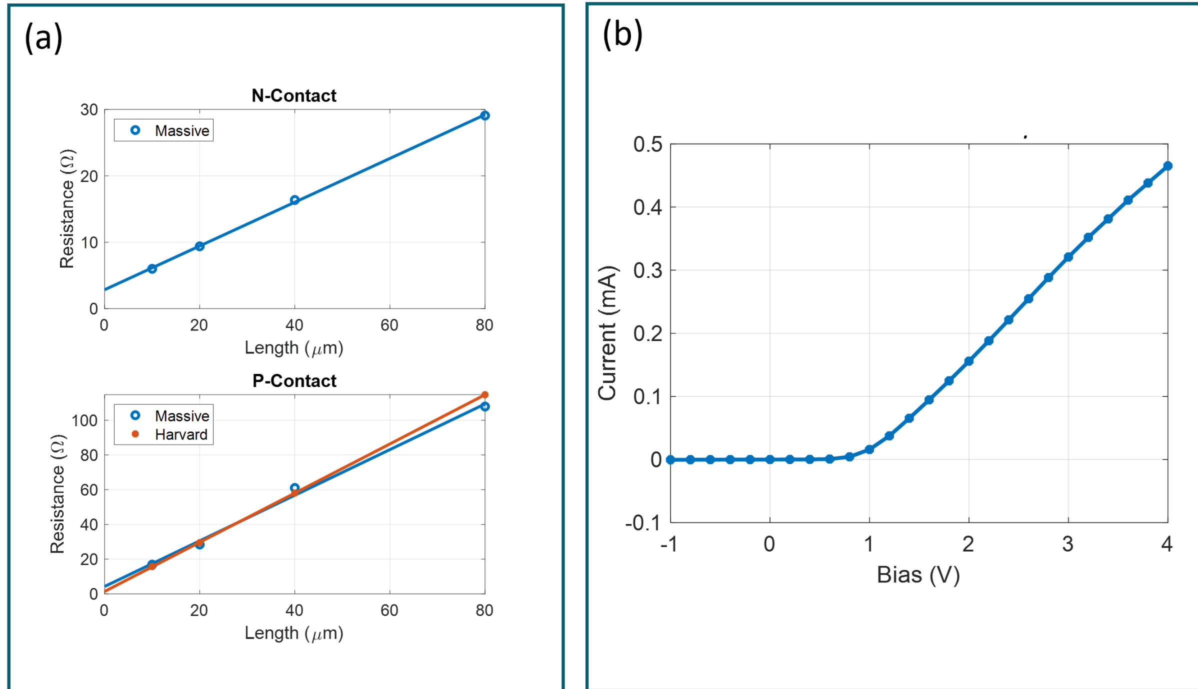

Figure 7.12: Electrical measurements on SAH QW diodes. (a) N- and P-contact measurements showing ohmic contacts with reasonably low resistance, and (b) diode IV curve demonstrating very high series resistance due to phase separation in InGaP cladding layers.

Short Loop Electrical Diode Fabrication

Based on results from the first fabrication it was assumed that the InGaP cladding layers were responsible for the high diode series resistance as phase separation in InGaP on GaAs is a known issue [87]. Because InGaP is only lattice-matched to GaAs at a specific composition ($In_{0.49}Ga_{0.51}P$) any variation in the composition leads to strain. This is particularly problematic for the thick InGaP layers that are necessary for laser cladding. Excess buildup of strain leads to a variety of defects such as threading dislocations and stacking faults.

To debug the high resistance problem and try to identify which layers were the root cause, 3 test structures were grown and are shown in Fig. 7.13. The InGaP growth recipe was optimized to achieve closer lattice matching with GaAs and the doping level

in the cladding and contact layers was increased. The n-GaAs lower contact layer was also made thicker to allow for greater tolerance during fabrication. These test structures included a simple GaAs PiN junction with no InGaP layers in Fig. 7.13(a), a full laser stack excluding p-InGaP cladding in Fig. 7.13(b) and a full laser stack excluding n-InGaP cladding in Fig. 7.13(c), all with 5 layers of QDs in the GaAs waveguide layer, which had a total thickness of around 600 nm. These samples also used the GaP on Si template, but with a modified version of the layout that had wider openings; each recess was widened by 8.5 µm so the 30 µm wide openings became 38.5 µm. The wider recesses are easier for fabrication as there is more space to fabricate devices in the flat smooth area toward the center. A simplified version of the fabrication process with a modified mask layout was used to create electrical diodes. This involved simply etching down to the n-GaAs layer on one half of the recess and then depositing metal for the p- and n-contacts. Results from IV curve testing are also shown in Fig. 7.13 for each of the three structures. The IV curves are significantly improved compared to the previous fabrication in all 3 cases. The improvement in the IV curves from these devices indicated that the InGaP cladding growth was sufficiently improved to grow the full stack with both cladding layers.

Fabrication 2 - QD Devices

For the final fabrication, the full laser stack (with both n-InGaP and p-InGaP claddings) was grown on the wide recess templates with 5 QD layers. Fig. 7.14 shows the measured PL spectrum from the QDs, with peak emission near 1230 nm for the 30 µm wide vertical recesses. The fabrication process and sample layout were both identical to Fabrication 1, but with the wider recess template. The label in Fig. 7.14 says "30 µm" but in reality they were 38.5 µm wide on this template. After fabrication, the electrical performance of the devices was tested and the relevant results are shown in Fig. 7.15. Fig. 7.15(a) shows contact resistance measurements on TLM patterns, demonstrating reasonably low

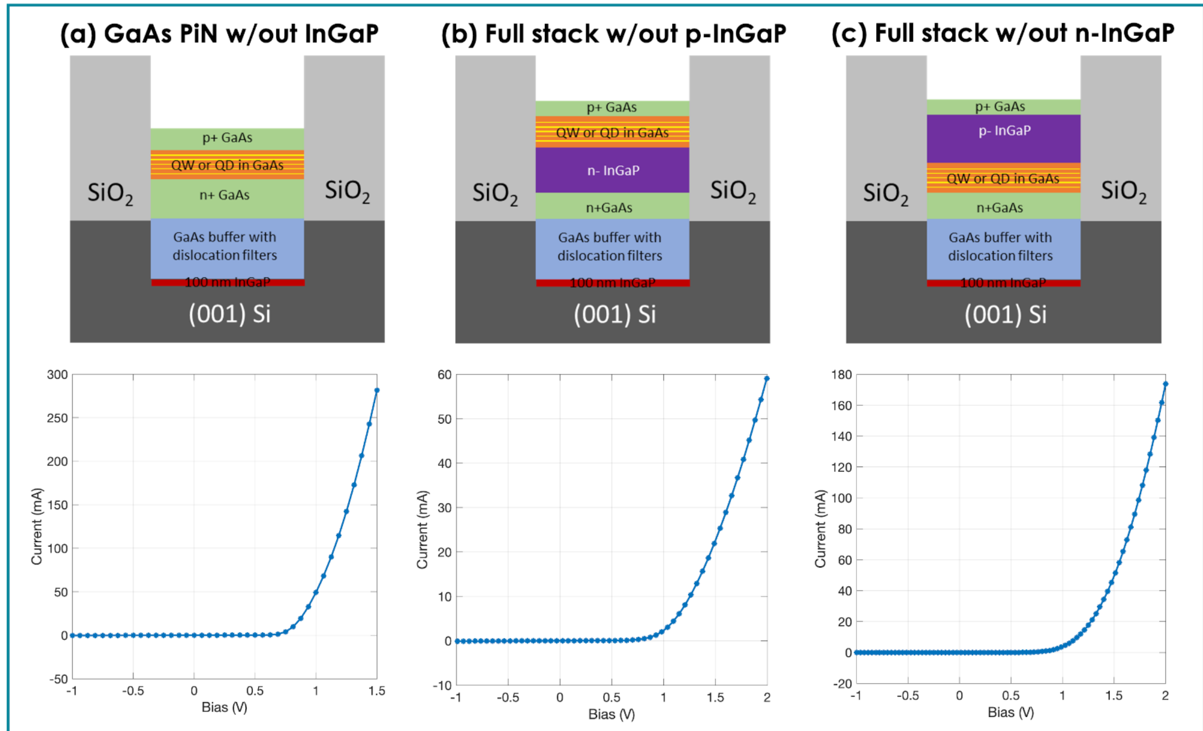

Figure 7.13: III-V layer structure and corresponding diode IV curves for (a) GaAs PiN junction, (b) full laser stack excluding p-InGaP cladding and (c) full laser stack excluding n-InGaP cladding. All three structures utilized the GaP-on-Si growth template.

contact and sheet resistance values for both p and n-type. The numbers in Fig. 7.15(a) should be interpreted cautiously because the calculations assumed the contact is applied across the entire width of the recess when in reality there is some area near the edges of where the surface cannot be contacted reliably (refer to e.g. Fig. 7.10). However, the contacts were clearly ohmic, and the TLM data points are linear with reasonable resistance so it's safe to assume that the slow turn-on in Fig. 7.15(b) is not a result of poor contacts. Fig. 7.15(b) shows an exemplary diode IV curve in one on the 38.5 µm wide recesses. In the linear region, the series resistance is approximately 8 Ω which is not unreasonable. However, the diode turn-on is very slow, and the curve doesn't become linear until beyond 4 Volts. The inset to Fig. 7.15(b) shows some improvement after burning in the contact by applying 100 mA of current for an extended period (over an

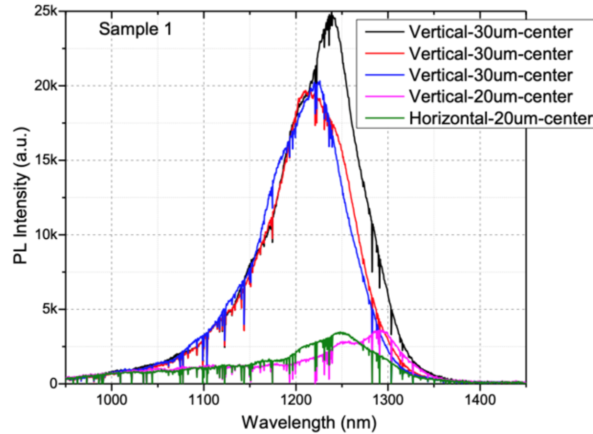

Figure 7.14: Measured PL emission from SAH QDs with peak wavelength around 1230 nm, and strongest emission from 30 µm wide recess. QD epitaxy grown on GaP-on-Si template.

hour in total), but the IV curve still shows slow turn-on. In spite of the slow turn-on, this electrical performance is a significant improvement from the first fabrication. Fig. 7.15(c) shows an IV curve from the first fab for comparison. Furthermore, some of the devices on planar Si demonstrated in the previous chapter had very similar IV curves (before additional annealing) and still demonstrated lasing. After initial electrical test-

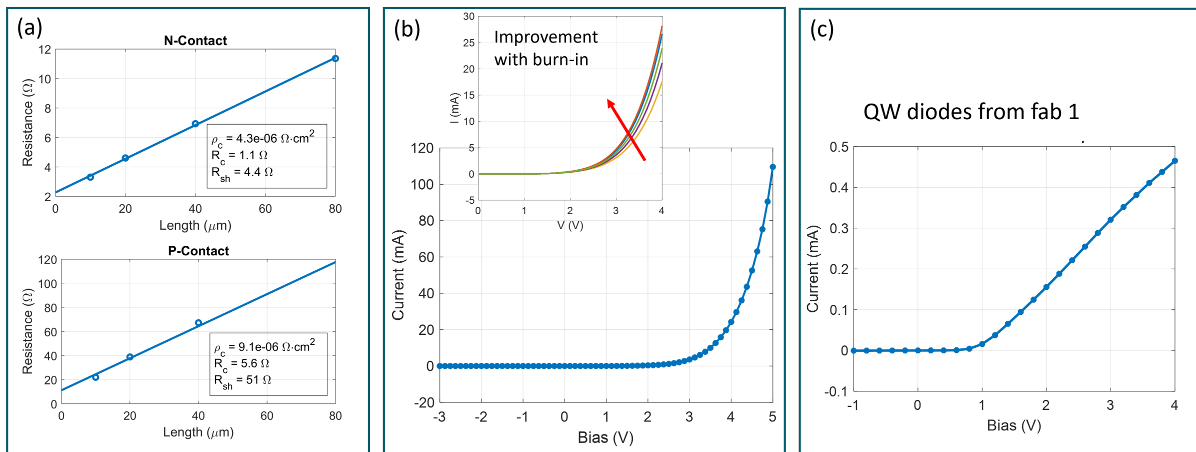

Figure 7.15: (a) N- and P-contact measurements on TLM patterns and (b) diode IV curve demonstrating reasonable series resistance in linear region but slow turn-on. Slight improvement with contact burn-in shown in inset. (c) IV curve from fab 1 QW devices for comparison.

ing, the sample was thinned to approximately 150 µm and cleaved into bars for testing. The cleaved facet from one of these devices was shown in Fig. 7.10(c). Because the III-V is not present across the entire sample surface, and the underlying substrate is Si, it was difficult to get good quality cleaves. As a result some roughness is seen on the facet in Fig. 7.10(c), however it is not severe enough to entirely prevent lasing in its own right. Figs. 7.16(a-b) show the device under test with QD emission clearly visible in 7.16(b) with the lights turned off in the lab. However, Fig. 7.16(c) shows a typical LIV characteristic for all the tested devices, which demonstrates LED-like behavior but no lasing. Every device on the sample was tested, and exhibited similar performance. The stage was also cooled down to 10 °C and the devices were tested under pulsed current operation and driven hard out to ~800 mA with narrow 100 ns pulses and still no lasing was observed.

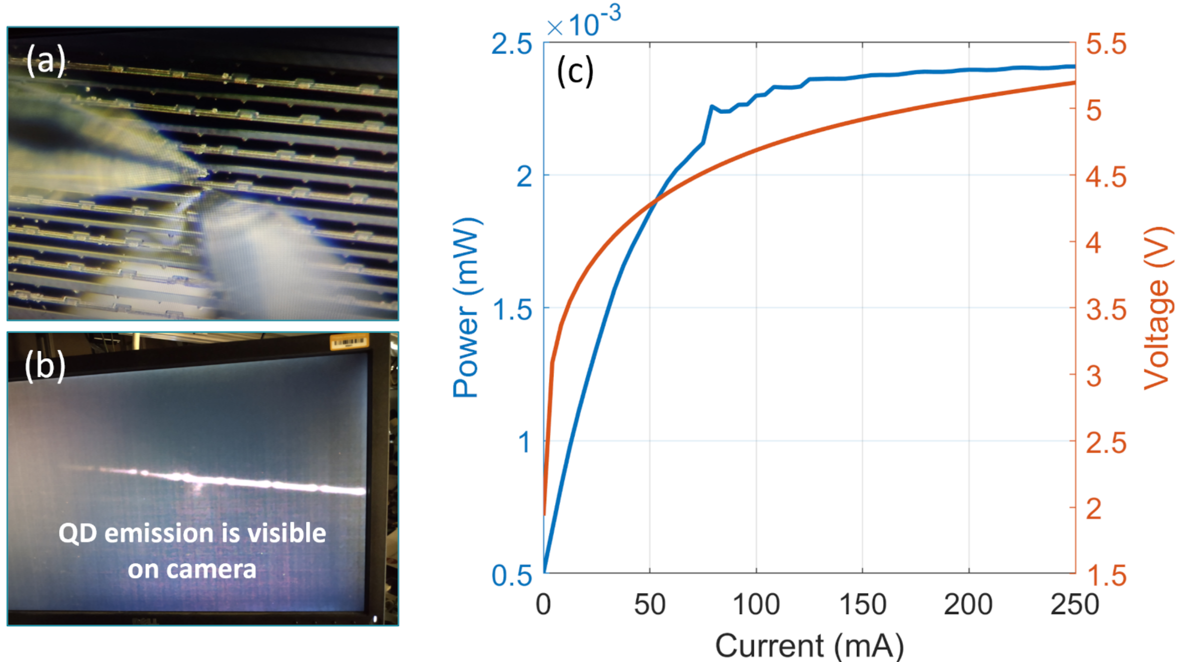

Figure 7.16: (a) Picture of cleaved device under test and (b) QD emission observed on camera. (c) LIV curve for cleaved facet device under CW operation demonstrating LED behavior but no lasing.

InGaP Failure Analysis

One of the fabricated devices from Fab 2, was taken for TEM analysis to uncover issues with the epitaxy that might cause the slow turn-on and low QD gain. Fig. 7.17(a) shows a cross section of the device after performing a focused ion beam (FIB) cut in the center of the recess, with the metal layers clearly contacting the semiconductor and the passivation dielectric still intact. The QD layers, however, are quite "wavy" as a result of the uneven InGaP layer on which they were grown. Fig. 7.17(b) shows a close-up TEM image of the QD layers on InGaP where the surface non-uniformity is clearly visible. The yellow arrows point out phase separation in the lower InGaP cladding, which causes the waviness seen in the QD layers. The phase separation is caused by Ga-rich defects (seen in Fig. 7.17(c-d)) which results in defects due to lattice mismatch from the inhomogeneous InGaP composition. Phase separation in the lower InGaP cladding which causes the surface waviness results in defective InAs clusters during QD growth. These clusters result in a high density of large dots which affects the QD stacking. Fig. 7.18(a) shows a close up TEM image of the defective QD layers which in turn causes dislocation defects to cascade into the upper InGaP cladding, further degrading the quality of the overall epi stack. Fig. 7.18(b) highlights the presence of stacking faults (SF) and antiphase boundaries (APBs) in the N-GaAs layer which likely contributed to the initial phase separation observed in the lower InGaP cladding. The conclusion to all of this is that phase separation in the lower InGaP cladding layer causes the surface waviness observed at the start of QD growth. This in turn results in highly defective QD layers (hence the low gain, and relatively low PL intensity compared to QWs) and the defects propagate into the upper InGaP cladding. This is consistent with our observations from the short-loop fabrication where the diode with only lower InGaP cladding displayed the worst IV characteristic (see Fig. 7.13(b)). In the device with only upper InGaP, any defects that

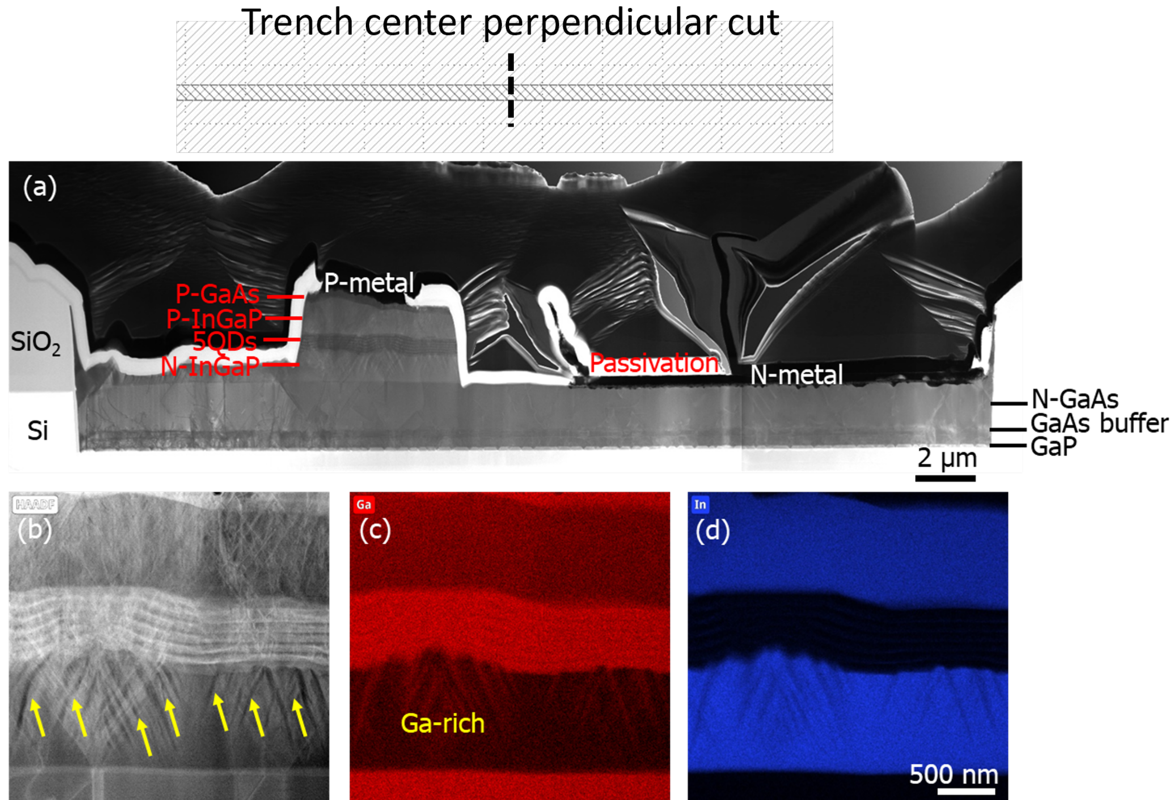

Figure 7.17: (a) FIB cut and cross section TEM in center of recess after full device fabrication. (b) Close-up showing clear phase separation in InGaP, and EDX mapping of (c) Ga and (d) In elements.

might have been present on the n-GaAs surface were likely terminated during QD growth in the GaAs waveguide layer which left a good surface for growing the upper InGaP.

7.4 Next Steps for Lasers in Recess

Based on the discussion thus far, the InGaP claddings are clearly the most problematic in terms of demonstrating electrically pumped lasers by SAH. QD and QW active regions with strong PL emission have been grown by SAH, and optically pumped MDLs have been demonstrated [60, 140, 141]. This shows that it is possible to grow active layers by MOCVD SAH. Good electrical contacts have been demonstrated, on both n-GaAs

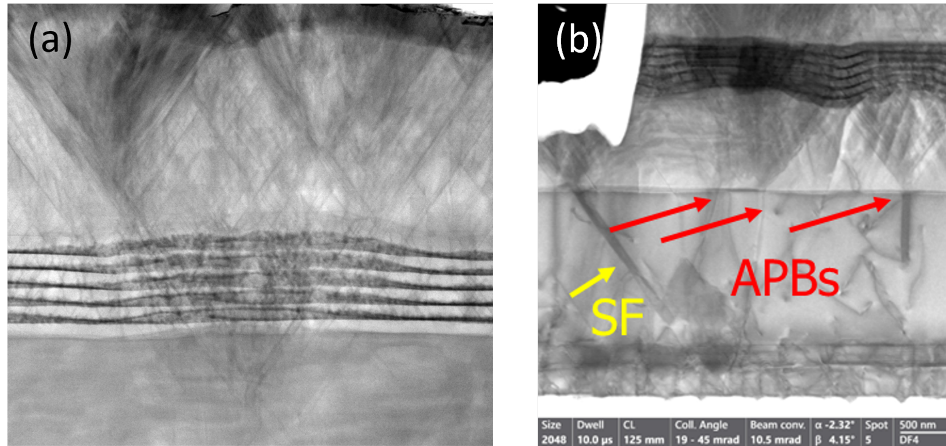

Figure 7.18: (a) TEM analysis of defective InAs clusters and cascading dislocations in the upper InGaP cladding. (b) Evidence of stacking faults (SF) and antiphase boundaries (APBs) in the n-GaAs layer contributing to phase separation of lower InGaP.

and p-GaAs, and a reliable process has been developed for fabricating III-V devices in an oxide recess on Si. The InGaP cladding layers remain as the only clear obstacle to demonstrating the first electrically pumped lasers grown entirely by MOCVD SAH on Si. There are three possible paths forward to accomplish this goal: 1. continue optimizing the growth to achieve InGaP with no phase separation and low defect density, 2. use AlGaAs for the lower cladding and InGaP for the upper cladding like the planar Si devices from chapter 6 or, 3. use AlGaAs for both lower and upper cladding, with a sufficiently low temperature in the upper AlGaAs to avoid QD annealing. Of these, options 2 and 3 are the most promising for achieving lasing in the short term. InGaP is attractive, in theory, since it can be grown selectively and at low temperature, but based on the results in this chapter there is likely a considerable amount of optimization before upper and lower InGaP cladding can be grown reliably and without phase separation. Option 3 is the lowest risk in terms of actually demonstrating a working laser, and would require only minor changes to the fabrication process. Growth development of AlGaAs in recesses is ongoing and so far looks quite promising. Fig. 7.19(a) shows a new epitaxial design

with $Al_{0.4}GaAs$ cladding and InGaAs QWs. Fig. 7.19(b) shows a cross section of the as grown structure where some polycrystalline AlGaAs material was deposited on the oxide surface, which is the downside of using AlGaAs. However the polycrystal here is relatively thin (∼450 nm) and could easily be removed with dry or wet etching. Fig. 7.19(c) is a TEM image of the grown structure showing no phase separation in the AlGaAs layers, a very flat, smooth surface, and few dislocations.

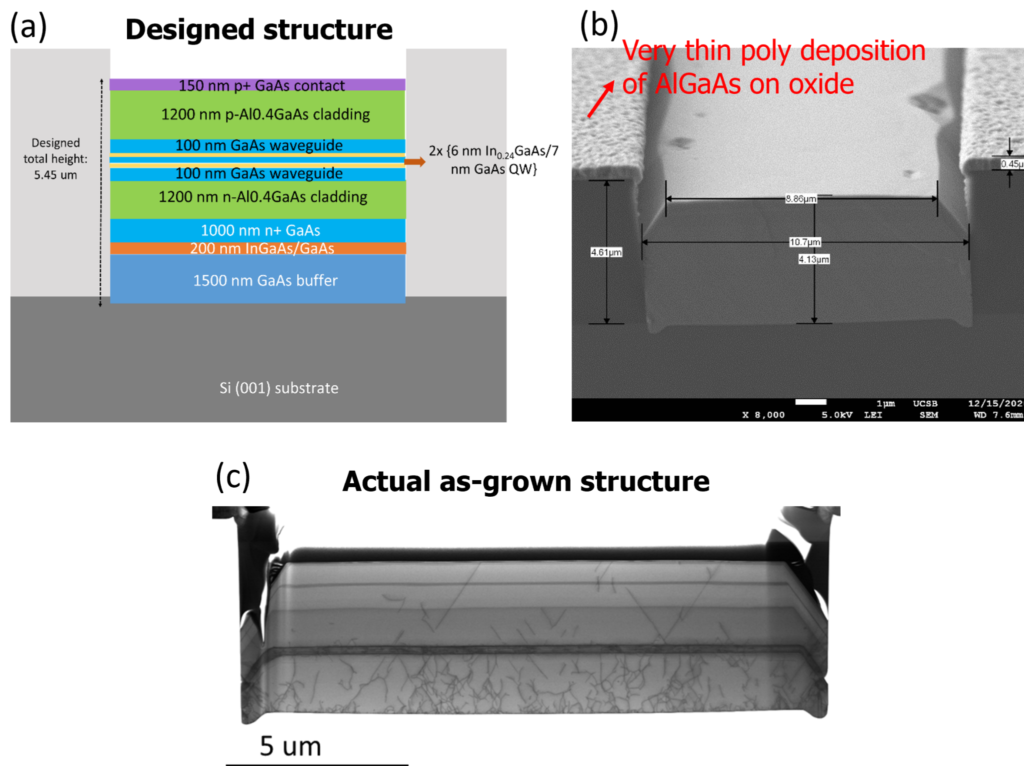

Figure 7.19: (a) Potential new epitaxy design with AlGaAs upper and lower cladding, (b) cross section of the grown structure showing some polycrystalline AlGaAs deposition on the oxide, and (c) TEM image of the structure showing very flat layers, with no phase separation and minimal dislocations.

The AlGaAs cladding approach seems promising from this initial demonstration. The next step would be to demonstrate QDs in the active region and see how they are affected by growth of the upper AlGaAs. Alternatively, InGaP could be used for the upper cladding only. Based on results from the short-loop fab, upper InGaP cladding does not

appear to negatively impact the IV curve. Because AlGaAs is not selective, this approach would require the sample to be removed from the chamber after growing the active region and the poly removed from the oxide surface before regrowing the upper InGaP cladding layer. In either case, some new fabrication process development would be necessary with the use of AlGaAs since the InGaP dry and wet etches would no longer be suitable. In particular, reliably etching down to the n-GaAs layer without etching through it would require careful timing of the etch, or development of a selective etch (either dry or wet). The fabrication in chapter 6 used a carefully timed dry etch to etch through the lower AlGaAs and into the contact layer. However, the challenge for SAH devices is that the growth rate is somewhat less predictable so the exact thickness of the layers may not be known. If the n-GaAs layer is thick enough, then there should be sufficient tolerance to over etch the AlGaAs, but there is still a risk of unintentionally etching through the contact layer.

7.5 Coupling to SiN Waveguides: Simulation

One of the advantages of the MOCVD SAH approach, as mentioned earlier, is the absence of a gap between the III-V and SiO_2 sidewall. Fig. 7.20 shows a cross-section of the III-V/SiO_2 interface after performing a FIB cut on the sample, demonstrating how the III-V material extends to the edge with no gap. Although there is some distortion, or "faceting", in the layers near the edge. In the image shown here, the distorted material is mostly within 2 µm of the edge.

One of the challenges of coupling from a III-V waveguide to SiN is the inherent mode mismatch. For a simple edge coupling scheme, maximizing coupling efficiency is a matter of maximizing the overlap between the fundamental modes, and making the gap between them as small as possible. The SiN waveguides in this template are comprised of two SiN

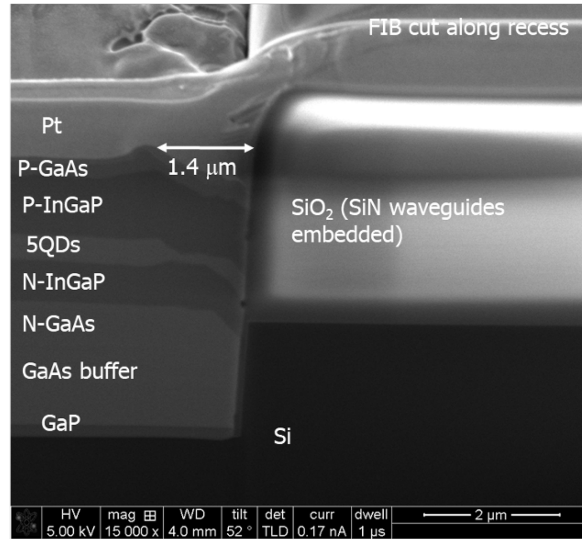

Figure 7.20: Zero-gap interface between III-V and SiO_2 for III-V laser stack grown by MOCVD SAH.

layers, each 220 nm thick and separated by 100 nm of SiO_2. The 2D optical mode profiles were simulated for a III-V ridge waveguide (GaAs with InGaP cladding), and for the SiN waveguide as shown in Fig. 7.21(a). Mode simulations were performed with the Ansys Lumerical Finite-Difference Eigenmode (FDE) solver. The III-V ridge in this case was 5 µm wide with a 500 nm thick GaAs waveguiding layer. The SiN width was swept from 0.2 µm to 6 µm wide. The loss due to mode mismatch was calculated for each SiN width to find the optimal dimension for coupling to the 5 µm ridge. The results from this sweep are shown in Fig. 7.21(b). The optimal SiN width is 4.8 µm, as shown in Fig. 7.21(a), and mode mismatch loss is about 0.5 dB. The loss shown here is due only to mode mismatch (i.e. different shapes, and reflections due to index difference) and assumes no gap between the waveguides, so this is really the upper limit in terms of possible coupling efficiency. In reality of course, even with the "zero-gap" interface shown in Fig. 7.20, the faceting near the edge will degrade the coupling efficiency. It is difficult to precisely simulate the effect of this faceting, however it can be approximated. In Lumerical finite difference time-domain (FDTD), rather than use an idealized geometry, the GaAs waveguide layer

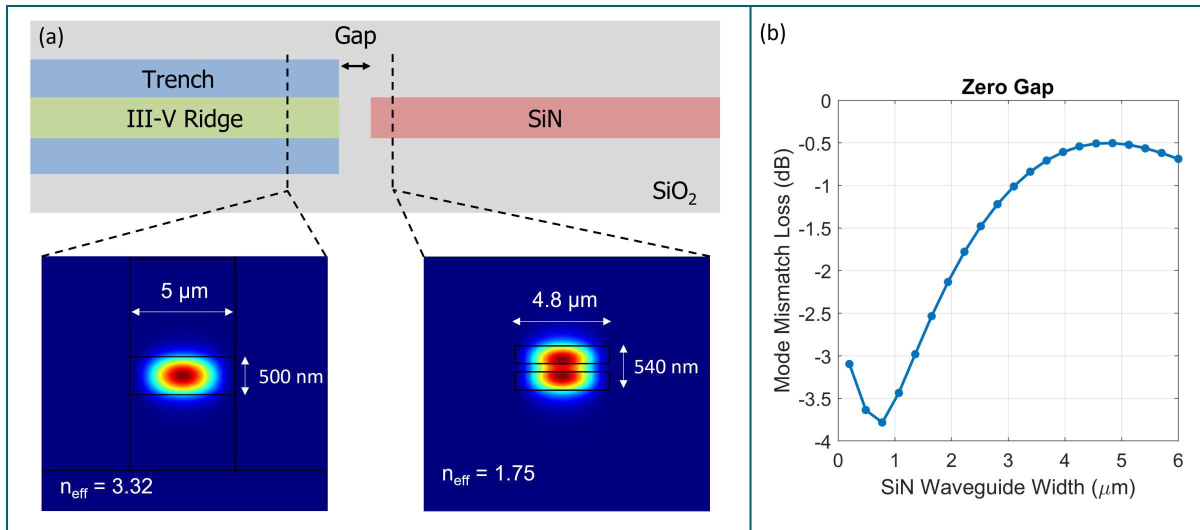

Figure 7.21: (a) Top-view schematic of III-V ridge in a recess coupling to SiN waveguides, with corresponding cross-sectional mode profiles shown below. (b) Simulated coupling loss due to mode mismatch versus SiN waveguide width. Simulation assumes zero gap between III-V and SiN.

was broken up into sections with different thickness in the final 2 µm of the ridge to mimic the true geometry. A side-view from the FDTD simulation geometry is shown in Fig. 7.22(a), and the simulated mode field profile is shown below for this geometry. The coupling efficiency of this geometry was compared to the case of a straight facet with a gap between the III-V and SiN by performing a sweep over different gap lengths. The blue curve in Fig. 7.22(b) shows results from the 3D FDTD sweeep of coupling efficiency versus gap distance, assuming the gap is filled with SiO_2 (an air gap would have worse performance due to lower index). In the zero-gap case, coupling efficiency is the same as predicted with the mode mismatch simulation. However, the efficiency drops rapidly with gap distance and at 3 µm the coupling efficiency is about 40%. The red '*' shows the coupling obtained from the 3D FDTD simulation from Fig. 7.21(a), with 2 µm of faceting at the interface, but no gap. Here the coupling efficiency is almost 70% whereas a 2 µm SiO_2 filled gap would result in coupling efficiency around 45%. This highlights the advantage of the SAH approach in terms of coupling efficiency, because, even with

some poor material quality near the edges, the efficiency is still significantly higher than having a gap between the waveguides.

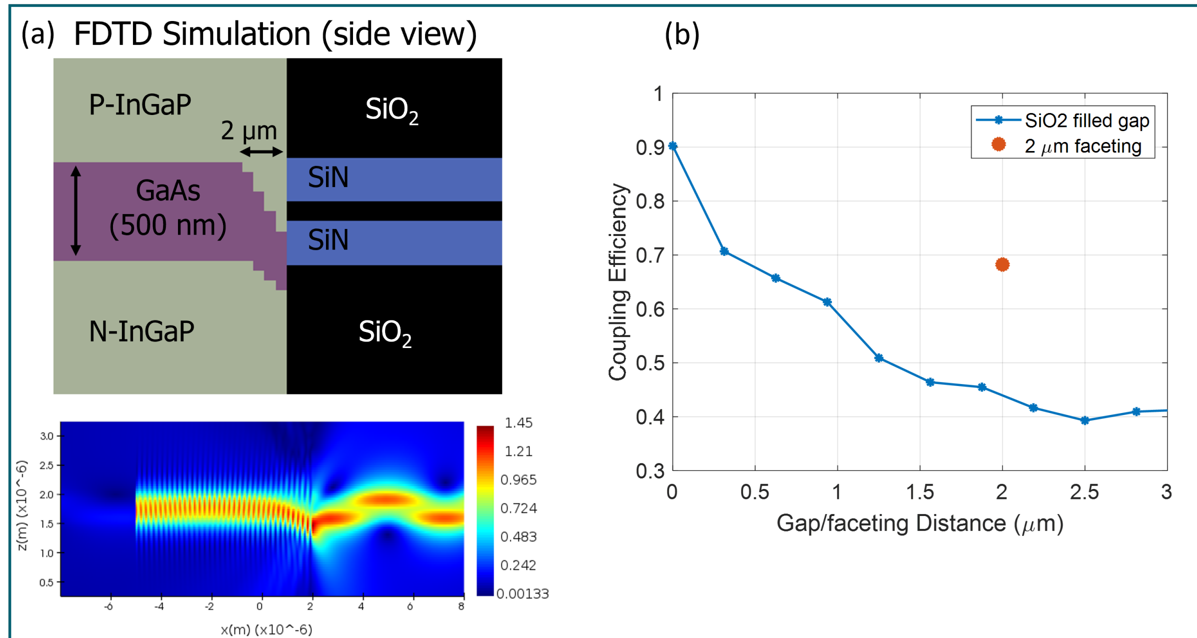

Figure 7.22: (a) 3D FDTD simulation to mimic faceting effects in the true geometry. (b) Sweep of coupling efficiency versus gap distance compared to results from (a).

Chapter 8

Summary and Future Work

The PIC market has been dominated by InP and SiPh in recent decades. InP because it provides a suitable platform for optical gain in the C- and O-bands for optical communication, and SiPh because it leverages state-of-the-art CMOS foundries to manufacture low loss, high performance passives in high volume at low cost. More recently, these two platforms have converged with various heterogeneous integration techniques employed to put InP gain chips on SiPh to get the best of both. However, InP is costly and its spectral range is limited to wavelengths above ~ 1.2 µm. While this is good for fiber based optical communication, other wavelengths are often necessary for specific applications. GaAs is less costly than InP and is ideal for wavelengths near 1 µm, and lasers in this range have been well researched. With the addition of QDs for gain, GaAs is also suitable for O-band lasers at 1.31 µm. Active-passive integration on native GaAs, analogous to InP PICs, is relatively immature, however. And heterogeneous integration of GaAs on Si is only a recent development compared to InP on Si. Direct heteroepitaxy of III-V materials on silicon has always been the long term goal, and for this GaAs-based lasers with QD gain appear to be the most promising. The work in this thesis demonstrated the utility of GaAs as an active-passive PIC platform, and explored monolithic integration of GaAs lasers on Si by MOCVD direct heteroepitaxy. This chapter provides a summary of the accomplishments in section 8.1. Ongoing and future work is then discussed in section

8.2.

8.1 Summary of Accomplishments

8.1.1 GaAs Active-Passive PIC Platform

A fully monolithic active-passive PIC platform on GaAs was demonstrated for operation near 1030 nm. This platform integrates active gain sections, with passive sections, while maintaining state-of-the-art Fabry-Perot (FP) laser performance for this material system. Extensive testing was done to extract various material parameters and gain characteristics. FP lasers demonstrated injection efficiency as high as 98%, and over 240 mW of CW output power from broad area devices. Threshold current density as low as 94 A/cm^2 was measured and transparency current density of 85.5 A/cm^2 was extracted from the gain characteristic. Efficient coupling between active and passive waveguide sections was demonstrated with active-passive FP lasers exhibiting performance comparable to all-active lasers. Although the passive waveguide loss was slightly high at around 4 cm^{-1}. These devices also had high characteristic temperature, $T_0 = 205\ K$. Widely tunable SGDBR lasers were fabricated on this PIC platform. Tunable laser chips were cleaved, AR coating applied to the facets, and mounted to AlN carriers for testing. Continuous tuning across a range of more than 20 nm was demonstrated and typical SMSR was greater than 30 dB across most of this range. Greater than 35 mW of output power was demonstrated from the front facets.

8.1.2 MOCVD Grown Lasers on Silicon

InAs/GaAs QD lasers monolithically grown on planar (001) silicon entirely by MOCVD were demonstrated. FP lasers with a 4 µm wide ridge exhibited CW output power of

more than 16 mW from each facet, and CW lasing up to 60 °C. Pulsed current operation of a broad area laser demonstrated greater than 200 mW total output power. This work demonstrated the feasibility of using MOCVD for growing QD lasers on silicon. Due to the high growth rates of MOCVD this is promising as a path towards large-scale monolithic integration of QD lasers for SiPh. Growth by selective area heteroepitaxy (SAH) and subsequent fabrication of laser structures in a trench was also demonstrated. The fabricated devices exhibited LED behavior, but electrically pumped lasing was not achieved. However significant progress was made towards the goal of achieving electrically pumped SAH lasers by MOCVD. Issues with the material were identified, specifically phase separation in the InGaP cladding, and some improvement was seen in the material quality. A significant amount of effort was also undertaken to develop the fabrication process for lasers in a trench. Ongoing work is underway to grow a similar structure with AlGaAs cladding, rather than InGaP.

8.2 Future Work

8.2.1 1030 nm GaAs PICs

Active-Passive Epitaxy Improvements

There are a few potential improvements that could be made to the active-passive epitaxy. One issue noted in chapter 3 was the high passive waveguide loss, which was attributed partly to free-carrier absorption due to overlap with the p-doped cladding. One option to reduce this is to increase the Al content in the upper cladding of the current structure to confine the mode more tightly in the waveguide. However, high Al content AlGaAs is more susceptible to oxidation which can degrade performance. Furthermore, if Al content is greater than around 50-60%, than BHF cannot be used at

any time during processing because it attacks AlGaAs with high Al. A better design would be to make the GaAs waveguide layer a little thicker, and use Al content around 40% for both upper and lower cladding. This is a good Al percentage for fabrication, and the thicker waveguide layer would allow the mode to spread out without overlapping the doped cladding layers as much. Another improvement for fabrication purposes could be to use InGaP as the grating layer. $HCl:H_3PO_4$ etches InGaP selective to GaAs/AlGaAs, so this could be used to etch the gratings and get an accurate and repeatable depth without relying on a carefully timed dry etch. An InGaP layer below the MQW layers could also serve as an etch stop for precisely removing active layers in the OQW design. The index difference between InGaP and GaAs would also allow the regrowth process to start with GaAs, rather than AlGaAs. This makes it possible to create a thicker GaAs waveguide without offsetting the MQW layers too far from the center, thus improving both QW confinement and active-passive coupling efficiency.

Wavelength Tuning

The analysis in chapter 5 determined that the primary tuning mechanism for the SGDBR lasers is likely thermal, due to self-heating with current injection. One possible conclusion, supported by literature, was that oxygen defects at the regrowth interface contributed to higher Shockley-Read-Hall (SRH) recombination, thus reducing total carrier density and increasing internal heating. Future work will utilize improved surface preparation before regrowth to minimize oxygen incorporation. The series resistance of the diode could also potentially be reduced by accessing the n-contact from the top of the epi, rather than backside contacting. This would reduce the effect of self-heating when tuning with current injection. Further testing is required to accurately determine the upper limit of the tuning speed for the lasers fabricated in this work.

8.2.2 SAH Lasers

AlGaAs Cladding

It was concluded in chapter 7 that phase separation in the InGaP cladding layers severely degraded device performance and prevented lasing. Although some improvement was observed with optimization, the InGaP quality did not improve sufficiently to demonstrate lasing. AlGaAs has been identified as an alternative cladding and early growth demonstrates are promising. Because AlGaAs does not grow selectively, some additional process development will be required to remove the polycrystal that forms on the oxide during growth. The etch recipes for forming the ridge will also need to be modified to accommodate AlGaAs.

Coupling to SiPh

The long-term goal of SAH lasers is monolithic integration with SiPh. Future work should focus on the design of efficient coupling schemes to demonstrate coupling from the III-V ridge to SiN waveguides. Some simulations were presented in chapter 7, however additional designs could be considered such as a multi-tip SiN coupler to improve misalignment tolerance. The coupler design is only the first step. Once this is accomplished, additional work should take advantage of the whole suite of passive devices available in the AIM photonics PDK, to demonstrate truly monolithic III-V on Si PICs.

Bibliography

[1] S. E. Miller, *Integrated optics: An introduction*, *Bell Syst. Tech. J.* **48** (September, 1969) 2059–2069.

[2] Z. I. Alferov, *Alas-gaas heterojunction injection lasers with a low room-temperature threshold*, *Sov. Phys. Semicond.* **3** (1970) 1107–1110.

[3] Z. Alferov, *Double heterostructure lasers: early days and future perspectives*, *IEEE Journal of Selected Topics in Quantum Electronics* **6** (2000), no. 6 832–840.

[4] M. Smit, K. Williams, and J. van der Tol, *Past, present, and future of inp-based photonic integration*, *APL Photonics* **4** (2019), no. 5 050901.

[5] L. A. Coldren, P. A. Verrinder, and J. Klamkin, *A review of photonic systems-on-chip enabled by widely tunable lasers*, *IEEE Journal of Quantum Electronics* **58** (2022), no. 4 1–10.

[6] F. Kish, V. Lal, P. Evans, S. W. Corzine, M. Ziari, T. Butrie, M. Reffle, H.-S. Tsai, A. Dentai, J. Pleumeekers, M. Missey, M. Fisher, S. Murthy, R. Salvatore, P. Samra, S. Demars, N. Kim, A. James, A. Hosseini, P. Studenkov, M. Lauermann, R. Going, M. Lu, J. Zhang, J. Tang, J. Bostak, T. Vallaitis, M. Kuntz, D. Pavinski, A. Karanicolas, B. Behnia, D. Engel, O. Khayam, N. Modi, M. R. Chitgarha, P. Mertz, W. Ko, R. Maher, J. Osenbach, J. T. Rahn, H. Sun, K.-T. Wu, M. Mitchell, and D. Welch, *System-on-chip photonic integrated circuits*, *IEEE Journal of Selected Topics in Quantum Electronics* **24** (2018), no. 1 1–20.

[7] F. Kish, R. Nagarajan, D. Welch, P. Evans, J. Rossi, J. Pleumeekers, A. Dentai, M. Kato, S. Corzine, R. Muthiah, M. Ziari, R. Schneider, M. Reffle, T. Butrie, D. Lambert, M. Missey, V. Lal, M. Fisher, S. Murthy, R. Salvatore, S. Demars, A. James, and C. Joyner, *From visible light-emitting diodes to large-scale iii–v photonic integrated circuits*, *Proceedings of the IEEE* **101** (2013), no. 10 2255–2270.

[8] G. Gilardi and M. K. Smit, *Generic inp-based integration technology: Present and prospects (invited review)*, *Progress In Electromagnetics Research* **147** (2014) 23–35.

[9] G. E. Hoefler, Y. Zhou, M. Anagnosti, A. Bhardwaj, P. Abolghasem, A. James, S. Luna, P. Debackere, A. Dentai, T. Vallaitis, *et. al.*, *Foundry development of system-on-chip inp-based photonic integrated circuits*, *IEEE Journal of Selected Topics in Quantum Electronics* **25** (2019), no. 5 1–17.

[10] K. Williams, E. Bente, D. Heiss, Y. Jiao, K. Ławniczuk, X. Leijtens, J. Van der Tol, and M. Smit, *Inp photonic circuits using generic integration*, *Photonics Research* **3** (2015), no. 5 B60–B68.

[11] C. Doerr, *Silicon photonic integration in telecommunications*, *Frontiers in Physics* **3** (2015).

[12] T. Shi, T.-I. Su, N. Zhang, C. yin Hong, and D. Pan, *Silicon photonics platform for 400g data center applications*, in *Optical Fiber Communication Conference*, p. M3F.4, Optica Publishing Group, 2018.

[13] T. Komljenovic, M. Davenport, J. Hulme, A. Y. Liu, C. T. Santis, A. Spott, S. Srinivasan, E. J. Stanton, C. Zhang, and J. E. Bowers, *Heterogeneous silicon photonic integrated circuits*, *Journal of Lightwave Technology* **34** (1, 2016) 20–35.

[14] A. W. Fang, H. Park, O. Cohen, R. Jones, M. J. Paniccia, and J. E. Bowers, *Electrically pumped hybrid algainas-silicon evanescent laser*, *Opt. Express* **14** (Oct, 2006) 9203–9210.

[15] B. Song, C. Stagarescu, S. Ristic, A. Behfar, and J. Klamkin, *3d integrated hybrid silicon laser*, *Optics Express* **24** (2016) 10435–10444.

[16] J. Zhang, G. Muliuk, J. Juvert, S. Kumari, J. Goyvaerts, B. Haq, C. O. D. Beeck, B. Kuyken, G. Morthier, D. V. Thourhout, R. Baets, G. Lepage, P. Verheyen, J. V. Campenhout, A. Gocalinska, J. O'Callaghan, E. Pelucchi, K. Thomas, B. Corbett, A. J. Trindade, and G. Roelkens, *Iii-v-on-si photonic integrated circuits realized using micro-transfer-printing*, *APL Photonics* **4** (2019).

[17] C. Xiang, W. Jin, D. Huang, M. A. Tran, J. Guo, Y. Wan, W. Xie, G. Kurczveil, A. M. Netherton, D. Liang, H. Rong, and J. E. Bowers, *High-performance silicon photonics using heterogeneous integration*, *IEEE Journal of Selected Topics in Quantum Electronics* **28** (2022) 1–15.

[18] S. Keyvaninia, G. Roelkens, D. V. Thourhout, C. Jany, M. Lamponi, A. L. Liepvre, F. Lelarge, D. Make, G.-H. Duan, D. Bordel, and J.-M. Fedeli, *Demonstration of a heterogeneously integrated iii-v/soi single wavelength tunable laser*, *Opt. Express* **21** (Feb, 2013) 3784–3792.

[19] B. Snyder, B. Corbett, and P. O'Brien, *Hybrid integration of the wavelength-tunable laser with a silicon photonic integrated circuit*, *J. Lightwave Technol.* **31** (Dec, 2013) 3934–3942.

[20] N. Margalit, C. Xiang, S. M. Bowers, A. Bjorlin, R. Blum, and J. E. Bowers, *Perspective on the future of silicon photonics and electronics*, *Applied Physics Letters* **118** (2021).

[21] M. Blaicher, M. R. Billah, J. Kemal, T. Hoose, P. Marin-Palomo, A. Hofmann, Y. Kutuvantavida, C. Kieninger, P.-I. Dietrich, M. Lauermann, *et. al.*, *Hybrid multi-chip assembly of optical communication engines by in situ 3d nano-lithography*, *Light: Science & Applications* **9** (2020), no. 1 71.

[22] R. Jones, P. Doussiere, J. B. Driscoll, W. Lin, H. Yu, Y. Akulova, T. Komljenovic, and J. E. Bowers, *Heterogeneously integrated inpsilicon photonics: Fabricating fully functional transceivers*, *IEEE Nanotechnology Magazine* **13** (2019), no. 2 17–26.

[23] A. Liu, P. Wolf, J. A. Lott, and D. Bimberg, *Vertical-cavity surface-emitting lasers for data communication and sensing*, *Photon. Res.* **7** (Feb, 2019) 121–136.

[24] J. C. Norman, R. P. Mirin, and J. E. Bowers, *Quantum dot lasers—history and future prospects*, *Journal of Vacuum Science & Technology A* **39** (2021), no. 2.

[25] S. Mudumba, S. de Alba, R. Romero, C. Cherwien, A. Wu, J. Wang, M. A. Gleeson, M. Iqbal, and R. W. Burlingame, *Photonic ring resonance is a versatile platform for performing multiplex immunoassays in real time*, *Journal of Immunological Methods* **448** (2017) 34–43.

[26] S. Rumley, D. Nikolova, R. Hendry, Q. Li, D. Calhoun, and K. Bergman, *Silicon photonics for exascale systems*, *J. Lightwave Technol.* **33** (Feb, 2015) 547–562.

[27] Y. Shen, N. C. Harris, S. Skirlo, M. Prabhu, T. Baehr-Jones, M. Hochberg, X. Sun, S. Zhao, H. Larochelle, D. Englund, *et. al.*, *Deep learning with coherent nanophotonic circuits*, *Nature photonics* **11** (2017), no. 7 441–446.

[28] L. E. Srouji, A. Krishnan, R. Ravichandran, Y. Lee, M. On, X. Xiao, and S. J. B. Yoo, *Photonic and optoelectronic neuromorphic computing*, *APL Photonics* **7** (2022).

[29] H.-T. Peng, M. A. Nahmias, T. F. de Lima, A. N. Tait, and B. J. Shastri, *Neuromorphic photonic integrated circuits*, *IEEE Journal of Selected Topics in Quantum Electronics* **24** (2018), no. 6 1–15.

[30] J. Sun, E. Timurdogan, A. Yaacobi, Z. Su, E. S. Hosseini, D. B. Cole, and M. R. Watts, *Large-scale silicon photonic circuits for optical phased arrays*, *IEEE Journal of Selected Topics in Quantum Electronics* **20** (2014), no. 4 264–278.

[31] M. Nickerson, B. Song, J. Brookhyser, G. Erwin, J. Kleinert, and J. Klamkin, *Gallium arsenide optical phased array photonic integrated circuit*, *arXiv preprint arXiv:2304.03417* (2023).

[32] J. Fridlander, F. Sang, V. Rosborough, F. Gambini, S. T. Šuran-Brunelli, J. R. Chen, K. Numata, M. Stephen, L. A. Coldren, and J. Klamkin, *Dual laser indium phosphide photonic integrated circuit for integrated path differential absorption lidar*, *IEEE Journal of Selected Topics in Quantum Electronics* **28** (2021), no. 1: Semiconductor Lasers 1–8.

[33] B. J. Isaac, B. Song, S. Pinna, L. A. Coldren, and J. Klamkin, *Indium phosphide photonic integrated circuit transceiver for fmcw lidar*, *IEEE Journal of Selected Topics in Quantum Electronics* **25** (2019) 1–7.

[34] P. Verrinder, L. Wang, F. Sang, J. Fridlander, V. Rosborough, M. Nickerson, G. Yang, M. Stephen, L. Coldren, and J. Klamkin, *Sgdbr tunable laser on gallium arsenide for 1030 nm lidar applications*, in *2021 27th International Semiconductor Laser Conference (ISLC)*, pp. 1–2, IEEE, 2021.

[35] P. Verrinder, L. Wang, J. Fridlander, F. Sang, V. Rosborough, M. Nickerson, G. Yang, M. Stephen, L. Coldren, and J. Klamkin, *Gallium arsenide photonic integrated circuit platform for tunable laser applications*, *IEEE Journal of Selected Topics in Quantum Electronics* **28** (2022).

[36] A. W. Yu, M. A. Krainak, D. J. Harding, J. B. Abshire, X. Sun, L. Ramos-Izquierdo, J. Cavanaugh, S. Valett, T. Winkert, M. Plants, C. Kirchner, B. Kamamia, R. Faulkner, P. Dogoda, W. Hasselbrack, and T. Filemyr, *A 16-beam non-scanning swath mapping laser altimeter instrument*, in *Solid State Lasers XXII: Technology and Devices* (W. A. Clarkson and R. Shori, eds.), vol. 8599, p. 85990P, International Society for Optics and Photonics, SPIE, 2013.

[37] G. R. Allan, J. B. Abshire, H. Riris, J. Mao, W. E. Hasselbrack, K. Numata, J. Chen, R. Kawa, M. Rodriguez, and M. Stephen, *Lidar measurements of co2 column concentrations in the arctic region of north america from the ascends 2017 airborne campaign*, in *Lidar Remote Sensing for Environmental Monitoring XVI*, vol. 10779, pp. 28–33, SPIE, 2018.

[38] J. B. Abshire, A. K. Ramanathan, H. Riris, G. R. Allan, X. Sun, W. E. Hasselbrack, J. Mao, S. Wu, J. Chen, K. Numata, *et. al.*, *Airborne measurements of co2 column concentrations made with a pulsed ipda lidar using a multiple-wavelength-locked laser and hgcdte apd detector*, *Atmospheric Measurement Techniques* **11** (2018), no. 4 2001–2025.

[39] W. Abdalati, H. J. Zwally, R. Bindschadler, B. Csatho, S. L. Farrell, H. A. Fricker, D. Harding, R. Kwok, M. Lefsky, T. Markus, A. Marshak, T. Neumann, S. Palm, B. Schutz, B. Smith, J. Spinhirne, and C. Webb, *The icesat-2 laser altimetry mission*, *Proceedings of the IEEE* **98** (2010), no. 5 735–751.

[40] J. Coleman, *Strained-layer ingaas quantum-well heterostructure lasers*, *IEEE Journal of Selected Topics in Quantum Electronics* **6** (2000), no. 6 1008–1013.

[41] M. A. Tran, C. Zhang, T. J. Morin, L. Chang, S. Barik, Z. Yuan, W. Lee, G. Kim, A. Malik, Z. Zhang, *et. al.*, *Extending the spectrum of fully integrated photonics to submicrometre wavelengths*, *Nature* **610** (2022), no. 7930 54–60.

[42] H. Park, C. Zhang, M. A. Tran, and T. Komljenovic, *Heterogeneous silicon nitride photonics*, *Optica* **7** (2020), no. 4 336–337.

[43] LightCounting, "Silicon Photonics: Linear Drive, Pluggable, and Co-Packaged Optics." `https://www.lightcounting.com/newsletter/may-2023-silicon-photonics-linear-drive-pluggable-and-co-packaged-optics-203`, May, 2023. Accessed on July 26, 2023.

[44] A. Honardoost, K. Abdelsalam, and S. Fathpour, *Rejuvenating a versatile photonic material: thin-film lithium niobate*, *Laser & Photonics Reviews* **14** (2020), no. 9 2000088.

[45] T. Ishikawa and J. E. Bowers, *Band lineup and in-plane effective mass of ingaasp or ingaalas on inp strained-layer quantum well*, *IEEE Journal of Quantum Electronics* **30** (1994), no. 2 562–570.

[46] E. H. Li, *Material parameters of ingaasp and inalgaas systems for use in quantum well structures at low and room temperatures*, *Physica E: Low-dimensional systems and Nanostructures* **5** (2000), no. 4 215–273.

[47] S. Arafin and L. A. Coldren, *Advanced inp photonic integrated circuits for communication and sensing*, *IEEE Journal of Selected Topics in Quantum Electronics* **24** (2017), no. 1 1–12.

[48] J. C. Norman, D. Jung, Y. Wan, and J. E. Bowers, *Perspective: The future of quantum dot photonic integrated circuits*, *APL photonics* **3** (2018), no. 3 030901.

[49] M. Smit, X. Leijtens, H. Ambrosius, E. Bente, J. Van der Tol, B. Smalbrugge, T. De Vries, E.-J. Geluk, J. Bolk, R. Van Veldhoven, *et. al.*, *An introduction to inp-based generic integration technology*, *Semiconductor Science and Technology* **29** (2014), no. 8 083001.

[50] S. Manipatruni, K. Preston, L. Chen, and M. Lipson, *Ultra-low voltage, ultra-small mode volume silicon microring modulator*, *Optics express* **18** (2010), no. 17 18235–18242.

[51] M. A. Tran, D. Huang, T. Komljenovic, J. Peters, A. Malik, and J. E. Bowers, *Ultra-low-loss silicon waveguides for heterogeneously integrated silicon/iii-v photonics*, *Applied Sciences* **8** (2018), no. 7 1139.

[52] W. Jin, Q.-F. Yang, L. Chang, B. Shen, H. Wang, M. A. Leal, L. Wu, M. Gao, A. Feshali, M. Paniccia, *et. al.*, *Hertz-linewidth semiconductor lasers using cmos-ready ultra-high-q microresonators*, *Nature Photonics* **15** (2021), no. 5 346–353.

[53] J. F. Bauters, M. J. Heck, D. D. John, J. S. Barton, C. M. Bruinink, A. Leinse, R. G. Heideman, D. J. Blumenthal, and J. E. Bowers, *Planar waveguides with less than 0.1 db/m propagation loss fabricated with wafer bonding*, *Optics express* **19** (2011), no. 24 24090–24101.

[54] N. M. Fahrenkopf, C. McDonough, G. L. Leake, Z. Su, E. Timurdogan, and D. D. Coolbaugh, *The aim photonics mpw: A highly accessible cutting edge technology for rapid prototyping of photonic integrated circuits*, *IEEE Journal of Selected Topics in Quantum Electronics* **25** (2019), no. 5 1–6.

[55] T. Aalto, M. Cherchi, M. Harjanne, S. Bhat, P. Heimala, F. Sun, M. Kapulainen, T. Hassinen, and T. Vehmas, *Open-access 3-μm soi waveguide platform for dense photonic integrated circuits*, *IEEE Journal of Selected Topics in Quantum Electronics* **25** (2019), no. 5 1–9.

[56] K. Giewont, K. Nummy, F. A. Anderson, J. Ayala, T. Barwicz, Y. Bian, K. K. Dezfulian, D. M. Gill, T. Houghton, S. Hu, *et. al.*, *300-mm monolithic silicon photonics foundry technology*, *IEEE Journal of Selected Topics in Quantum Electronics* **25** (2019), no. 5 1–11.

[57] "The silicon photonics process design kit." `https://www.analogphotonics.com/product/the-silicon-photonics-process-design-kit/`, 2023. Accessed on July 26, 2023.

[58] Y. Wan, J. E. Bowers, C. Shang, J. Norman, B. Shi, Q. Li, N. Collins, M. Dumont, K. M. Lau, and A. C. Gossard, *Low threshold quantum dot lasers directly grown on unpatterned quasi-nominal (001) si*, *IEEE Journal of Selected Topics in Quantum Electronics* **26** (2020).

[59] M. Liao, S. Chen, J.-S. Park, A. Seeds, and H. Liu, *Iii–v quantum-dot lasers monolithically grown on silicon*, *Semiconductor Science and Technology* **33** (2018), no. 12 123002.

[60] B. Shi, S. Zhu, B. Song, D. Hu, T. Vo, J. Herman, D. L. Harame, J. Klamkin, *et. al.*, *Selective area heteroepitaxy of quantum dot lasers on nano-v-grooved silicon*, in *Integrated Photonics Research, Silicon and Nanophotonics*, pp. IW2B–7, Optica Publishing Group, 2022.

[61] S. Zhu, B. Shi, B. Song, D. Hu, and J. Klamkin, *Iii-v lasers on silicon by selective area heteroepitaxy*, in *CLEO: Science and Innovations*, pp. SF2G–4, Optica Publishing Group, 2022.

[62] H. David, H. Marco, B. Rudiger, *et. al.*, *Dramatic advances in direct diode lasers*, in *SPIE*, vol. 7583, pp. 75830B–1, 2010.

[63] P. O. Leisher, J. Campbell, M. Labrecque, K. McClune, T. Cooper, E. Burke, F. Talantov, D. Renner, L. Johansson, and M. Mashanovitch, *¿ 3w diffraction-limited 1550 nm diode laser amplifiers for lidar*, in *Components and Packaging for Laser Systems VIII*, vol. 11982, pp. 29–34, SPIE, 2022.

[64] P. Crump, G. Erbert, H. Wenzel, C. Frevert, C. M. Schultz, K.-H. Hasler, R. Staske, B. Sumpf, A. Maaßdorf, F. Bugge, S. Knigge, and G. Tränkle, *Efficient high-power laser diodes*, *IEEE Journal of Selected Topics in Quantum Electronics* **19** (2013), no. 4 1501211–1501211.

[65] S. Arslan, G. Erbert, A. Boni, M. Wilkens, A. Maaßdorf, J. Fricke, A. Ginolas, and P. Crump, *Approaches for higher power in gaas-based broad area diode lasers*, in *2019 IEEE High Power Diode Lasers and Systems Conference (HPD)*, pp. 51–52, 2019.

[66] A. Boni, P. Della Casa, D. Martin, and P. Crump, *Efficiency optimization of high-power gaas lasers by balancing confinement and threshold*, in *2021 27th International Semiconductor Laser Conference (ISLC)*, pp. 1–2, 2021.

[67] P. Crump and R. Martinsen, *Advances in high efficiency diode laser pump sources suitable for pumping nd: Yag systems*, in *Quantum Electronics and Laser Science Conference*, p. JWD5, Optica Publishing Group, 2007.

[68] R. Feeler, J. Junghans, and E. Stephens, *Low-cost diode arrays for the life project*, in *High Power Lasers for Fusion Research*, vol. 7916, pp. 72–78, SPIE, 2011.

[69] J. Sethian, D. Colombant, J. Giuliani, R. Lehmberg, M. Myers, S. Obenschain, A. Schmitt, J. Weaver, M. Wolford, F. Hegeler, *et. al.*, *The science and technologies for fusion energy with lasers and direct-drive targets*, *IEEE Transactions on plasma science* **38** (2010), no. 4 690–703.

[70] "Lumentum." `https://www.lumentum.com/en`, 2023. Accessed on July 26, 2023.

[71] H.-T. Cheng, Y.-C. Yang, T.-H. Liu, and C.-H. Wu, *Recent advances in 850 nm vcsels for high-speed interconnects*, *Photonics* **9** (2022), no. 2.

[72] H. Li, P. Wolf, P. Moser, G. Larisch, J. A. Lott, and D. Bimberg, *Vertical-cavity surface-emitting lasers for optical interconnects*, *SPIE Newsroom* **25** (2014) 126103.

[73] F. Koyama, *Advances and new functions of vcsel photonics*, *Optical Review* **21** (2014) 893–904.

[74] K. Nishi, K. Takemasa, M. Sugawara, and Y. Arakawa, *Development of quantum dot lasers for data-com and silicon photonics applications*, *IEEE Journal of Selected Topics in Quantum Electronics* **23** (2017), no. 6 1–7.

[75] L. Wang, E. Hughes, C. Zhang, J. Bowers, and J. Klamkin, *Reliable quantum dot laser grown by mocvd*, in *Integrated Photonics Research, Silicon and Nanophotonics*, pp. IW2B–1, Optica Publishing Group, 2022.

[76] W. Y. Anthony, M. A. Stephen, S. X. Li, G. B. Shaw, A. Seas, E. Dowdye, E. Troupaki, P. Liiva, D. Poulios, and K. Mascetti, *Space laser transmitter development for icesat-2 mission*, in *Solid State Lasers XIX: Technology and Devices*, vol. 7578, pp. 64–74, SPIE, 2010.

[77] S. Lee, R. Ramaswamy, and V. Sundaram, *Analysis and design of high-speed high-efficiency gaas-algaas double-heterostructure waveguide phase modulator*, *IEEE Journal of Quantum Electronics* **27** (1991), no. 3 726–736.

[78] J. Mendoza-Alvarez, L. Coldren, A. Alping, R. Yan, T. Hausken, K. Lee, and K. Pedrotti, *Analysis of depletion edge translation lightwave modulators*, *Journal of Lightwave Technology* **6** (1988), no. 6 793–808.

[79] "Tower semiconductor announces world's first heterogeneous integration of quantum dot lasers on its popular sipho foundry platform ph18." `https://www.globenewswire.com/en/news-release/2023/03/02/2619018/0/en/Tower-Semiconductor-Announces-World-s-First-Heterogeneous-Integration-of-Quantu` `html`, 2023. Accessed on July 26, 2023.

[80] L. A. Coldren, S. W. Corzine, and M. L. Mashanovitch, *Diode lasers and photonic integrated circuits*. John Wiley & Sons, 2012.

[81] F. Xia, V. M. Menon, and S. R. Forrest, *Photonic integration using asymmetric twin-waveguide (atg) technology: part i-concepts and theory*, *IEEE Journal of selected topics in quantum electronics* **11** (2005), no. 1 17–29.

[82] E. J. Skogen, J. S. Barton, S. P. Denbaars, and L. A. Coldren, *A quantum-well-intermixing process for wavelength-agile photonic integrated circuits*, *IEEE Journal of Selected Topics in Quantum Electronics* **8** (2002), no. 4 863–869.

[83] N. Zia, S.-P. Ojanen, J. Viheriala, E. Koivusalo, J. Hilska, H. Tuorila, and M. Guina, *Widely tunable 2 μm hybrid laser using gasb semiconductor optical amplifiers and a si 3 n 4 photonics integrated reflector*, *Optics Letters* **48** (2023), no. 5 1319–1322.

[84] B. Shi, H. Zhao, L. Wang, B. Song, S. T. S. Brunelli, and J. Klamkin, *Continuous-wave electrically pumped 1550 nm lasers epitaxially grown on on-axis (001) silicon*, *Optica* **6** (2019), no. 12 1507–1514.

[85] B. Shi, L. Wang, A. A. Taylor, S. Suran Brunelli, H. Zhao, B. Song, and J. Klamkin, *Mocvd grown low dislocation density gaas-on-v-groove patterned (001) si for 1.3 μ m quantum dot laser applications*, *Applied Physics Letters* **114** (2019), no. 17 172102.

[86] Q. Li and K. M. Lau, *Epitaxial growth of highly mismatched iii-v materials on (001) silicon for electronics and optoelectronics*, *Progress in Crystal Growth and Characterization of Materials* **63** (2017), no. 4 105–120.

[87] L. Wang, *High Performance MOCVD Grown QD Laser on GaAs and Si*. University of California, Santa Barbara, 2023.

[88] I. Németh, B. Kunert, W. Stolz, and K. Volz, *Heteroepitaxy of gap on si: Correlation of morphology, anti-phase-domain structure and movpe growth conditions*, *Journal of Crystal Growth* **310** (2008), no. 7-9 1595–1601.

[89] K. Volz, A. Beyer, W. Witte, J. Ohlmann, I. Németh, B. Kunert, and W. Stolz, *Gap-nucleation on exact si (001) substrates for iii/v device integration*, *Journal of Crystal Growth* **315** (2011), no. 1 37–47. 15th International Conference on Metalorganic Vapor Phase Epitaxy (ICMOVPE-XV).

[90] A. Beyer, A. Stegmüller, J. O. Oelerich, K. Jandieri, K. Werner, G. Mette, W. Stolz, S. D. Baranovskii, R. Tonner, and K. Volz, *Pyramidal structure formation at the interface between iii/v semiconductors and silicon*, *Chemistry of Materials* **28** (2016), no. 10 3265–3275, [https://doi.org/10.1021/acs.chemmater.5b04896].

[91] A. Beyer, B. Haas, K. Gries, K. Werner, M. Luysberg, W. Stolz, and K. Volz, *Atomic structure of (110) anti-phase boundaries in gap on si (001)*, *Applied Physics Letters* **103** (2013), no. 3.

[92] C. Shang, M. R. Begley, D. S. Gianola, and J. E. Bowers, *Crack propagation in low dislocation density quantum dot lasers epitaxially grown on si*, *APL Materials* **10** (2022), no. 1.

[93] K. Feng, C. Shang, E. Hughes, A. Clark, R. Koscica, P. Ludewig, D. Harame, and J. Bowers, *Quantum dot lasers directly grown on 300 mm si wafers: Planar and in-pocket*, *Photonics* **10** (2023), no. 5.

[94] C. Shang, K. Feng, E. T. Hughes, A. Clark, M. Debnath, R. Koscica, G. Leake, J. Herman, D. Harame, P. Ludewig, *et. al.*, *Electrically pumped quantum-dot lasers grown on 300 mm patterned si photonic wafers*, *Light: Science & Applications* **11** (2022), no. 1 299.

[95] P. Doussiere, *High power lasers on inp substrates*, in *IEEE Photonic Society 24th Annual Meeting*, pp. 674–675, IEEE, 2011.

[96] C. Xiang, J. Guo, W. Jin, L. Wu, J. Peters, W. Xie, L. Chang, B. Shen, H. Wang, Q.-F. Yang, *et. al.*, *High-performance lasers for fully integrated silicon nitride photonics*, *Nature communications* **12** (2021), no. 1 6650.

[97] Y. T. Byun, K. H. Park, S. H. Kim, S. S. Choi, and T. K. Lim, *Single-mode gaas/algaas w waveguides with a low propagation loss*, *Applied optics* **35** (1996), no. 6 928–933.

[98] M. A. Krainak, X. Sun, G. Yang, and W. Lu, *Comparison of linear-mode avalanche photodiode lidar receivers for use at one-micron wavelength*, in *Advanced Photon Counting Techniques IV*, vol. 7681, pp. 226–238, SPIE, 2010.

[99] V. Jayaraman, Z. M. Chuang, and L. A. Coldren, *Theory, design, and performance of extended tuning range semiconductor lasers with sampled gratings*, *IEEE Journal of Quantum Electronics* **29** (1993) 1824–1834. 18.

[100] H. Zhao, S. Pinna, B. Song, L. Megalini, S. T. S. Brunelli, L. A. Coldren, and J. Klamkin, *Indium phosphide photonic integrated circuits for free space optical links*, *IEEE Journal of Selected Topics in Quantum Electronics* **24** (2018) 1–6.

[101] M. Tawfieq, H. Wenzel, P. Della Casa, O. Brox, A. Ginolas, P. Ressel, D. Feise, A. Knigge, M. Weyers, B. Sumpf, *et. al.*, *High-power sampled-grating-based master oscillator power amplifier system with 23.5 nm wavelength tuning around 970 nm*, *Applied Optics* **57** (2018), no. 29 8680–8685.

[102] O. Brox, H. Wenzel, P. Della Case, M. Tawfieq, B. Sumpf, M. Weyers, and A. Knigge, *Reflectors and tuning elements for widely-tunable gaas-based sampled grating dbr lasers*, in *Novel In-Plane Semiconductor Lasers XVII*, vol. 10553, pp. 136–144, SPIE, 2018.

[103] A. J. Martino, J. Cavanaugh, A. Gibbons, J. E. Golder, A. Ivanoff, P. Jester, N. Kurtz, T. Neumann, A. Pingel, and C. Swenson, *Icesat-2/atlas at 4 years: instrument performance and projected life*, in *Advanced Photon Counting Techniques XVII*, vol. 12512, pp. 47–61, SPIE, 2023.

[104] J. G. Smith, L. Ramos-Izquierdo, A. Stockham, and S. Scott, *Diffractive optics for moon topography mapping*, in *Micro (MEMS) and Nanotechnologies for Space Applications*, vol. 6223, pp. 15–24, SPIE, 2006.

[105] L. A. Coldren, G. A. Fish, Y. Akulova, J. Barton, L. Johansson, and C. Coldren, *Tunable semiconductor lasers: A tutorial*, *Journal of Lightwave Technology* **22** (2004), no. 1 193.

[106] T. Koch, U. Koren, R. Gnall, C. Burrus, and B. Miller, *Continuously tunable 1-5&mu m multiple-quantum-well galnas/galnasp distributed-bragg-reflector lasers*, *Electronics Letters* **24** (1988), no. 23 1431–1433.

[107] N. H. Zhu, J. M. Wen, H. S. San, H. P. Huang, L. J. Zhao, and W. Wang, *Improved optical heterodyne methods for measuring frequency responses of photodetectors*, *IEEE journal of quantum electronics* **42** (2006), no. 3 241–248.

[108] "RefractiveIndex.info - GaAs (Gallium Arsenide)." `https://refractiveindex.info/?shelf=main&book=GaAs&page=Papatryfonos`. Accessed on July 18, 2023.

[109] B. Bennett, R. Soref, and J. Del Alamo, *Carrier-induced change in refractive index of inp, gaas and ingaasp*, *IEEE Journal of Quantum Electronics* **26** (1990), no. 1 113–122.

[110] J. Mendoza-Alvarez, L. Coldren, A. Alping, R. Yan, T. Hausken, K. Lee, and K. Pedrotti, *Analysis of depletion edge translation lightwave modulators*, *Journal of lightwave technology* **6** (1988), no. 6 793–808.

[111] N. Nilsson, *Empirical approximations for the fermi energy in a semiconductor with parabolic bands*, *Applied Physics Letters* **33** (1978), no. 7 653–654.

[112] C. Henry, R. Logan, and K. Bertness, *Spectral dependence of the change in refractive index due to carrier injection in gaas lasers*, *Journal of Applied Physics* **52** (1981), no. 7 4457–4461.

[113] A. Alping and L. Coldren, *Electrorefraction in gaas and ingaasp and its application to phase modulators*, *Journal of applied physics* **61** (1987), no. 7 2430–2433.

[114] M. Nickerson, B. Song, L. Wang, P. Verrinder, J. Brookhyser, G. Erwin, J. Kleinert, and J. Klamkin, *Broadband and low residual amplitude modulation phase modulator arrays for optical beamsteering applications*, in *CLEO: Science and Innovations*, pp. SS1D–4, Optica Publishing Group, 2022.

[115] M. Nickerson, P. Verrinder, L. Wang, B. Song, and J. Klamkin, *Broadband optical phase modulator with low residual amplitude modulation*, in *Integrated Photonics Research, Silicon and Nanophotonics*, pp. IW4B–4, Optica Publishing Group, 2022.

[116] J. Talghader and J. Smith, *Thermal dependence of the refractive index of gaas and alas measured using semiconductor multilayer optical cavities*, *Applied Physics Letters* **66** (1995), no. 3 335–337.

[117] N. Kobayashi, K. Sato, M. Namiwaka, K. Yamamoto, S. Watanabe, T. Kita, H. Yamada, and H. Yamazaki, *Silicon photonic hybrid ring-filter external cavity wavelength tunable lasers*, *Journal of Lightwave Technology* **33** (2015), no. 6 1241–1246.

[118] C. Yang, L. Liang, L. Qin, H. Tang, Y. Lei, P. Jia, Y. Chen, Y. Wang, Y. Song, C. Qiu, *et. al.*, *Advances in silicon-based, integrated tunable semiconductor lasers*, *Nanophotonics* **12** (2023), no. 2 197–217.

[119] X. Zou, C. Li, X. Su, Y. Liu, D. Finkelstein-Shapiro, W. Zhang, and A. Yartsev, *Carrier recombination processes in gaas wafers passivated by wet nitridation*, *ACS applied materials & interfaces* **12** (2020), no. 25 28360–28367.

[120] J. J. Coleman, J. D. Young, and A. Garg, *Semiconductor quantum dot lasers: a tutorial*, *Journal of Lightwave Technology* **29** (2010), no. 4 499–510.

[121] M. Asada, Y. Miyamoto, and Y. Suematsu, *Gain and the threshold of three-dimensional quantum-box lasers*, *IEEE Journal of Quantum Electronics* **22** (1986), no. 9 1915–1921.

[122] Y. Arakawa and H. Sakaki, *Multidimensional quantum well laser and temperature dependence of its threshold current*, *Applied physics letters* **40** (1982), no. 11 939–941.

[123] D. Jung, J. Norman, M. Kennedy, C. Shang, B. Shin, Y. Wan, A. C. Gossard, and J. E. Bowers, *High efficiency low threshold current 1.3 μm inas quantum dot lasers on on-axis (001) gap/si*, *Applied Physics Letters* **111** (2017), no. 12.

[124] T. Kageyama, K. Nishi, M. Yamaguchi, R. Mochida, Y. Maeda, K. Takemasa, Y. Tanaka, T. Yamamoto, M. Sugawara, and Y. Arakawa, *Extremely high temperature (220 c) continuous-wave operation of 1300-nm-range quantum-dot lasers*, in *The European Conference on Lasers and Electro-Optics*, p. PDA_1, Optica Publishing Group, 2011.

[125] Y. Urino, N. Hatori, K. Mizutani, T. Usuki, J. Fujikata, K. Yamada, T. Horikawa, T. Nakamura, and Y. Arakawa, *First demonstration of athermal silicon optical interposers with quantum dot lasers operating up to 125 $^\circ$c*, *Journal of Lightwave Technology* **33** (2015), no. 6 1223–1229.

[126] M. Willatzen, T. Tanaka, Y. Arakawa, and J. Singh, *Polarization dependence of optoelectronic properties in quantum dots and quantum wires-consequences of valence-band mixing*, *IEEE journal of quantum electronics* **30** (1994), no. 3 640–653.

[127] T. Newell, D. Bossert, A. Stintz, B. Fuchs, K. Malloy, and L. Lester, *Gain and linewidth enhancement factor in inas quantum-dot laser diodes*, *IEEE Photonics Technology Letters* **11** (1999), no. 12 1527–1529.

[128] "Innolume." `https://www.innolume.com/`. Accessed on July 18, 2023.

[129] "QD Laser." `https://www.qdlaser.com/en/`. Accessed on July 18, 2023.

[130] L. Wang, B. Shi, H. Zhao, S. S. Brunelli, B. Song, D. C. Oakley, and J. Klamkin, *Toward all mocvd grown inas/gaas quantum dot laser on cmos-compatible (001) silicon*, in *CLEO: QELS_Fundamental Science*, pp. JTu2A–82, Optica Publishing Group, 2019.

[131] L. Wang, H. Zhao, B. Shi, S. Pinna, S. S. Brunelli, F. Sang, B. Song, and J. Klamkin, *High performance 1.3 μm aluminum-free quantum dot lasers grown by mocvd*, in *Optical Fiber Communication Conference*, pp. T4H–2, Optica Publishing Group, 2020.

[132] S. Ishutkin, V. Arykov, I. Yunusov, M. Stepanenko, V. Smirnov, P. Troyan, and Y. Zhidik, *The method of low-temperature icp etching of inp/ingaasp heterostructures in cl2-based plasma for integrated optics applications*, *Micromachines* **12** (2021), no. 12 1535.

[133] C.-W. Lee, D. Nie, T. Mei, and M. Chin, *Study and optimization of room temperature inductively coupled plasma etching of inp using cl2/ch4/h2 and ch4/h2*, *Journal of crystal growth* **288** (2006), no. 1 213–216.

[134] D. Jung, Z. Zhang, J. Norman, R. Herrick, M. Kennedy, P. Patel, K. Turnlund, C. Jan, Y. Wan, A. C. Gossard, *et. al.*, *Highly reliable low-threshold inas quantum dot lasers on on-axis (001) si with 87% injection efficiency*, *ACS photonics* **5** (2017), no. 3 1094–1100.

[135] A. Salhi, L. Fortunato, L. Martiradonna, M. Todaro, R. Cingolani, A. Passaseo, and M. De Vittorio, *High efficiency and high modal gain inas/ingaas/gaas quantum dot lasers emitting at 1300 nm*, *Semiconductor science and technology* **22** (2007), no. 4 396.

[136] S. T. Šuran Brunelli, B. Markman, A. Goswami, H.-Y. Tseng, S. Choi, C. Palmstrøm, M. Rodwell, and J. Klamkin, *Selective and confined epitaxial growth development for novel nano-scale electronic and photonic device structures*, *Journal of Applied Physics* **126** (2019), no. 1.

[137] A. Goswami, B. Markman, S. T. Š. Brunelli, S. Chatterjee, J. Klamkin, M. Rodwell, and C. J. Palmstrøm, *Confined lateral epitaxial overgrowth of ingaas: Mechanisms and electronic properties*, *Journal of Applied Physics* **130** (2021), no. 8.

[138] J. Li, Y. Xue, K. Xu, Z. Xing, K. S. Wong, and K. M. Lau, *Large-area inp laterally grown on soi for micro-lasers and fabry-perot lasers*, in *CLEO 2023*, p. STh3H.2, Optica Publishing Group, 2023.

[139] K. Feng, C. Shang, E. Hughes, R. Koscica, A. Clark, M. Debnath, G. Leake, D. Harame, P. Ludewig, and J. Bowers, *Electrically pumped quantum-dot lasers*

grown on cmos-compatible 300 mm si wafers, in *2022 28th International Semiconductor Laser Conference (ISLC)*, pp. 1–2, IEEE, 2022.

[140] B. Shi, S. Zhu, B. Song, and J. Klamkin, *Iii-v quantum dot lasers on silicon by selective area heteroepitaxy*, in *2022 28th International Semiconductor Laser Conference (ISLC)*, pp. 1–2, 2022.

[141] S. Zhu, B. Shi, B. Song, D. Hu, and J. Klamkin, *Iii-v lasers on silicon by selective area heteroepitaxy*, in *CLEO: Science and Innovations*, pp. SF2G–4, Optica Publishing Group, 2022.

[142] B. Shi, B. Song, A. A. Taylor, S. S. Brunelli, and J. Klamkin, *Selective area heteroepitaxy of low dislocation density antiphase boundary free gaas microridges on flat-bottom (001) si for integrated silicon photonics*, *Applied Physics Letters* **118** (2021), no. 12.

[143] J. Klamkin, S. Zhu, B. Shi, L. Wang, and B. Song, *Towards fully monolithic silicon-based integrated photonics: Mocvd grown lasers on silicon by blanket and selective area heteroepitaxy*, in *Novel In-Plane Semiconductor Lasers XXI*, vol. 12021, pp. 34–39, SPIE, 2022.

[144] B. Shi, A. Goswami, A. A. Taylor, S. T. Suran Brunelli, C. Palmstrøm, and J. Klamkin, *Antiphase boundary free inp microridges on (001) silicon by selective area heteroepitaxy*, *Crystal Growth & Design* **20** (2020), no. 12 7761–7770.

[145] D. K. Schroder, *Semiconductor material and device characterization.* John Wiley & Sons, 2015.

[146] P. Karbownik, A. Baranska, A. Szerling, W. Macherzynski, E. Papis, K. Kosiel, M. Bugajski, M. Tlaczala, and R. Jakiela, *Low resistance ohmic contacts to n-gaas for application in gaas/algaas quantum cascade lasers*, *Optica Applicata* **39** (2009), no. 4 655.

[147] A. Baca, F. Ren, J. Zolper, R. Briggs, and S. Pearton, *A survey of ohmic contacts to iii-v compound semiconductors*, *Thin solid films* **308** (1997) 599–606.

[148] S. Sze and J. Irvin, *Resistivity, mobility and impurity levels in gaas, ge, and si at 300 k*, *Solid-State Electronics* **11** (1968), no. 6 599–602.

[149] E. Schlecht, F. Maiwald, G. Chattopadhyay, S. Martin, and I. Mehdi, *Design considerations for heavily-doped cryogenic schottky diode varactor multipliers*, in *Proceedings of the Twenlfth International Symposium on Space Terahertz Technology*, 2001.

[150] M. Sotoodeh, A. Khalid, and A. Rezazadeh, *Empirical low-field mobility model for iii–v compounds applicable in device simulation codes*, *Journal of applied physics* **87** (2000), no. 6 2890–2900.

[151] "Nanophotonics and System Integration."
https://www.nasp.de/gap-on-si.html. Accessed on July 18, 2023.

[152] "AIM Photonics MPW Services." https://www.aimphotonics.com/mpw. Accessed on July 18, 2023.

[153] J. Flemish and K. Jones, *Selective wet etching of gainp, gaas, and inp in solutions of hcl, ch 3 cooh, and h 2 o 2*, *Journal of The Electrochemical Society* **140** (1993), no. 3 844.